SECONDARY ION MASS SPECTROMETRY BY TIME-OF-FLIGHT

A Thesis

Submitted to

the Faculty of Graduate Studies

University of Manitoba

In Partial Fulfillment

of the Requirements for the Degree

Doctor of Philosophy

by

Erich Werner Ens

March 1984

SECONDARY ION MASS SPECTROMETRY BY TIME-OF-FLIGHT

by

Erich Werner Ens

A thesis submitted to the Faculty of Graduate Studies of the University of Manitoba in partial fulfillment of the requirements of the degree of

DOCTOR OF PHILOSOPHY

ACKNOWLEDGEMENTS

I would like to thank my advisor, Dr. K. Standing for directing this research and for his assistance with the details of the experiments. I am grateful to Dr. B. Chait (now at Rockefeller University) who is largely responsible for the design and construction of the mass spectrometer and continues to provide valuable advice. (He also took the data at Rockefeller for the comparison experiment.) I was fortunate to join this project shortly after the instrument was completed so the present experiments could begin immediately. Drs. R. Macfarlane and D. Torgerson have had an interest in this project since the beginning and continue to provide useful suggestions. Helpful advice from Dr. J. Westmore including assistance in the interpretation of the mass spectra is gratefully acknowledged. I am indebted to Ron Beavis for several contributions; in particular he performed the final measurements on the metastable decay of CsI clusters. Contributions from Dr. B. Schueler and Grant McIntosh are also appreciated.

I am grateful to Heidi Harms for typing with an unfamiliar word processor from a nearly illegible first draft, and to my wife Chris Loepp who spent many late nights preparing figures and making revisions even while she was 7 months pregnant. Chris's patience throughout this ordeal is greatly appreciated.

Financial assistance in the form of research grants and fellowships was provided by the Natural Sciences and Engineering Research Council.

ABSTRACT

The operation and performance of the Manitoba time-of-flight mass spectrometer is described. The recent implementation of a commercial time-to-digital converter is described and compared to the conventional timing method (time-to-amplitude conversion) used earlier.

Mass spectra obtained here with keV alkali ions and in Rockefeller University with ~100 MeV fission fragments from ^{252}Cf were found to be similar. Yields of secondary ions from alanine were measured for primary alkali ions (Cs^+, K^+, Na^+, and Li^+) at energies 1 keV to 16 keV. Yields increase greatly with increasing energy and with the mass of the bombarding particle, suggesting that in this energy region the nuclear stopping is mainly responsible for the secondary ion production. This is in contrast to the case for fission fragments where electronic stopping must be responsible. Thus, it appears that the mass spectra are fairly insensitive to the form of the incident energy loss.

Secondary ions $[(CsI)_nCs]^+$, with n up to ~40, were produced by 8 keV Cs^+ bombardment of CsI. The yield of clusters decreased smoothly with n when observed in a time-of-flight mass spectrometer at effective times ~ 0.2 μs after emission. Clusters with $n > 7$ were found to be metastable, with lifetimes $\ll 100$ μs. A large anomaly in the population of the disintegration products was measured at ~ 70 μs after emission, $n = 13$ clusters being favored and $n = 14$ and 15 being suppressed.

A marked increase in the yield of cations, anions and all cluster ions was observed after irradiating alkali halides with $\gtrsim 10^{14}$ alkali ions/cm^2. In addition, the irradiation was found to produce emission of cluster ions delayed by ~200 ns after the primary ion impact.

CONTENTS

LIST OF FIGURES

CHAPTER 1

INTRODUCTION

Mass spectrometry provides a useful tool for chemical analysis by supplying information on molecular weight and chemical structure for a large variety of compounds. Such analysis involves volatilization and ionization of atomic or molecular species followed by electrostatic or magnetic mass-to-charge separation. The structural information is obtained from the masses of fragments produced by the processes of volatilization and ionization. This fragmentation, however, has also presented the major limitation on mass spectrometry as an analytic tool; as the molecular mass increases, the molecule tends to become less volatile and more fragile, resulting in complex mass spectra, often without molecular weight information.

The problem arises already for many fairly small molecules. For example, fig. 1.1 shows the mass spectrum of the amino acid alanine (m/z 89), as obtained by conventional methods (1) where the sample is volatilized by heating and ionized by electron impact (EI). The molecular ion at m/z 89 is more than two orders

of magnitude less intense than some of the fragments, and in fact accounts for only about 0.1% of the total yield. For molecules such as this, it is usually possible to improve the situation by "derivatization" - the preparation of more volatile compounds from the material of interest - but this has serious limitations for large molecules.

Fragmentation during ionization may be reduced by using chemical ionization (CI) (2) in which a reagent gas at ~1 torr is ionized by electron impact and the sample, at much lower pressure ($\sim 10^{-3}$ torr), is ionized by reacting with the reagent ions. This

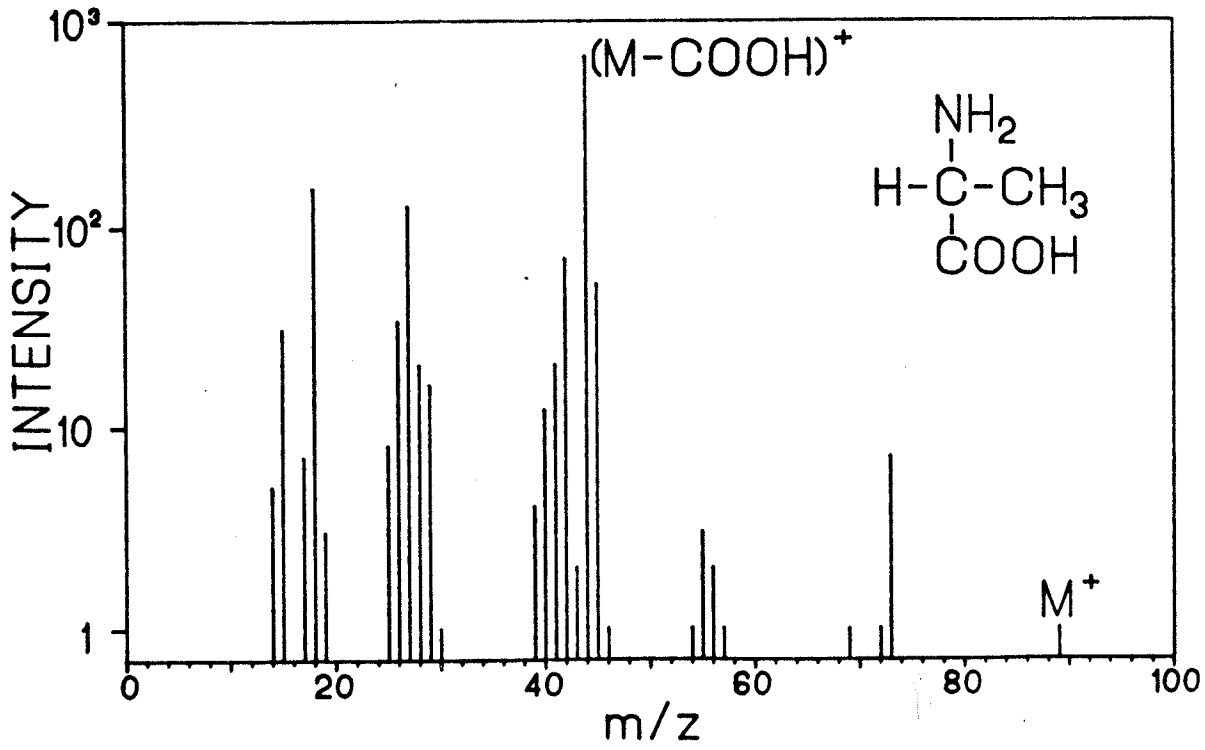

Figure 1.1 Electron impact spectrum of alanine (m/z 89). The molecular ion is >100 times less intense than the most intense fragment. Data taken from ref. 1.

method, however, still requires gaseous samples and therefore offers limited improvement for thermally labile molecules of low volatility.

Several so called "soft-ionization" techniques have been developed (3,4) to extend the application of mass spectrometry to larger, more fragile molecules. Many of these require only minor modifications to conventional EI or CI sources; fragmentation during volatilization is reduced by depositing the sample onto an inert surface (e.g. Teflon) (5) or by rapid heating so that vaporization is favoured kinetically over decomposition (6). "In beam" methods (7), where the sample probe is placed close to the ionizing electron beam, also show reduced fragmentation.

The most successful soft ionization methods desorb and ionize the sample molecule directly from the condensed phase. The earliest such method, field desorption (FD), was introduced by Beckey in 1969 (8). In this method, ions are desorbed from extremely fine emitters by a strong electrostatic field. Simons et al (9) have used the same principle to desorb ions from the liquid phase. Field desorption has produced the simplest spectra for many compounds. However, difficulty in sample preparation and poor reproducibility have limited application of this technique.

Molecules may also be desorbed and ionized directly by the impact of energetic primary ions or atoms, or laser pulses. Macfarlane and Torgerson (10) first demonstrated this technique with fission fragments from ^{252}Cf, using a time-of-flight mass spectrometer (11) initially used to obtain mass spectra of short-lived radioisotopes. The ionizing radiation was observed to cause desorption and ionization of molecules adsorbed to a surface. To

investigate the potential of such radiation for chemical analysis, they placed a ^{252}Cf source behind a thin metal foil coated with an organic sample. A time-of-flight mass spectrometer places no fundamental limit on the mass range and the early demonstrations (10) included involatile samples of molecular weight near 2000. Organic molecular ions with mass near 14000 have since been observed with this technique (12). Accelerated ions in the same energy range have been used to study the desorption mechanism (13,14). Progress in high energy, heavy ion induced desorption has been reviewed by Macfarlane (15).

Using a magnetic instrument, Benninghoven and Sichtermann (16) demonstrated similar results for small molecules ($m/z \lesssim 300$) with low energy primary ions (~2 keV Ar^+). Secondary ion mass spectrometry (SIMS) is well established in surface analysis but the primary ion flux normally used ($> 10^{-6}$ A/cm^2) destroys or sputters away adsorbed molecules in a very short time; with 10^{-6} A/cm^2 the molecular parent ion yield from an amino acid disappears in a few seconds (16). Benninghoven kept the primary ion flux sufficiently low ($\lesssim 10^{-9}$ A/cm^2) so that the probability of striking the same spot twice during an experiment was negligible. This technique - called molecular or static SIMS - allows organic samples to be analysed with limited damage. The mass range was limited in the early demonstrations by the type of mass spectrometer used.

In a recent variation of molecular SIMS, introduced by Barber et al (17), the sample is dissolved or dispersed in a viscous liquid (usually glycerol) and bombarded with neutral atoms in the same energy range. "Fast atom bombardment (FAB)"

allows relatively simple adaptation to existing spectrometers since ion optics needn't be considered. In addition, higher primary beam fluxes may be used since the surface is continually renewed as the liquid matrix evaporates. FAB has been used with high performance sector-field instruments and a wide range of organic molecules up to m/z ~ 5700 have been observed (18,19).

The use of laser pulses to desorb nonvolatile organic molecules was first demonstrated in 1978 by Posthumus et al (20), with a magnetic sector instrument. Nonvolatile compounds have also been analysed using time-of-flight (21). Laser desorption spectra are generally less reproducible than those obtained by particle induced desorption and reported observations of high mass ions (m/z > 1000) are scarce.

* * *

The Manitoba time-of-flight mass spectrometer (22), completed in 1979, was originally designed to use fission fragments to induce desorption. After the discovery of similar results (at low mass) with keV primary ions (16), a pulsed ion gun was designed to take advantage of their convenience and versatility and retain the sensitivity and unlimited mass range of time-of-flight. The instrument is similar to that of Macfarlane and Torgerson (11) but uses a pulsed beam of keV ions rather than fission fragments. Its construction, operation and performance are described in detail in chapters 2, 3 and 4. Similar instruments have been constructed recently at

Uppsala (23) and Rockefeller (24). A curved time-of-flight instrument using low energy primary ions has recently been reported by Benninghoven (25).

The Manitoba instrument was the first to obtain a molecular ion peak from vitamin B_{12} using low energy ions (26) although it had been observed using fission fragments several years earlier (10). It has been used to study two classes of biological compounds (neuropeptides and fully-protected oligonucleotides) up to m/z 3452 (27-30).

Since bond energies are typically 2 - 5 eV, it is surprising that large molecules can be desorbed intact by incident primary ions which deposit up to 400 eV/Å. An understanding of the mechanism involved in molecular ion desorption should lead to its more effective exploitation. Measurements of the effects of primary ion characteristics on the mass spectrum, shed light on the physical processes involved and provide practical information for the application of the technique. Two experiments were performed to study primary ion effects: (i) In collaboration with B.T. Chait and F.H. Field at Rockefeller University, the mass spectra for a series of compounds obtained with low energy ions and ^{252}Cf fission fragments were compared. (ii) The yield of the amino acid alanine was measured as a function of energy for the primary ions Li^+, Na^+, K^+, and Cs^+ between 1 and 16 keV. These experiments are reported in chapter 5.

It has long been recognized that linear time-of-flight mass spectrometers have certain advantages for the observation of metastable ions (31). When an ion decomposes within the flight tube of such an instrument, the centre-of-mass of the resulting

fragments continues on to the detector with unchanged velocity. Thus the fragments appear in the mass spectrum at the approximate position of the parent ions, but the peak is broadened by the energy release. The pattern of metastable decay may be studied by using retarding grids at the end of the flight tube (31-34). Measurements of metastable decay patterns of CsI clusters are presented in chapter 6.

CHAPTER 2

THE MANITOBA TIME-OF-FLIGHT MASS SPECTROMETER

2.1 INTRODUCTION

A description of the Manitoba time-of-flight mass spectrometer has been reported previously (22). The principle of the device is illustrated in fig. 2.1. A thin layer of organic material deposited onto the target backing is struck by a

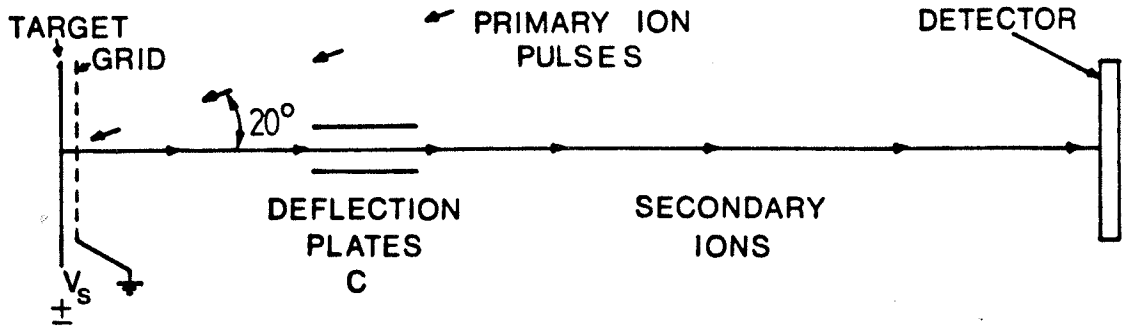

Figure 2.1 Schematic diagram of the time-of-flight mass spectrometer (not to scale).

succession of ion pulses from the source. When these pulses of primary ions hit the target, they may liberate secondary ions. Each secondary ion is accelerated to a fixed energy by the electric field between the target and a parallel grid. Measurement of the flight time determines the velocity and from this the mass to charge ratio may be calculated.

A photograph of the instrument is shown in fig. 2.2. The system is almost entirely metal-sealed. Sublimation pumps and ion pumps are used to provide operating pressures in the 10^{-8} torr range. Rough pumping is done by sorption pumps and a venturi pump so that clean vacuum conditions are maintained throughout evacuation. The apparatus is constructed of non-magnetic stainless steel. The flight tube has a length of $\approx$ 1.6 m and an internal diameter of $\approx$15 cm. A vacuum lock is provided on a side tube, so that targets may be changed without disturbing the vacuum in the main system.

2.2 SAMPLE PREPARATION AND INSERTION

The sample foil - usually 6.4 μm aluminized polyester (Alexander Vacuum Research, Inc. Type C1) - is stretched over a 1.8 cm diameter stainless steel ring with a tightly fitting outer ring (fig. 2.3).

NOTICE/AVIS

PAGE(S) 10 IS/ARE/EST/SONT black+white photo

PLEASE WRITE TO THE AUTHOR FOR INFORMATION, OR CONSULT THE ARCHIVAL COPY HELD IN THE DEPARTMENT OF ARCHIVES AND SPECIAL COLLECTIONS, ELIZABETH DAFOE LIBRARY, UNIVERSITY OF MANITOBA, WINNIPEG, MANITOBA, CANADA, R3T 2N2.

VEUILLEZ ECRIRE A L'AUTEUR POUR LES RENSEIGNEMENTS OU VEUILLEZ CONSULTER L'EXEMPLAIRE DONT POSSEDE LE DEPARTEMENT DES ARCHIVES ET DES COLLECTIONS SPECIALES, BIBLIOTHEQUE ELIZABETH DAFOE, UNIVERSITE DU MANITOBA, WINNIPEG, MANITOBA, CANADA, R3T 2N2.

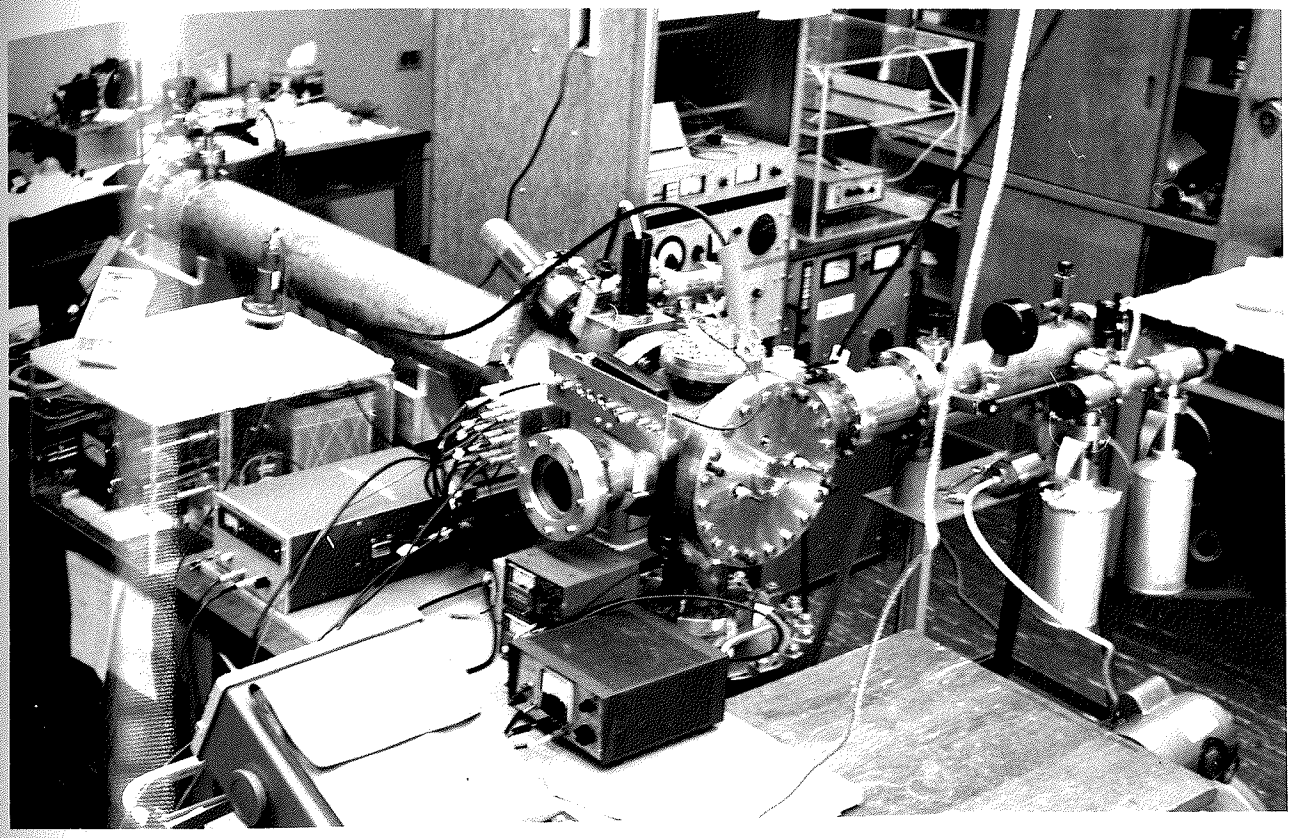

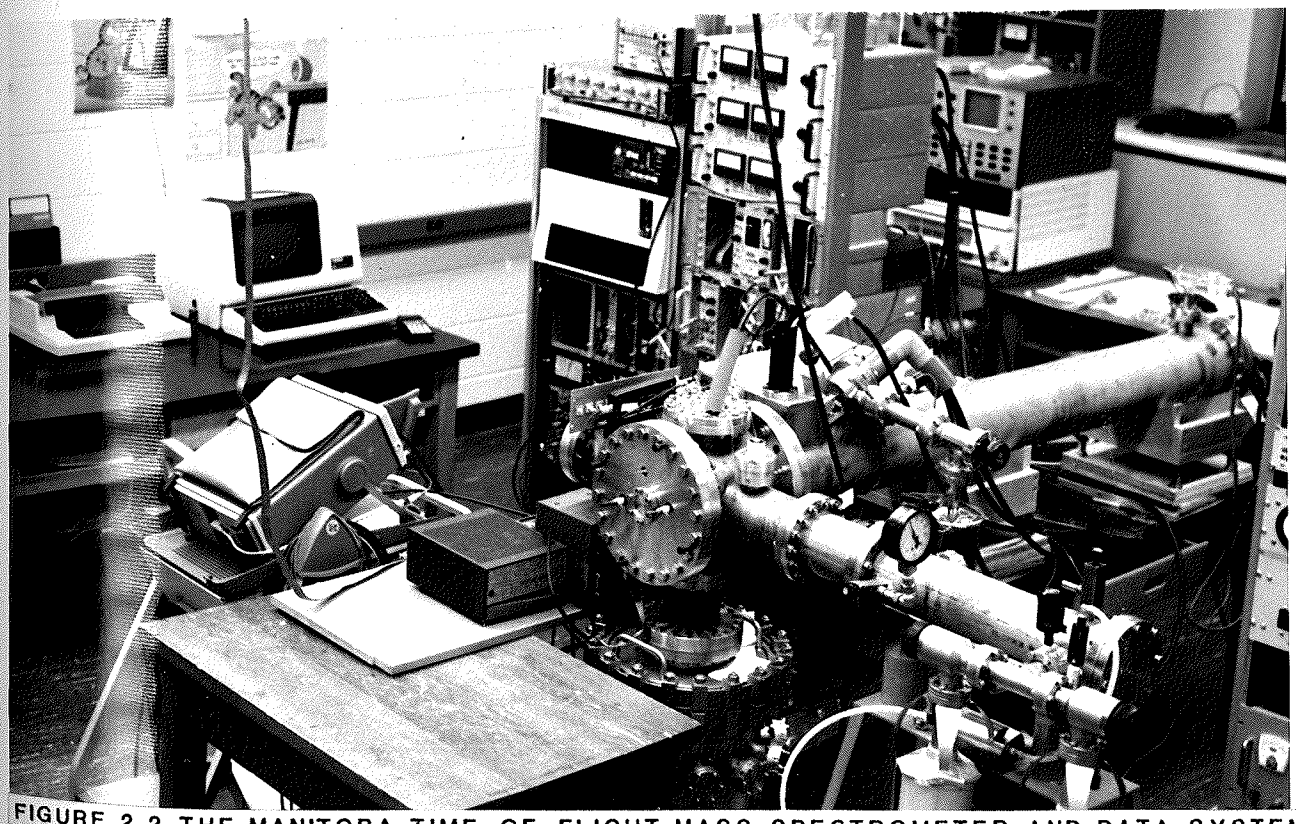

FIGURE 2.2 THE MANITOBA TIME-OF-FLIGHT MASS SPECTROMETER AND DATA SYSTEM.

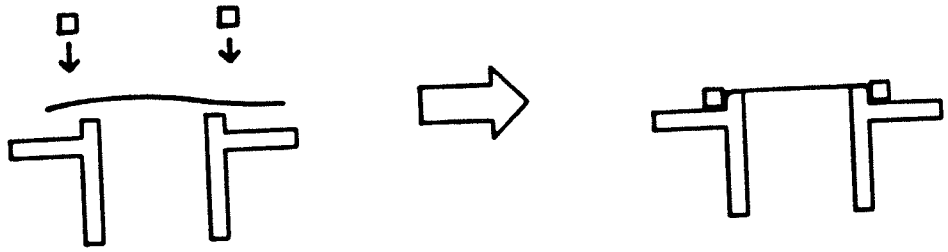

Figure 2.3 Mounting of the sample foil; usually aluminized polyester.

Other materials have been used (Ag,C,Ni,Al) but accurately planar surfaces are most easily obtained with the inexpensive polyester because of its elasticity. Significant effect on the mass spectrum of the sample backing has not been observed here, although systematic measurements have not been made. The few compounds that have been analysed on a carbon backing (Union Carbide GRAFOIL) show less intense background peaks for $m/z \lesssim 200$ but otherwise the spectra are similar to those obtained using aluminized polyester backing. Only one compound (stearic acid) has been analyzed using Ag backing. Apart from the observation of Ag^+ peaks, the spectrum obtained from an electrosprayed (see below) target was similar to that obtained using Al-polyester. No comparison of yields using different target backings has been made here. (Benninghoven has observed significant effects of target backing when thin layers of sample were evaporated onto the target surface (35). The effects are obscured when thicker coverage is used.)

The sample is deposited from solution onto the foil by the electrospray method (36,37) based upon the atomization of a liquid by a strong electrostatic field (38). The present implementation, illustrated in fig. 2.4, is closest to that of McNeal et al (36). A solution containing the sample is placed into the reservoir of a 26 gauge hypodermic needle (Bector Dickinson Canada, YALES 5110). A 0.2 mm diameter stainless steel wire is inserted into the needle to regulate flow. With the needle positioned a few cm above the target a potential of 2 to 10 kV causes tiny charged droplets to spray onto the target foil. The needle to target distance and potential are varied to obtain the desired spray quality and spot size; the drops should be small enough so that most of the solvent evaporates and the solute residue hits the target without visibly wetting it.

Uniformly fine spray is most easily obtained if the solvent has low surface tension. Methanol or acetone with up to 20% water (if necessary) are the most common solvents. A typical concentration of ~1 μg/μl results in droplet residues ~1 μm in size (fig. 2.5). Higher concentrations produce larger average residues.

A modified travelling microscope is used to enable vertical and horizontal movement of the needle. The spray is most easily observed with a weak laser but is also visible with a penlight in a darkened room. The apparatus is housed inside a Plexiglass box to prevent air currents from disturbing the spray.

Five targets are mounted in a ceramic sample holder. This is introduced into the system through the vacuum lock and moved by a rack and pinion system.

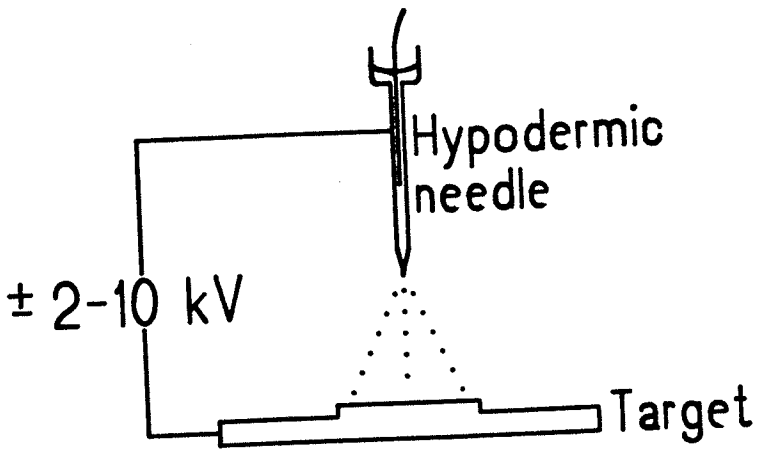

Figure 2.4 Target preparation by electrospray. The electric field causes tiny droplets (~μm) to spray onto the target foil. Most of the solvent evaporates before the solute hits the target.

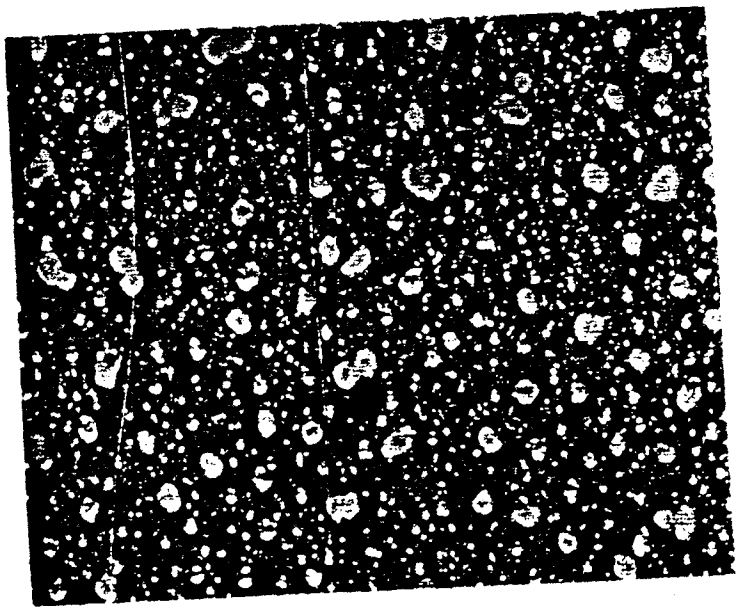

Figure 2.5 600 μl of ~ 1 μg/μl alanine electrosprayed onto ~1 cm^2 aluminized polyester. Magnification × 640.

2.3 SECONDARY ION ACCELERATION

The sample is positioned behind the acceleration grid (90% or 60% transmission Ni mesh - Buckbee Mears Co.) where contact is made to the high voltage feed-through. Three ceramic balls glued to the grid assembly define the plane of the target 2 mm from the grid. Positive or negative secondary ions may be analysed by placing high voltage of the corresponding polarity on the target. Source voltages V_s up to 10 kV have been used.

Ions desorbed with zero initial kinetic energy are accelerated to an energy $q_s V_s = 1/2\, m_s v_s^2$. The square of the flight time is therefore proportional to the ratio of mass to charge:

$$t_o = \sqrt{\frac{m_s}{2q_s V_s}}\ (\ell + 2d)$$

Here ℓ is the length of the drift region and d is the acceleration distance. For an initial axial velocity v_{oz} where $\epsilon_z = 1/2\, m_s v_{oz}^2 \ll q_s V_s$ the flight time to a good approximation (using also $d \ll \ell$) is

$$t = \sqrt{\frac{m_s}{2q_s V_s}}\ (\ell + 2d - \ell\frac{\epsilon_z}{2q_s V_s})$$

For $\epsilon_z = 2$ eV the flight time of a 10 keV ion with m/z 1000 (36 μs) changes by 3.6 ns. However, if ϵ_z is independent of mass, time is still proportional to $\sqrt{m_s}$. The constant of proportionality is determined from the flight times of ions with known mass.

A spread in $\mathcal{E}_z$ causes a time spread given by

$$\Delta t_s = \Delta \mathcal{E}_z \frac{\sqrt{m_s}}{(2q_s V_s)^{3/2}}$$

In contrast to the situation in some earlier time-of-flight spectrometers (39), the secondary ion accelerating field is constant in time. Also, the ions are formed very close to an equipotential surface (the target backing) which is perpendicular to the spectrometer axis. As a result of these two factors the axial velocity distribution is relatively narrow*. This is illustrated by the

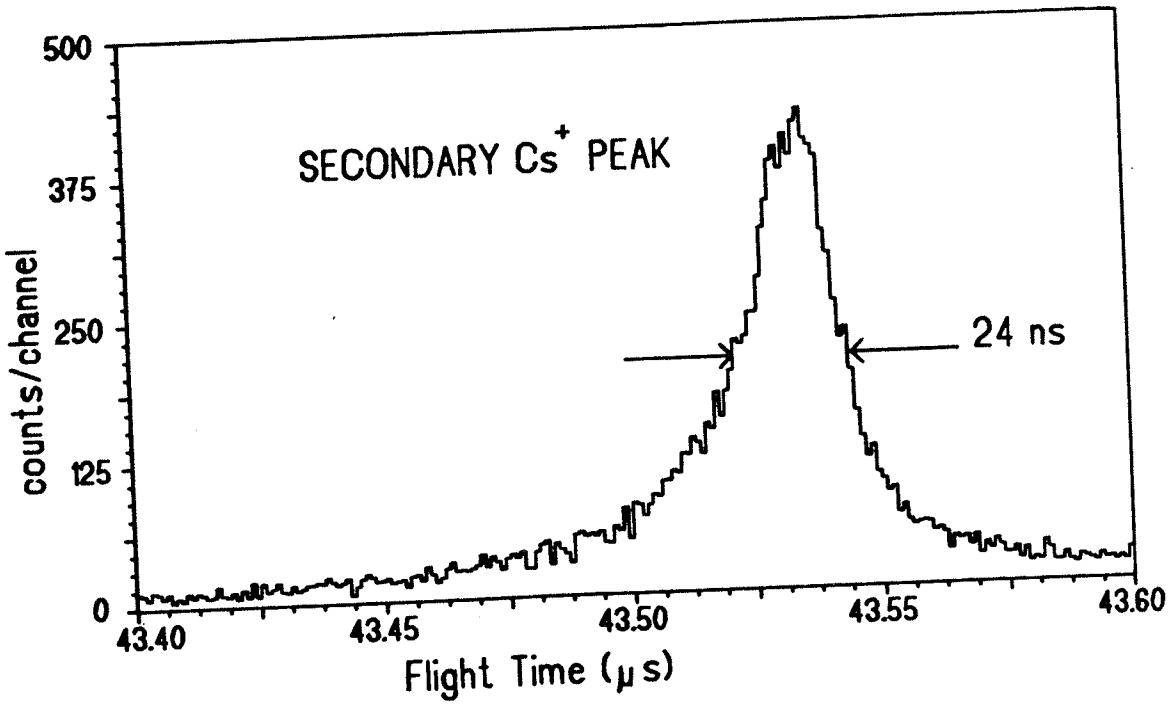

Figure 2.6 Time spectrum of 1 keV secondary Cs^+ ions ejected from a CsI target by 17 keV Cs^+ primary beam. The full width at half maximum of 24 ns corresponds to an initial axial velocity spread $\Delta v_{oz} = 1.3 \times 10^5$ cm/s or a spread in $\mathcal{E}_z = (mv_{oz}^2)/2$ of $\Delta \mathcal{E}_z = 1.15$ eV. The previously reported value of 2.2 eV (89) is in error due to a miscalculation.

* Compare, for example, the velocity distributions obtained recently in spectrometers with diffuse sources (40,41).

time spectrum of secondary Cs^+ ions from a CsI target shown in fig. 2.6. The accelerating voltage in this measurement is kept low to separate this effect from the time spread caused by the primary pulse duration. The initial energy spread is not the dominant factor in peak broadening for most compounds in the present arrangement. Peak broadening is discussed in greater detail in §4.4.

2.4 PRIMARY ION SOURCE

2.4.1 Ion Production and Focusing

The pulsed-ion gun is illustrated schematically in fig. 2.7. Alkali metal ions (Li^+,Na^+,K^+, or Cs^+) are emitted thermionically from a small glassy bead of alkali aluminosilicate (42,43) melted onto the end of a tungsten hairpin filament. This type of source was chosen because of its simplicity, low cost, and minimal pumping requirements. Source preparation is described in appendix A.

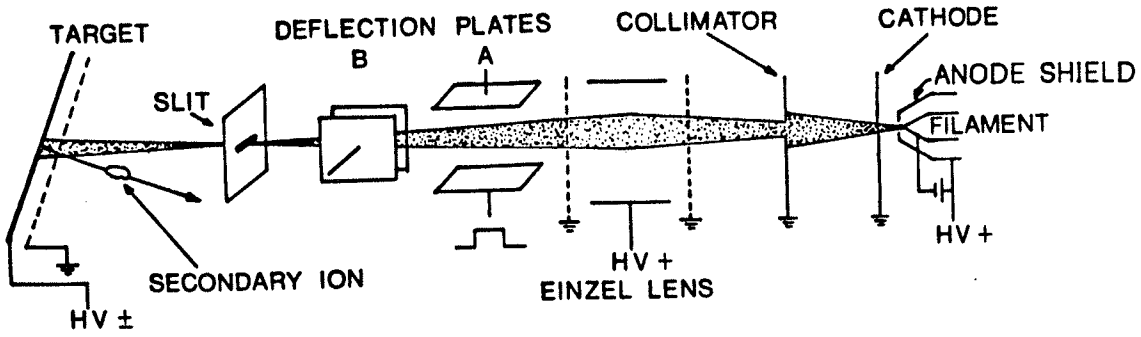

Figure 2.7 Pulsed positive-ion source.

The electrostatic design of the source is based on the three-electrode guns widely used in electron microscopy (44,45). The plane cathode is operated at ground potential. The position of its aperture (1.5 mm diameter) may be adjusted externally in the plane perpendicular to the ion beam axis, in order to provide accurate alignment of the extracted beam. The filament is held at a potential V_p, so the energy of a primary ion (mass m_p, charge q_p) leaving the source is q_pV_p. Source potentials V_p up to 25 kV have been used. The anode shield is set at a potential near V_p (usually a few hundred volts above) adjusted to give an optimum beam. This depends on the particular source geometry and usually changes during the source lifetime.

The beam is focused by a gridded Einzel lens (46) to a spot of ~50 μm diameter in the plane containing the defining slit, 32 cm from the source. The lens has a diameter of 4 cm and is approximately midway between the source and the slit. Optimum potential of the lens is near 1/2 V_p. The 60% transmission Ni grids (197 lines/cm - Buckbee Mears Co.) are spaced 3.2 cm apart. The size of the apertures in the grid (~30 μm) is the lower limit of the spot size (47,48).

2.4.2 Pulsing the Ion Beam

The focused beam is swept rapidly across the 35 μm wide slit by a voltage pulse V_{def} applied to the deflection plates A (fig. 2.7) resulting in a short burst of ions passing through the slit. To prevent a second ion burst from appearing on the falling edge of the voltage pulse, a delayed pulse is applied to the other set of deflection plates B, oriented at right angles to the

first set. The resulting path of the ion beam spot at the slit is illustrated in fig. 2.8. The plates are 3 cm long and 1 cm apart and are positioned 13 cm and 9.5 cm from the slit.

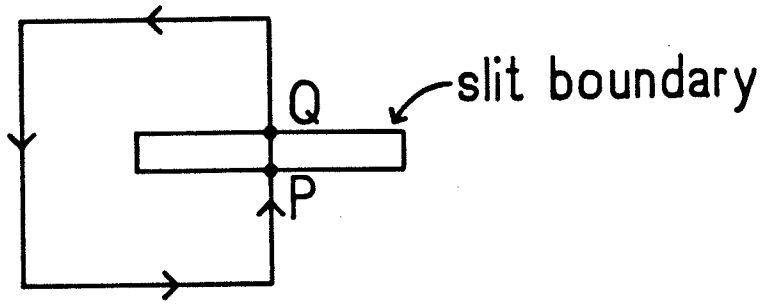

Figure 2.8 The path of the beam focus at the slit.

A small voltage V_{dc} across the plates is required to direct a dc ion beam through the slit. Under pulsed conditions, an offset voltage V_o is applied to one plate and the voltage pulse is applied to the opposite plate. Fig. 2.9 illustrates the electric field experienced by an ion that hits the lower

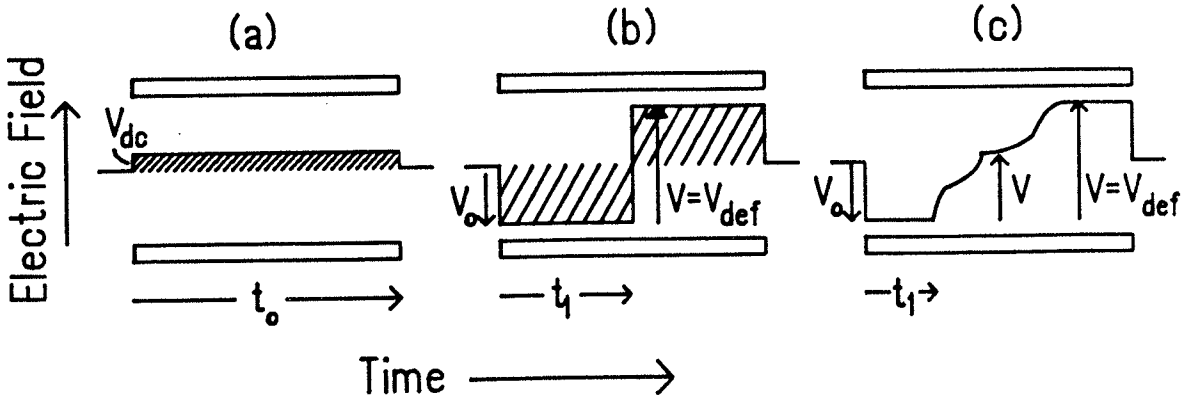

Figure 2.9 The electric field observed by an ion that hits point P in fig. 2.8 under dc conditions (a) and under pulsed conditions with zero risetime (b) and arbitrary risetime (c). The net impulse must be the same for the two conditions so $V_{dc}t_o = \int(V - V_o)dt$.

slit boundary (point P in fig. 2.8) under dc and pulsed conditions. Since the net impulse must be the same in the two cases, the time integral of the electric field must be equal. Thus,

$$\frac{V_{dc}t_o}{d} = -\int_0^{t_1} \frac{V_o}{d}\,dt + \int_{t_1}^{t_o} \frac{(V - V_o)}{d}\,dt$$

where t_o is the transit time between the plates, t_1 is the time an ion has spent between the plates before the pulse fires, and d is the plate separation. Then

$$V_{dc}t_o = \int_0^{t_o} V dt - V_o t_o$$

The net impulse is the same for a pulse with zero risetime (fig. 2.9b) or an arbitrary risetime $< t_o$ (fig. 2.9c) if $\int V dt$ is the same.

An ion which hits the upper slit boundary (point Q in fig. 2.8) arrives at the deflecting plate Δt_1 later than the one considered above and will receive an additional impulse $-V_{def}\Delta t_1$. A corresponding increase ΔV_{dc} in the dc voltage is required to give the same additional impulse: $\Delta V_{dc}t_o = -V_{def}\Delta t_1$. This is the area shown in fig. 2.10 and is independant of the risetime provided it is less than the transit time between the plates.

For a beam focused to a point, the duration of the primary pulse Δt_p is the magnitude of the time difference Δt_1:

$$\Delta t_p = \frac{\Delta V_{dc}t_o}{V_{def}} \qquad (2.1)$$

This relation offers a simple prediction of the primary pulse duration from an easily measured quantity ΔV_{dc} and indicates the importance of the deflection pulse height in obtaining short

pulses. The measurement of ΔV_{dc} (the range of dc deflection voltages for which ions are transmitted) takes the size of the beam spot into account; the effective slit width is approximately the sum of the geometrical slit width and the size of the beam spot. For 18 keV Cs^+ ions, the measured value of $\Delta V_{dc} \approx 7$ V giving an expected pulse duration of $\Delta t_p = 1.8$ ns for $V_{def} = 1$ kV. In this calculation the fringing fields are taken into account (49); the transit time t_o is taken as the time to travel the effective length of the plates, $\ell + \Delta\ell$ where

$$\Delta\ell = \frac{d}{\pi}\left(1 - \ln\frac{d}{2\pi\ell}\right) \qquad (2.2)$$

To relate the pulse duration to the primary ion energy and the ion gun geometry, $\Delta V_{dc} t_o$ in eq'n 2.1 may be replaced. For a point beam, ΔV_{dc} is the voltage required to deflect the beam across the width s of the slit. The corresponding impulse Δp is given by $\Delta p/p = s/L$ where L is the distance from the centre of the

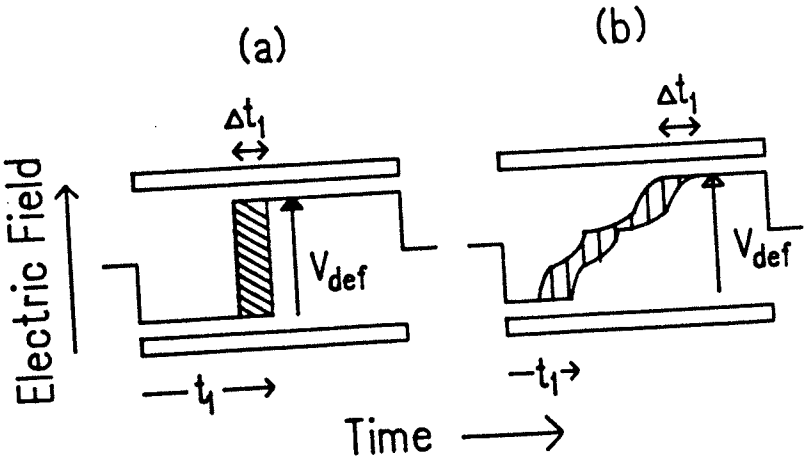

Figure 2.10 The primary pulse duration is the range of values t_1 may take. The shaded area represents the corresponding range of impulses for a deflection pulse with (a) zero risetime and (b) arbitrary risetime. The area is $\Delta t_1 V_{def}$ in both cases so Δt_1 is independent of the risetime provided it is less than the transit time t_o.

plates to the plane of the slit. Since $\Delta p = q_p \Delta V_{dc} t_o / d$, $\Delta V_{dc} t_o = psd/Lq_p$. Substitution into eq'n (2.1) gives

$$\Delta t_p = \frac{(sd)}{(L\sqrt{q_p})} \frac{\sqrt{2m_p V_p}}{V_{def}} \qquad (2.3)$$

using $p = (2m_p q_p V_p)^{1/2}$. For the above conditions (18 keV Cs^+ ions, $V_{def} = 1$ kV) using the geometrical slit width ($s \sim 35$ μm) this gives an ion burst of 0.6 ns duration; an effective slit width of ≈ 100 μm is consistent with the above result (1.8 ns). The measured secondary electron peak width under these conditions is 2.1 ns (fig. 2.11).

The finite angle of incidence of the beam and the size of the beam spot might also be expected to influence the effective

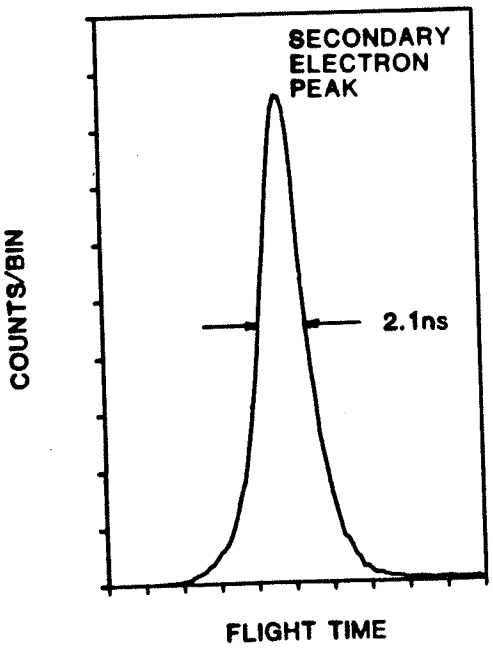

Figure 2.11 Time spectrum of 5 keV secondary electrons ejected from a target of CsI by 23 keV Cs^+ ions. (With $V_p = 18$ kV and $V_s = -5$ kV the energy of the primary ions at the target is 23 keV - see §2.4.3.) The width of this distribution is a good measure of the width of the primary beam pulse, since at -5 kV accelerating voltage the electron flight time is ~40 ns so the spread is expected to be negligible ($\lesssim$ 10 ps).

pulse duration; the flight times (from the slit to the target) of two 18 keV Cs^+ ions incident at 20°, on the top and bottom of the beam spot (0.5 to 1 mm apart), differ by 1 to 2 ns. If this is independent of the broadening treated above the effects add in quadrature. For the above conditions this gives an additional time spread between 0.2 and 0.9 ns. Fig. 2.11 indicates that the effect is small.

Originally the beam was pulsed using 50 V pulses from an E-H Research Laboratories Model 131 pulse generator giving ion bursts between ~6 and ~50 ns in duration depending on primary ion energy and species. The data presented in §4.2 were taken in this way. Shorter ion bursts (2 to 3 ns) are obtained using a switching power transistor in the circuit shown in fig. 2.12. With this arrangement, the plates are pulsed from high voltage of ~1 kV to ground with a risetime of 50 to 100 ns. This is longer than the

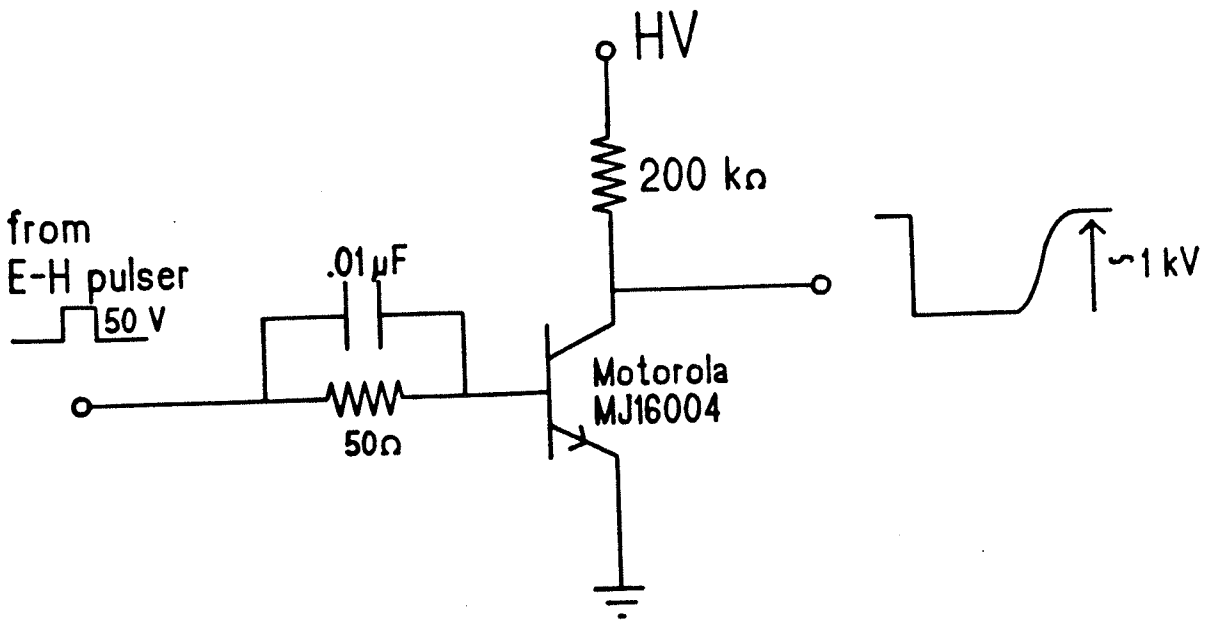

Figure 2.12 Pulsing circuit used to sweep the primary beam past the slit.

risetime of the pulses from the commercial pulser but still shorter than the transit time between the deflection plates of 25 keV Cs^+ (~220 ns) or K^+ (~120 ns) ions.

A similar method is used to pulse the deflection plates B to optimum dc condition just before the leading edge of the deflection pulse on plates A, and back to high voltage before the falling edge. This is illustrated in fig. 2.13.

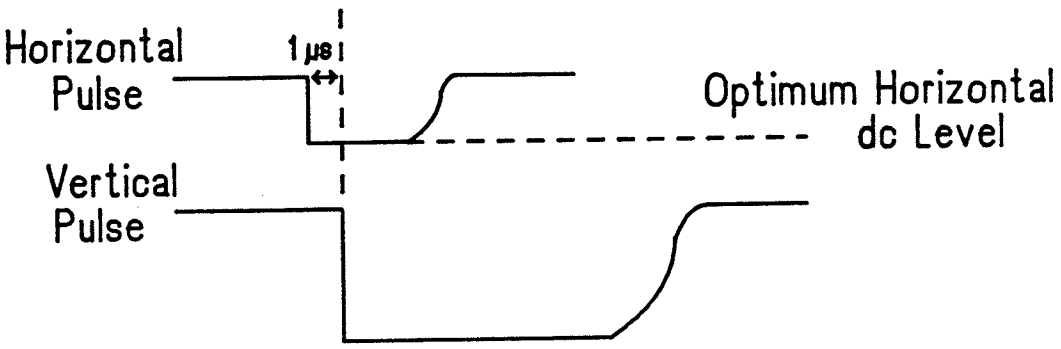

Figure 2.13 Timing of deflection plate pulses. Deflection plates B are pulsed to the optimum dc level just before the beam is swept past the slit with deflection plates A, and back to high voltage before the beam sweeps back.

2.4.3 Primary Ion Flux and Current Density

To compare secondary ion yields from different targets, or from the same target for different primary ion characteristics, it is necessary to determine the primary ion flux incident on the target. This is determined by measuring the dc beam hitting the slit in fig. 2.7 and calculating the fraction of the beam which passes through the slit.

The slit current (I_{slit}) determines the number of ions passing through the slit per pulse: $n = I_{slit}\Delta t_p/e$ where e is the electronic charge and Δt_p is the pulse duration given by eq'n 2.3 taking s as the geometrical slit width. This is independent of spot size since n is obtained by integrating the contribution from each point in the beam spot. Then the total number of incident ions in a measurement (assuming constant I_{slit}) is

$$N_p = nfTG = \frac{I_{slit}\Delta t_p}{e} fTG$$

where fT (frequency × measurement time) is the total number of pulses, and G is the transmission of the acceleration grid. Using eq'n 2.3 for Δt_p, the total incident flux is

$$N_p = \frac{(I_{slit}T)fG}{e} \left(\frac{sd\sqrt{2m_pV_p}}{L\sqrt{qV_{def}}}\right) \qquad (2.4)$$

The integrated slit current ($I_{slit}T$) is measured by counting the output pulses from a current-to-frequency converter (Analogue Technology Corp. Model 170). For many measurements, where only relative yields are required, this value is sufficient for normalization provided the other quantities in eq'n 2.4 are constant. If the primary ion energy or the mass is changed $I_{slit}T\sqrt{m_pV_p}$ provides normalization. When absolute yields are being measured as in §5.3, eq'n 2.4 should be used with caution; the slit forms the end of a perforated cylinder which is isolated from the rest of the ion gun and some secondary electrons may escape through the perforations, thus increasing the apparent primary current. The estimates of absolute yields should therefore be treated as lower limits.

For a given pulse duration, the ion flux at the target may be set to a suitable value by varying the dc ion-beam current; this is done by adjustment of the filament current. Under various operating conditions, the dc current at the plane of the slit has ranged from 0.3 to 200 nA. Normally the beam is adjusted so that ~100 to ~2000 ions per pulse pass through the slit and hit the target at a repetition frequency of 2 to 5 kHz, corresponding to an average ion current of ~0.1 to ~1 pA. Since the target beam spot has a diameter of ~1 mm, the average ion current density on the beam spot is ~10 to ~100 pA/cm^2.

2.4.4 Primary Ion Energy and Angle of Incidence at the Target

The primary ions are incident on the grid at an angle of 20^o from the normal, then pass through the secondary ion accelerating field between the grid and the target. Consequently the energy and angle of incidence of the ions at the target depend on both primary and secondary ion accelerating voltages, the latter illustrated in fig. 2.14.

When a positive potential $V_s = |V|$ is applied to the target to accelerate positive secondary ions, the positively charged primary ions with energy q_pV_p are decelerated and deflected in the region between the grid and the target. Their energy at the target is always $q_p(V_p - |V|)$, but the angle of incidence increases sharply from 20^o as V_p approaches V_s. When $V_p = 1.13V_s$ ions will not reach the target. Thus primary energies are available from $1.13V_s$ to the limit set by the maximum value of V_p.

Conversely, when a negative potential $V_s = -|V|$ is applied to the target to accelerate negative secondary ions, the primary ions are given an additional energy $q_p|V|$ as they are accelerated from the grid to the target. Thus for negative secondary ions, incident primary beam energies less than $q_p|V|$ are not accessible, and the primary beam energy at the target is $q_p(V_p + |V|) = q_pV_p + q_p|V|$, i.e., the initial energy plus $q_p|V|$. A negative potential also reduces the angle of incidence.

Under typical operating conditions, $V_p = 18$ kV and $V_s \leq 10$ kV, the angle of incidence does not deviate from 20^o by more than a few degrees.

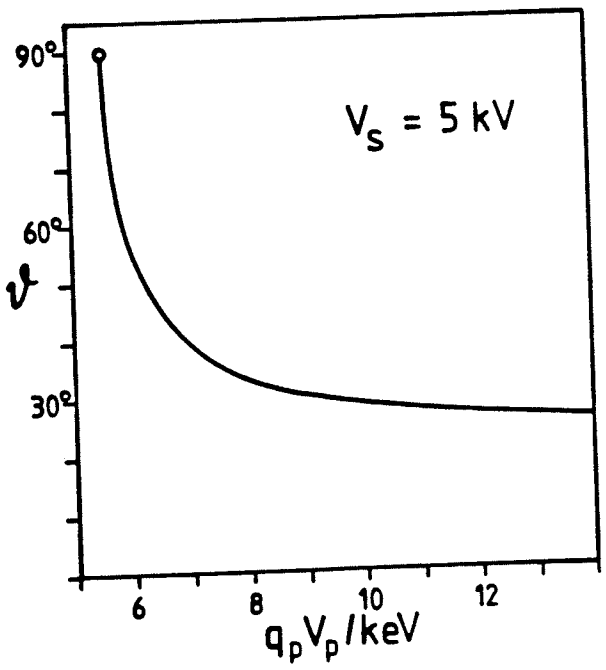

Figure 2.14 Angle of incidence of the primary ions at the target vs. the primary ion energy q_pV_p at the grid, for a secondary ion accelerating voltage $V_s = 5$ kV. The primary ion energy at the target is always $q_p(V_p - V_s)$, but the angle of incidence increases sharply for $V_p < 8$ kV. Primary ions with the energy < 5.66 keV will not reach the target.

2.5 ION DETECTION

2.5.1 The Detector

Secondary ions are detected at the end of the flight tube by a chevron microchannel electron multiplier (50) illustrated in fig. 2.15. Two Varian multichannel plates (1.8 cm diameter (VUW8900ZS) or 4 cm diameter (VUW8920ES)) are separated by a 250 μm stainless steel ring and mounted 1 mm from a stainless steel collector. This type of detector is well suited for time-of-flight measurement because of its large active area and good time resolution. Three 90% transmission grids (Buckbee Mears Co.) separated by 1.8 cm are mounted 2 cm in front of the detector

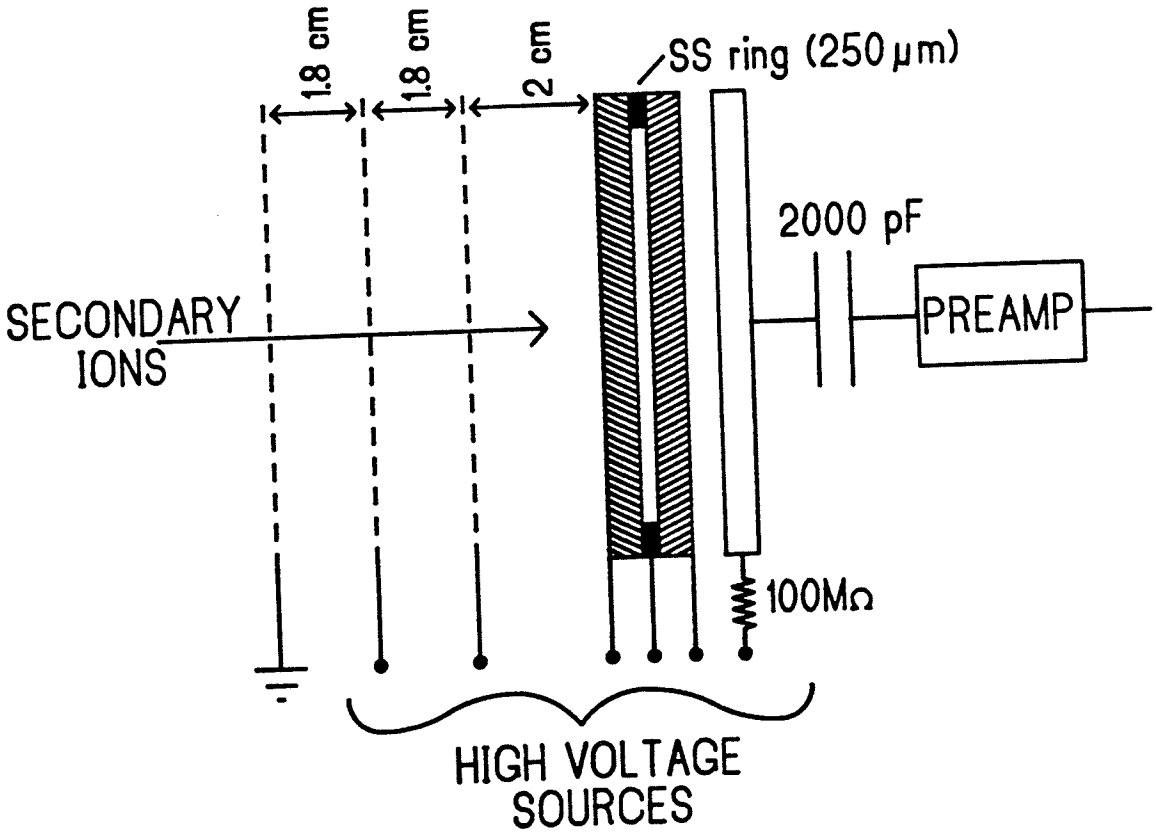

Figure 2.15 Chevron microchannel electron multiplier and post-acceleration/retarding grids.

assembly. These are used for post-acceleration or for analysis of metastable decay patterns.

The plates consist of an array of continuous dynode electron multipliers (~12 μm diameter) oriented at a small angle (~5°) to the plate normal. The bias angle increases the probability that an incoming ion strikes the channel surface. The plates are mounted with opposing bias angles to reduce ion feedback (this is the process where positive ions formed by secondary electrons near the channel exits are accelerated back in the channel and initiate a second electron cascade). Typically 1 kV is placed across each plate and 200 V is placed between the second plate and the collector. In this configuration, an electron gain of $\sim 10^7$ is achieved. The output pulse has a risetime of ~0.5 ns and a width of ~1.5 ns.

2.5.2 Radial Velocity Distribution

The number of secondary ions that strike the detector is determined by the angular spread resulting from the radial velocity distribution and the size of the detector. The radial velocity distribution was determined by measuring the counting rate as a function of voltage on the secondary deflection plates C in fig. 2.1. The experimental points in fig. 2.16 show typical results for fragment ions from alanine. The profiles were the same for both the horizontal and vertical deflections; they were also independent of primary ion energy. The experimental results were compared with profiles calculated for an initial radial velocity distribution of the form $dN/d\epsilon_r = A_r e^{-\lambda_r \epsilon_r}$, where $\epsilon_r = 1/2 m v_r^2$, and m and v_r are the mass and radial velocity of the

ion (51). Thus $1/\lambda_r$ characterizes the width of the distribution at 1/e of the maximum. The fringing fields of the deflection plates were taken into account (eq'n 2.2, ref.49) in the calculations.

Fig. 2.16 shows the profiles calculated for three values of λ_r; the experimental results are consistent with a radial distribution having a width $1/\lambda_r = (0.22 \pm 0.03)$ eV for the alanine fragment at m/z 44. The experimental points for the protonated molecular ion were consistent with a distribution of the same width, but the Na^+ ion had a narrower distribution, with

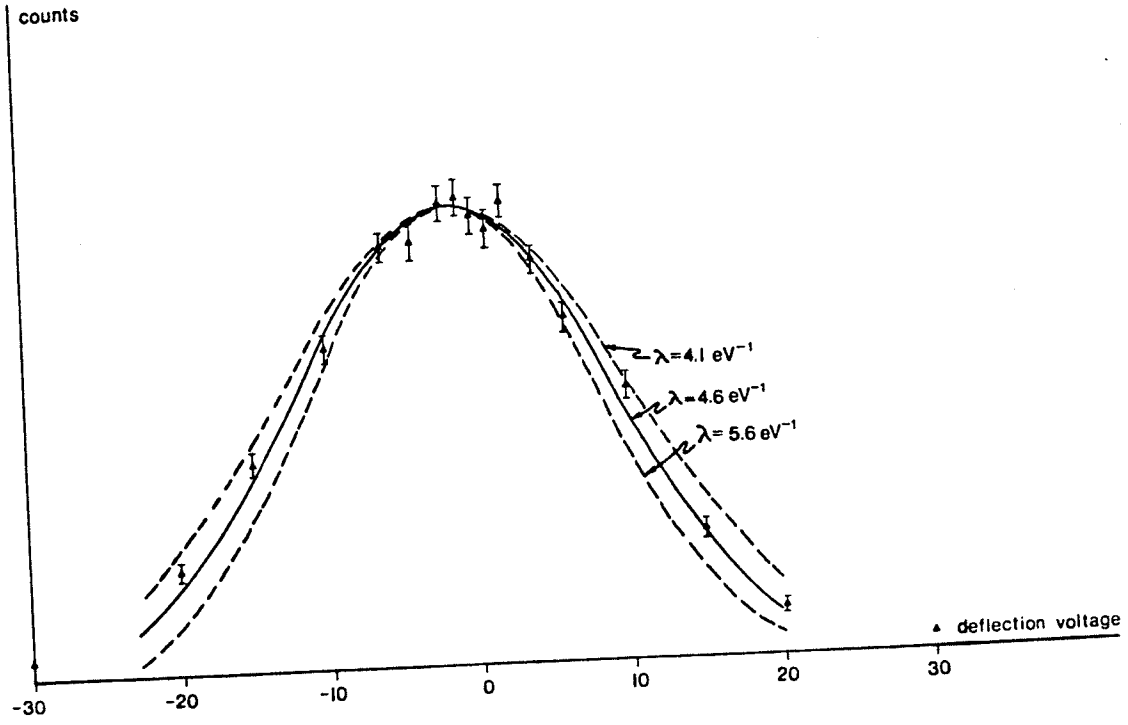

Figure 2.16 $(M+H-HCOOH)^+$ secondary ions detected from alanine as a function of voltage on the deflection plates shown in fig. 2.1. The curves shown are those calculated for $\lambda_r = 4.1$, 4.6,and 5.8 eV^{-1}. Primary ions 5 keV Cs^+, secondary ions 1 keV. The raw data is displayed with no background subtraction. The points at ± 30 V correspond to the background level; i.e., no distinct peaks were observed at these deflection voltages.

$1/\lambda_r = (0.14 \pm 0.02)$ eV. These values gave profiles which fitted the experimental results for secondary ion energies between 1 and 8 keV. When the deflection plates are adjusted to centre the secondary beam, $\gtrsim 90\%$ of the secondary alanine ions at 10 keV hit the 4 cm detector.

2.5.3 Detection Efficiency

Detection efficiency per unit mass for a water cluster depends on its velocity as illustrated in fig. 2.17. A similar dependence is expected for other ions. Velocity thresholds for efficient detection (more than 1 electron emitted per ion) of these large water clusters incident on Cu were determined by Beuhler and Friedman (52) in the range 1×10^6 cm/s to 1×10^7 cm/s. Detection (with unknown efficiency) of large molecular ions with velocity in this range is not uncommon: e.g. 10 keV CsI clusters with $m/z > 10\ 000$ (velocity = 1.4×10^6 cm/s) are reported in chapter 6; 20 keV molecular ions from porcine

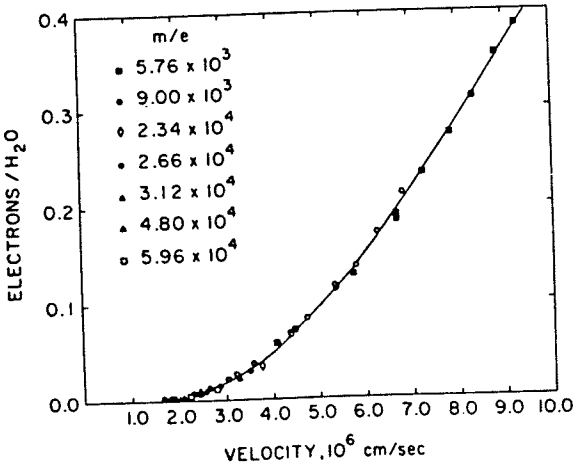

Figure 2.17 The average yield of electrons per water molecule in each cluster is plotted as a function of ion velocity. Symbols indicate different primary ion m/z ratios from which these reduced efficiencies were obtained. Taken from ref. 52.

iso-phospholipase A_2 with m/z 13 980 (velocity = 1.7×10^6 cm/s) have been observed using fission fragments (12). Campana et al (53) have detected 3 keV CsI clusters of m/z 18 600, with velocity (5×10^5 cm/s) below the reported threshold. In the last case, the detector had been implanted with Cs because of a long run on CsI and this may have increased its efficiency.

It is difficult to estimate the detection efficiency of ions with velocity near the threshold from the measurements of Beuhler, but it is clear that some improvement may be realized by post acceleration. Recently potentials up to 5 kV have been placed between the final grid and the front plate of the detector. This increases the velocity of a 10 keV ion with m/z 10 000 from 1.4×10^6 cm/s to 1.7×10^6 cm/s.

2.5.4 Metastable Ions

A large fraction of the ions produced from large molecules by keV ion bombardment are found to be metastable. The importance of this effect in a fission fragment spectrometer was emphasized by Chait et al (54,55). The phenomenon was first observed here (22,27,28) using the secondary ion deflection plates C in fig. 2.1; these plates are ~50 cm downstream of the target. Fig. 2.18 shows the positive and negative spectra of 5'-AMP near the molecular ion peaks. The upper curves are the normal spectra, while the lower ones are the spectra obtained when charged particles are deflected out of the counter by applying 1000 V across the deflection plates. The counts observed then presumably arise from neutral fragments produced by disintegration of ions in the first 50 cm (~10 μs) of flight. Clearly a substantial

proportion of the $(M+H)^+$ and $(M-H)^+$ ions have lifetimes $\leq 10\,\mu s$, while the $(M+Na)^+$ ions are considerably more stable. Similar behavior has been observed in many of the compounds studied.

The observation of the disintegration products at the same position as the parent ion is a particular property of a linear time-of-flight spectrometer. If an ion decomposes in the field-free flight path, each fragment retains the velocity of its parent ion apart from a small contribution from the kinetics of the disintegration. The fragment therefore appears at the approximate position of the parent ion in the time-of-flight spectrum, but the peak is broadened because of the energy gained in the break-up. Decompositions ocurring during acceleration produce tails on parent or fragment ion peaks. The implications of metastable decay on the performance of time-of-flight measurement have recently been described in detail by Chait et al (34,56) and are discussed in chapter 4.

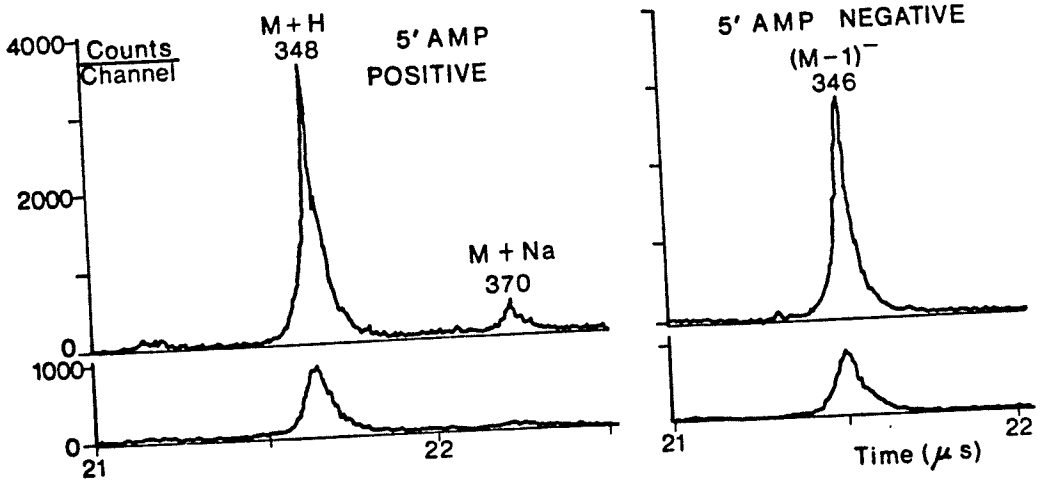

Figure 2.18 Time-of-flight spectra of positive and negative ions from 5'-AMP. The upper spectra are the normal ones; the lower spectra are taken with 1000 V applied across the deflecting plates C of fig. 2.1.

The grids shown in fig. 2.16 were originally inserted to study patterns of metastable decay. For this purpose, the detector and the entrance grid are maintained at ground potential but a retarding potential is applied to the central grid. This does not change the time-of-flight of neutral fragments, but charged particles are delayed. The delay is larger for charged fragments (mass m_f) than for the parent ion (mass m_p), since the fragment has only a fraction ($\approx m_f/m_p$) of the parent energy; if the energy of the fragment is too low, it will be reflected. This enables examination of the mass spectrum at the time the ions arrive at the detector. This feature was used to study the decay pattern of CsI clusters (chapter 6).

CHAPTER 3

DATA ACQUISITION AND ANALYSIS

3.1 INTRODUCTION

The signal that triggers the deflection pulse V_{def} for the primary beam also provides the "start" pulse for the timing circuits. Amplified pulses from the detector supply the "stop" signal. Thus the start is synchronized with the arrival of the primary ion burst at the target, and the stop with the arrival of a secondary ion at the target.

Two methods of time measurement have been used: originally time-to-amplitude conversion (TAC) followed by analogue-to-digital conversion (ADC) and more recently direct time-to-digital conversion (TDC). The data storage and analysis hardware used in the original configuration are shown in fig. 3.1. Spectra were acquired in a Norland Corp. Pulse-Height Analyser Inotech Ultima/2 IT3408. Initially (fig. 3.1a) this was also used to perform simple analysis, the results of which could then be printed on a Teletype. Spectra were plotted with an Hewlett

Packard HP7004B X-Y Recorder connected to the pulse-height analyser. The raw data then had to be deleted before the next run could begin. This system was used because much of the necessary

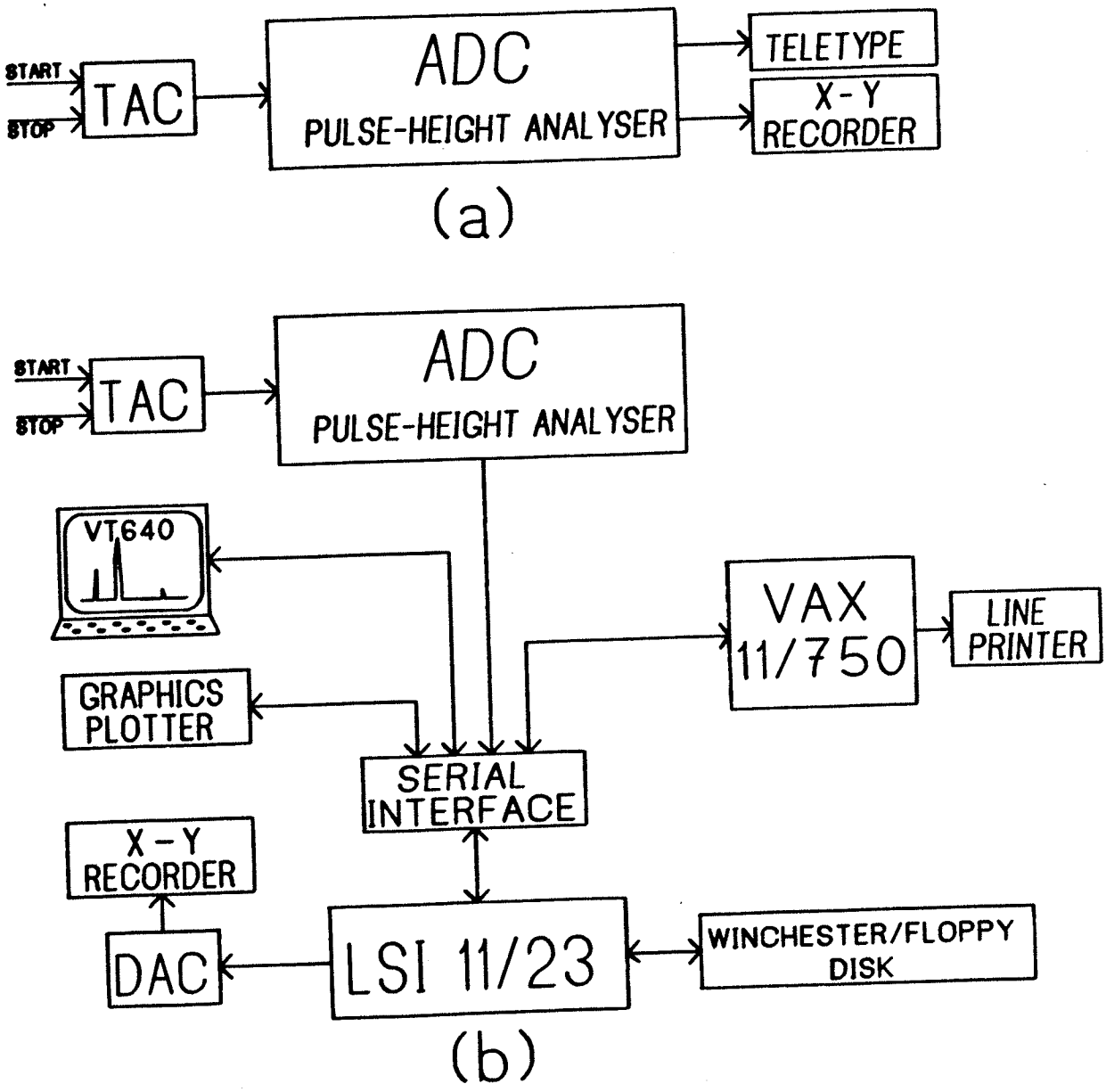

Figure 3.1 Data storage and analysis hardware using time-to-amplitude conversion a) initially, b) with an LSI 11/23 computer. The VT640 terminal is a DEC VT100 with Digital Engineering Retrographics. A DEC DLV11J serial interface provides four RS232 output ports. One of these is connected to the cyclotron laboratory VAX 11/750 computer to permit use of their Printronix P300 line printer. Details of the data acquisition are shown in fig. 3.3

electronics (see fig. 3.3) could be borrowed from the Cyclotron laboratory and the pulse-height analyser was also available in the department.

In late 1981 a DEC LSI 11/23 computer was acquired to provide more sophisticated display and analysis and permanent storage of the raw data (fig. 3.1b). Here, after a spectrum was taken with the pulse-height analyser it was transferred to the LSI 11 via an RS232 serial link. Then it could be be displayed and analysed on a VT640 terminal. At first, hard copy was obtained with a Data Translation DT2766 Digital-to-Analogue Converter (DAC) and the X-Y recorder and later with an Hewlett Packard HP7470A Graphics Plotter through a serial link. Permanent data storage was provided by a Data Systems Design, Inc. DSD880 7.8 Mbyte winchester and 1 Mbyte floppy disk.

In the summer of 1983, a new data acquisition system based on the LeCroy Research Systems SA Model 4208 TDC was implemented. The hardware for this system is illustrated in fig. 3.2. The TDC is controlled via CAMAC with the LSI 11 computer; the spectrum is histogrammed in computer memory. Data storage and analysis uses the same hardware as above (fig. 3.1b).

Most of the data presented here were taken using the former method (fig. 3.1a or b).

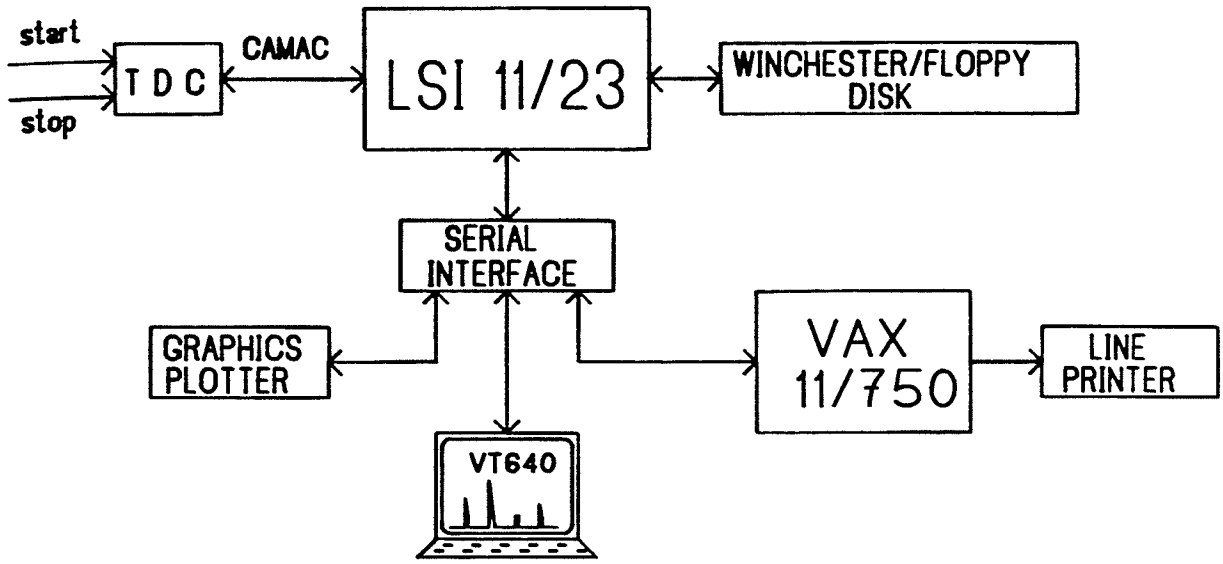

Figure 3.2 Data analysis and storage hardware using time-to-digital conversion. Details of the data acquisition with this system are shown in fig. 3.5.

3.2 TIME-TO-AMPLITUDE, ANALOGUE-TO-DIGITAL CONVERSION

3.2.1 Data Acquisition

In the initial configuration (22) (fig. 3.1), time-of-flight was measured by conventional nuclear timing circuits, as shown in fig. 3.3. Amplified pulses from the electron multiplier triggered a discriminator, which supplied the "stop" signal for a time-to-pulse-height converter (TAC). The "start" signal for the TAC was provided by a precision time-mark generator, which also triggered the pulser which delivered the deflection pulse V_{def} for the primary ion beam. The TAC was "stopped" when a secondary ion was detected. The TAC output, proportional to the time interval

Figure 3.3 Timing circuits used in the TAC-ADC configuration. The example shows the timing sequence for primary pulses separated by 200 μs and the TAC start delayed by 30 μs with respect to the ion gun pulse. The ungated trigger pulses are shown as dashed lines; pulses separated by 10 μs are shown for clarity, although the normal separation was 1 μs. The apparatus not already specified was: Tektronix Inc. Model 184 Time-Mark Generator; Ortec Inc. Model 416A Gate and Delay Generator; Ortec 442 Linear Gate and Stretcher; Ortec 467 Time-to-Pulse-Height Converter; Ortec 416A Gate and Delay Generators; Ortec 463 Discriminators; Ortec 142B Preamplifier 142B; Ortec 454 Timing Filter Amplifier; Ortec 441 Ratemeter; E-H Research Laboratories E-H131 Pulse Generator; Canberra Industries Model 1473 Scaler; Inotech Pulse-Height Analyzer Ultima/2, IT 3408; Analogue Technology Corp. Model 170 Current-to-Frequency Converter.

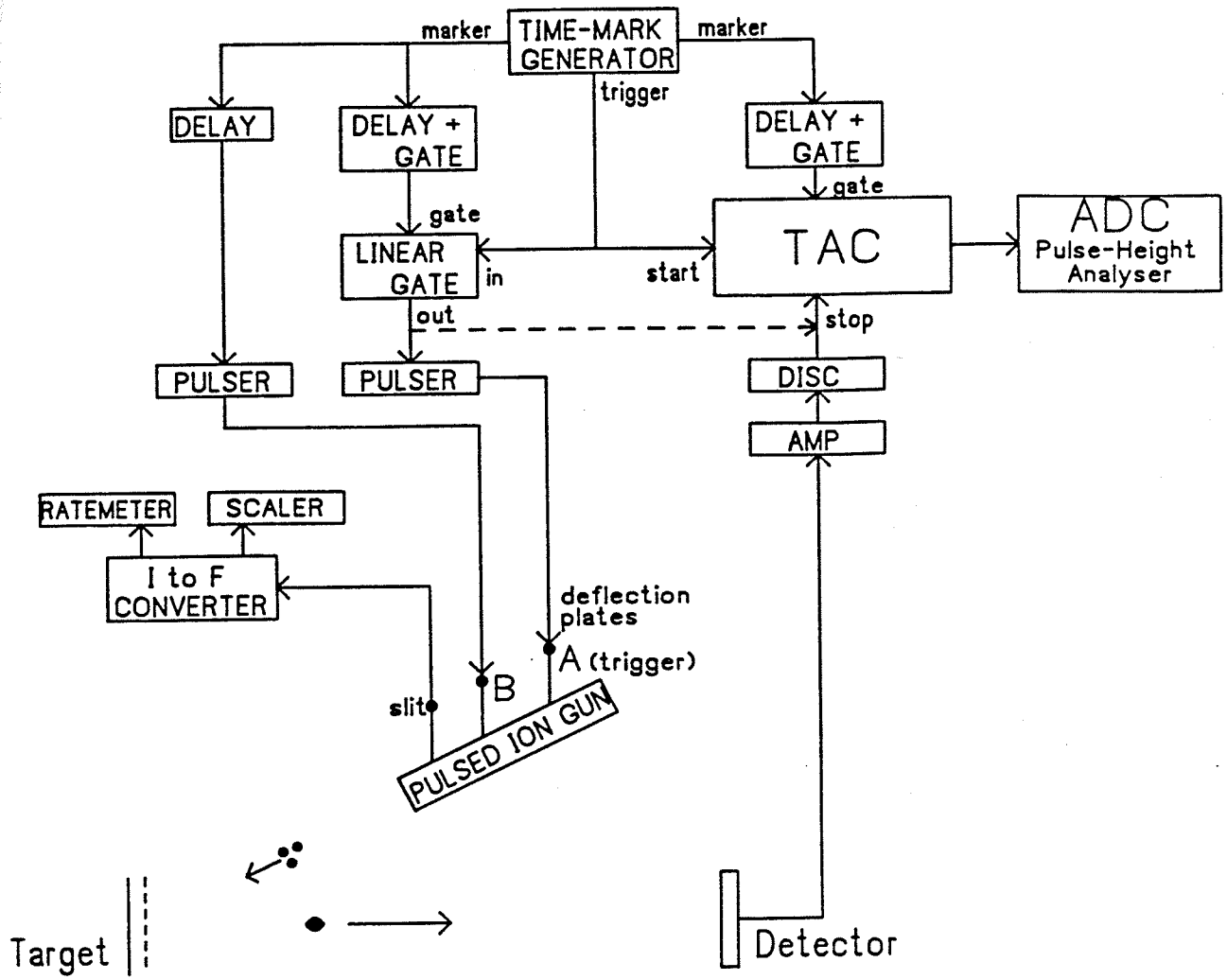
marker
TIME-MARK GENERATOR
marker
trigger
DELAY
DELAY + GATE
DELAY + GATE
gate
gate
LINEAR GATE
in
start
TAC
ADC
Pulse-Height Analyser
out
stop
PULSER
PULSER
DISC
AMP
RATEMETER
SCALER
I to F CONVERTER
deflection plates
A (trigger)
B
slit
PULSED ION GUN
Target
Detector

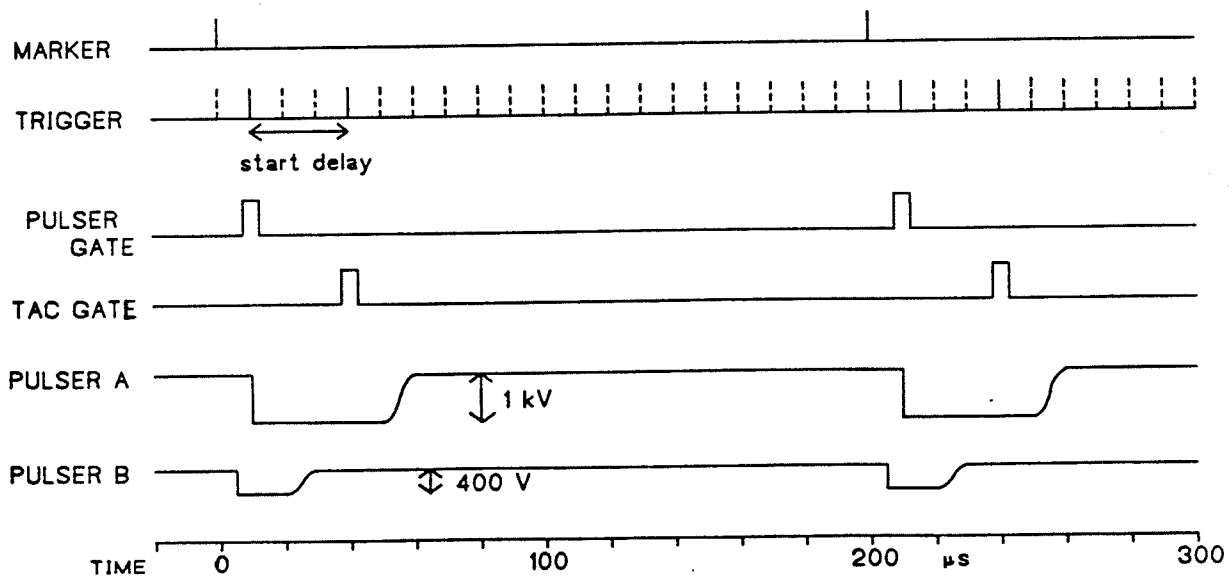
MARKER
TRIGGER
start delay
PULSER GATE
TAC GATE
PULSER A
1 kV
PULSER B
400 V
TIME
0
100
200
µs
300

between the start and stop, was connected to an ADC, whose output was recorded and displayed by a pulse-height analyser. When examining a complete mass spectrum, typically 4000 channels of ~15 ns/channel, or a total timing period of ~60 μs, were used.

At high counting rates several ions may arrive at the detector in a given timing period, but this system is capable of measuring only one. When more than one particle is detected in a given period, only the earliest one (the one of lowest mass) is registered. This can produce significant distortion of the spectrum, particularly for large biomolecules, where the molecular ions may be several orders of magnitude less intense than the fragments. The effect was reduced by running at TAC counting rates $\lesssim 10\,\%$ of the pulser rate. When the whole spectrum was being examined, the ion beam current was reduced to a value which gives a counting rate within this limit. The loss of counts for ions of high mass was then $\lesssim 10\,\%$ provided that there was no correlation between the production of such ions and of fragments of lower mass. When examining high-mass ions it was usually more satisfactory to reduce the counting rate by delaying the TAC start, as described below. Only heavy ions - i.e. those arriving after the TAC start - were then recorded, and the abundant low-mass ions did not contribute to the distortion.

In its simplest form, the system has reduced accuracy for long conversion times, because of the non-linearity and jitter present in the analogue TAC and ADC circuits. For example, minimum specifications for the TAC used here (see fig. 3.3) require a time resolution of 0.01% of full range, integral nonlinearity of 0.1% of full range, and a temperature stability

of 0.015%/°C. Thus for a 40 μs timing period a time resolution no better than ~4 ns and nonlinearities of ~40 ns could be expected. Recent measurements with the TDC, indicate the situation was considerably worse. The errors could, however, be reduced by delaying the TAC start signal by a fixed amount, which was conveniently done here by use of the time-mark generator. This unit has two synchronized outputs ("marker" and "trigger") whose periods may be set independently as multiples of the period of the reference oscillator (0.1 μs).

The "trigger" output was used to trigger both the TAC start and the primary ion gun (see fig. 3.3). However, they were only effective when coincident with the "marker" output after passing through separate variable delays. Thus the start could be delayed with respect to the deflection pulse by any multiple of the trigger period (usually 1 μs). The timing for a typical case is shown in fig. 3.3. Since the error in "trigger" timing is determined by the stability of the 10 MHz reference oscillator (0.0003% in 24 h), a long time of flight could be measured with an accuracy corresponding to a much shorter time interval.

The linearity of a given timing period was calibrated in a similar way, but with the ion gun pulser input feeding the TAC stop as shown by the dashed line in fig. 3.3. As the gating signal delay was changed, calibration peaks were recorded over the whole time spectrum; 1 μs intervals were normally adequate.

3.2.2 Data Analysis of Pulse-Height Spectra

The original method of data analysis (fig. 3.1a) used the applications program supplied with the pulse-height analyser to search the spectrum for peaks and calculate their centroids and intensities. These were then printed with the Teletype and subsequent analysis (see below) was performed manually.

With the LSI 11 (fig. 3.1b) pulse-height spectra were stored permanently and could be analysed interactively using the VT640 graphics terminal. Cursors were used to select mass calibration peaks and background regions if a smooth background was to be subtracted. The mass and intensity corresponding to individual peaks could then be determined separately using cursors or by an automatic peak searching routine. In the latter case, a table of results was stored in a separate file which could be examined at the terminal or printed on the line printer. The algorithms used to calculate peak centroids, fit the background and perform the peak search are described in Appendix B.

The peak centroids were corrected for non-linearity of the analogue circuits by linear interpolation between the time marker peaks mentioned in the previous section. Thus the corrected time t_c was given by $t_c = a_c + b_c \cdot (\text{centroid})$ where a_c and b_c were determined from the centroids of the two bracketing time markers which were stored separately. The mass-to-charge ratio was then calculated from $\sqrt{m_s/q} = a + bt_c$ where a and b were determined from the centroids of two or more peaks corresponding to known masses. If more than two peaks were used, a linear regression was

performed.

If the start was delayed by t_{delay} (fig. 3.3) so that known low mass peaks were cut off, calibration from a previous (low mass) spectrum could be used. Then $b \cdot t_{delay}$ was added to the constant a.

Since the channel width in a typical run is quite wide (~15 ns), accurate centroid determination of the low mass calibration peaks was difficult; many peaks are only ~5 ns in width. A bootstrapping method was therefore usually used to determine the calibration at high mass: The low mass peaks were used to identify obvious fragments of higher mass or the molecular ion which were then used for a more accurate calibration at high mass. The wide bins also degraded mass resolution at high mass in some cases; above $m/z \sim 1000$ the channel width was usually greater than 1u.

The TAC-ADC configuration described here had several disadvantages compared to the present TDC method described in the next section. The analogue circuits limited accuracy in the time measurements and necessitated corrections in the analysis. The single-stop TAC distorted the spectrum at high counting rates; to avoid this the counting rate had to be kept $\lesssim 500$ Hz (10% of the sweep rate). Wide time bins had to be used because the pulse-height analyser has only 4000 channels; this limited the accuracy in determining peak centroids of narrow peaks and degraded the mass resolution at high mass. All these disadvantages could be lessened to some extent by taking the spectrum in

sections but this complicated both the data acquisition and analysis.

3.3 DIRECT TIME-TO-DIGITAL CONVERSION

3.3.1 Data Acquisition

Recently direct time-to-digital conversion has been implemented (fig. 3.2) The TDC is a CAMAC module configured in the present application to accept a common start and up to 8 stops on a single line; each channel hit enables the next one. Dead time between stops is specified as ~3 ns. The unit uses a high stability crystal controlled 125 MHz clock to digitize in real time. Resolution of 1 ns is obtained by digital interpolation between two clock pulses. This is accomplished by dividing the clock signal into 4 signals delayed by 1 ns from each other. Since the clock period is 8 ns, it changes state every 4 ns so one of the 4 signals changes state every ns. Nanosecond resolution is achieved by identifying the signal that changes state in coincidence with the pulse being measured. Time intervals are encoded in 24-bit signed digital words corresponding to a dynamic range of 8.3 ms. The data are stored in the unit until read and cleared by the computer at the end of each sweep.

This method of time measurement does not produce the spectrum distortion caused by the single stop TAC in the analogue method described in the previous section and the digital circuits are largely unaffected by jitter and non-linearity. Also the TDC

with sufficient computer memory allows much narrower time bins; the present system uses a 32000 channel array compared to 4000 channels on the pulse-height analyser. Consequently the complete mass spectrum may be taken with higher counting rate.

The electronics are illustrated schematically in fig. 3.4. A flow chart of the data acquisition program is shown in fig. 3.5. In contrast to the first method where most of the data handling was performed by hardware, this arrangement relies mostly on software. The TDC is controlled from a VT640 terminal with the LSI 11/23 run under the RT11 operating system. Data are stored in a 32000 word $\times$ 16 bit histogram in extended memory. The use of extended memory in RT11 prohibits the use of interupts so the usual type of data acquisition program - where the interactive display routine is interupted by the TDC when data are available - could not be used. Instead the TDC is polled for a "look-at-me" (LAM) which is set externally ("end of window" (EDW) on the TDC) a selected delay (0 - 100 μs) after the start. At given intervals (say every 1000 sweeps) the terminal is checked for a command. The slit current is also measured at these intervals by reading the counts accumulated in the scaler/timer over a fixed time (usually 1 s). This "instantaneous" current multiplied by the number of sweeps is accumulated for normalization.

Since accessing extended memory is slow (~100 μs) the program controls the primary pulse repitition rate; a new cycle is initiated after the data from the TDC is read. Thus, if no data are present in a given sweep, the next one begins immediately. This also allows the histogramming and the time digitization tasks to be overlapped to some extent; after the

Figure 3.4 Timing circuits used for time-to-digital conversion. The LSI 11 initiates each sweep by triggering the TDC start and the primary ion gun. The same signal is passed through a variable delay and fed to the "end of window" input on the TDC. This sets a LAM ("look at me") which signals the computer to read the data from the TDC. The time between sweeps depends on the the amount of data to be read. Pulses outside of the window defined by the "stop veto" are ignored by the TDC. Additional apparatus used here (see also fig. 3.3): BiRa Systems Inc. Model 5000 Powered Camac Crate; BiRa Model 1311 BRQ Bus Controller; BiRa Model 3251 NIM Out Module; BiRa Model 2101 Scaler-Timer; Schlumberger Model 7174 Quad Constant Fraction Discriminator; EG&G Inc. Model GG200/N Gate Generator; Ortec 9305 Fast Preamp

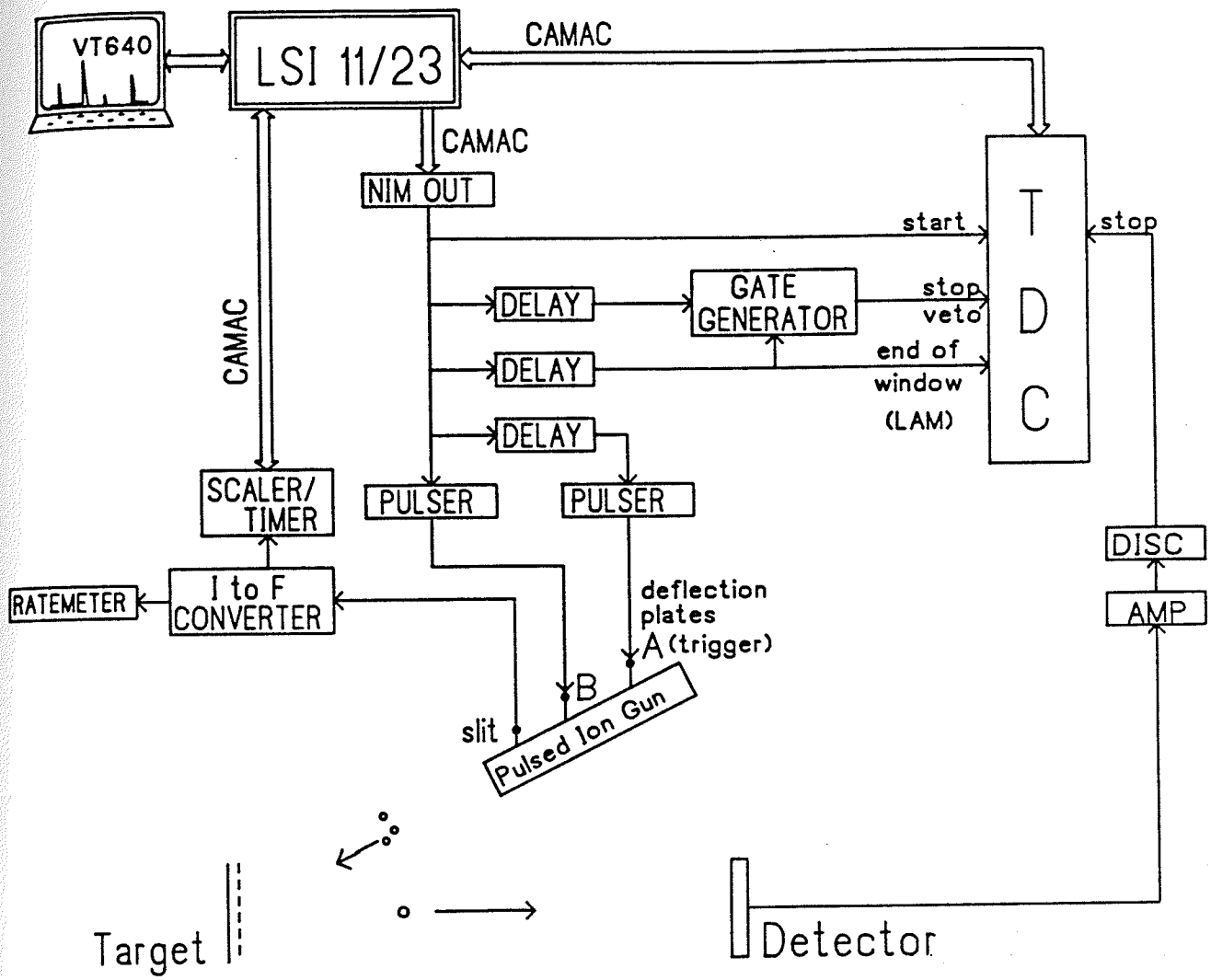
VT640
LSI 11/23
CAMAC
CAMAC
NIM OUT
CAMAC
start
stop
T
D
C
DELAY
GATE
GENERATOR
stop
veto
DELAY
end of
window
(LAM)
DELAY
SCALER/
TIMER
PULSER
PULSER
DISC
AMP
RATEMETER
I to F
CONVERTER
deflection
plates
A (trigger)
B
slit
Pulsed Ion Gun
Target
Detector

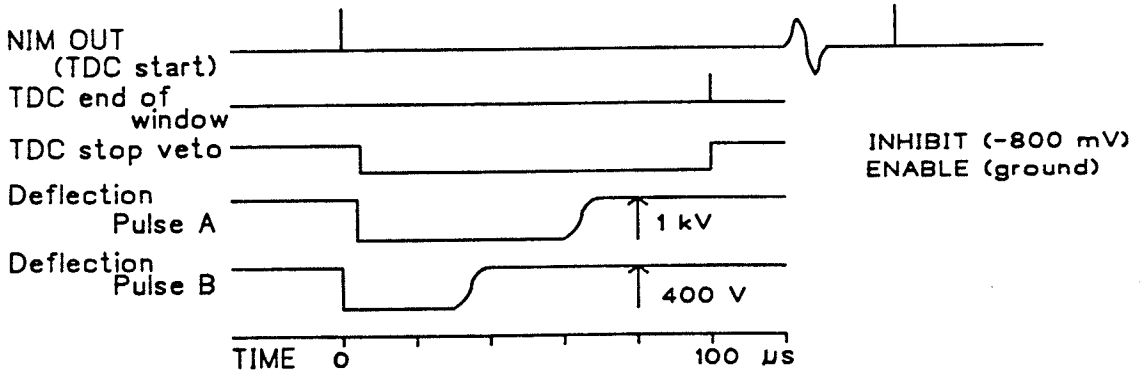
NIM OUT
(TDC start)
TDC end of
window
TDC stop veto
Deflection
Pulse A
Deflection
Pulse B
1 kV
400 V
TIME
0
100 µs
INHIBIT (-800 mV)
ENABLE (ground)

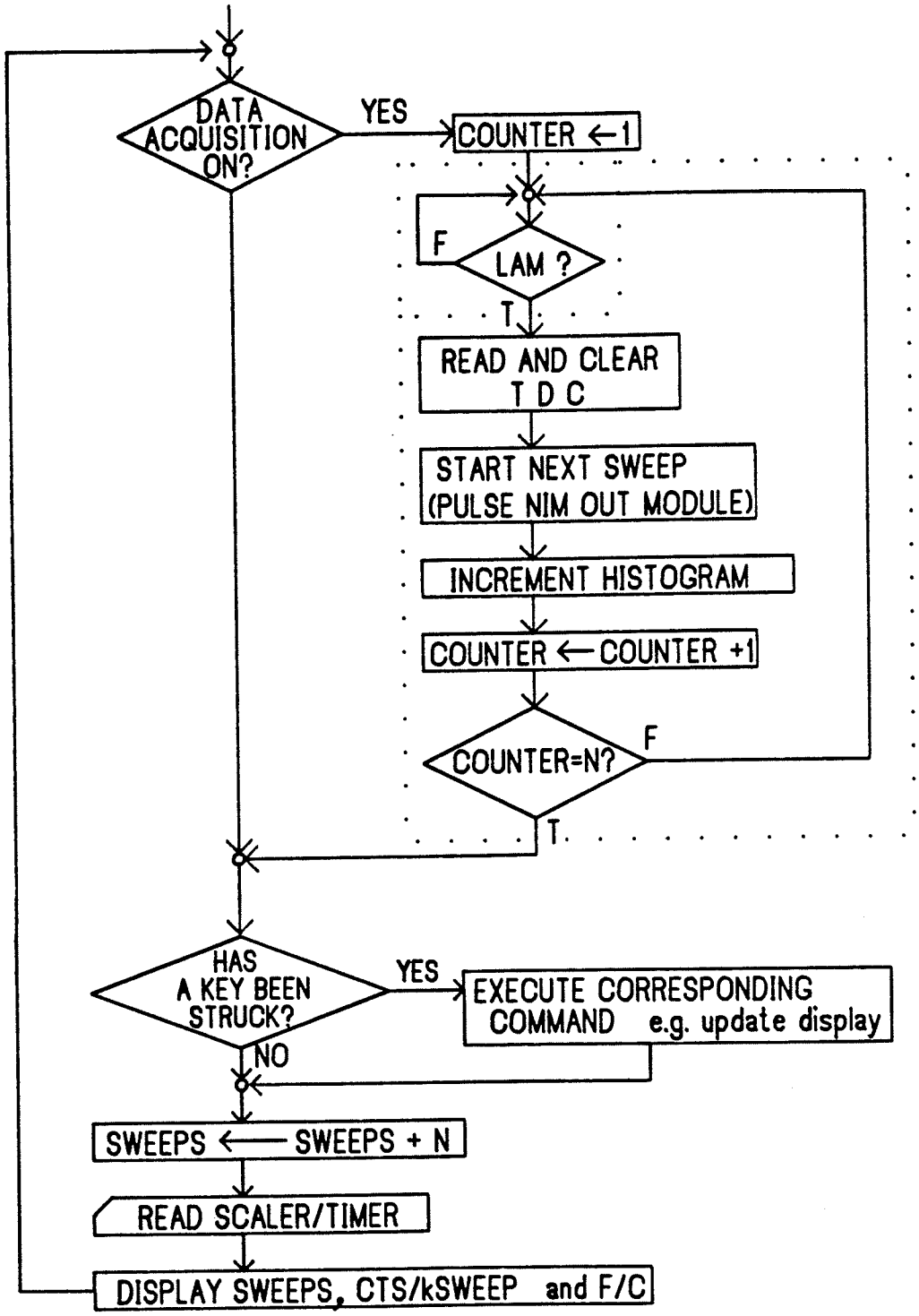

Figure 3.5 Flow chart of the TDC data acquisition program. Because of restrictions on the use of interupts with the LSI 11, the TDC is polled for a "look-at-me" (LAM) (inner dotted box). When one is detected, the data is read from the TDC and another sweep is initiated. This procedure is repeated a specified number (N) of times (outer dotted box) and then a command is accepted from the terminal and various displayed acquisition parameters are updated. The data acquisition may be turned off in which case the program is devoted to accepting and executing commands.

data are read into the low memory and digitization for the next sweep has started, the data are moved into extended memory (see fig. 3.5). The sweep rate is ~3 kHz if 0 or 1 datum is present per sweep, but slows to $\lesssim$ 500 Hz if 8 events are detected per sweep. This corresponds to a maximum total count rate of ~4 kHz (compared to 500 Hz for the analogue configuration) although the present ion source limits counting rates to ~2 kHz with this system.

Stop pulses before an externally selected time ("stop veto" on the TDC) are ignored by the TDC. This may also be done with software as described below, but it is slower and each early event uses a channel on the TDC. The stop veto is used mainly to inhibit pick-up from the deflection pulses since these occur in every sweep.

Within the time window determined by the external pulses (stop veto and EDW) a time window may be selected, outside of which data from the TDC are ignored by the acquisition program. The size of the window is limited by the size of the histogram array. With maximum resolution of 1 ns, the 32000 channel array limits the window width to 32 μs. Larger time windows are allowed with wider bin widths; any multiple of 1 ns may be selected.

Any portion of the incoming spectrum may be displayed on the terminal. Since data acquisition is suspended while the display is updated, and since the horizontal resolution of the terminal is only 640, a combination of binning and sampling is used to speed up the display routine.

Since the spectrum array uses only 16 bit words, there is a possibility of overflow in the intense low mass peaks; after $64K = 2^{16}$, the channel contents revert to zero. To prevent this, the data rate below a selected channel may be suppressed by a selected factor. For example, to suppress the spectrum below 10 μs by a factor of 10, ions with a flight time < 10 μs will be recorded only 1 sweep out of 10.

The data acquisition program also records the multiplicity distribution - the number of sweeps in which 0,1,2,...,8 events were observed.

3.3.2 Data Analysis of TDC Spectra

After the spectrum is accumulated in core memory, any portion of it may be stored on disk. The data acquisition details (bin width, run time etc.) are stored automatically with the spectrum.

The TDC spectra are analysed in the same way as the pulse height spectra (§3.2.2) except that the correction for non-linearity is not performed. Also, since the complete spectrum is taken each time with narrow bin width, a single calibration with low mass peaks is usually sufficient.

CHAPTER 4

PERFORMANCE

4.1 SENSITIVITY

Aspects of time-of-flight mass spectrometry with sophisticated computer control have been described by Macfarlane (57). In principle time-of-flight instruments have a significant advantage over sector-field instruments in sensitivity (58). Such an instrument is set to transmit ions of all masses simultaneously and the measured flight time from each ion* is used to increment the corresponding channel of the histogram. Thus the secondary ions produced in the whole measurement are integrated; no secondary ions are wasted except the ones that miss the detector altogether or the ones that hit the detector but fail to give an output pulse above threshold.

This is considerably different from the operation of a sector-field spectrometer in the usual scanning mode. In that

* Some data may be lost when the single stop TAC is used but this effect may be kept small (§3.2.1).

case the instrument is set to transmit a certain mass at any given instant of time. Ions of all other masses are rejected, giving a reduction in efficiency which depends on the scanning range and the width of the mass window. In this respect the time-of-flight spectrometer is similar to the sector-field spectrograph with photographic plate detection, which also integrates ions of various masses.

A second limitation on the efficiency of any spectrometer is provided by the finite apertures through which the beam must pass. In the sector-field spectrometer these may include an object or source slit and the magnet aperture. In the time-of-flight spectrometer there are no slits, so its transmission is high ($\gtrsim 10\%$), limited mainly by the finite size of the detector.

The property of a time-of-flight instrument that allows fragments from metastable decay in the flight tube to be detected at the position of the parent ion (§2.5.4) provides a further advantage in sensitivity. An ion needs to remain intact only during acceleration (~100 ns for m/z 1000 at $V_s = 10$ kV) to contribute to the peak integral. In contrast, in a sector-field (or curved time-of-flight) instrument, if an ion breaks up at any time during its flight (usually tens of microseconds) it will not be detected - at least not at the position of the parent.

These advantages allow mass spectra to be obtained with low primary flux density; the typical current density of 50 pA/cm^2 is much smaller than that usually used with magnetic and quadrupole instruments (59-61) and a factor ~10^6 lower than those sometimes used in fast atom bombardment (17). Thus the time-of-flight spectrometer may be expected to be particularly useful in cases where

radiation damage is the limiting factor.

To exploit fully the potential for sensitivity, it is necessary to make the sample spots the size of the beam spot (~1 mm diameter) or smaller, and to position it in the path of the primary beam. Until now it has not usually been necessary to economize on sample material so such a procedure has not been perfected although we have obtained smaller spots by electrospraying with a drawn glass capillary (37) instead of a hypodermic needle or by focusing the electrospray (58). An example indicating the present sensitivity is shown in fig. 4.1. Here 150 pmole of methionine enkephalin was electrosprayed onto a

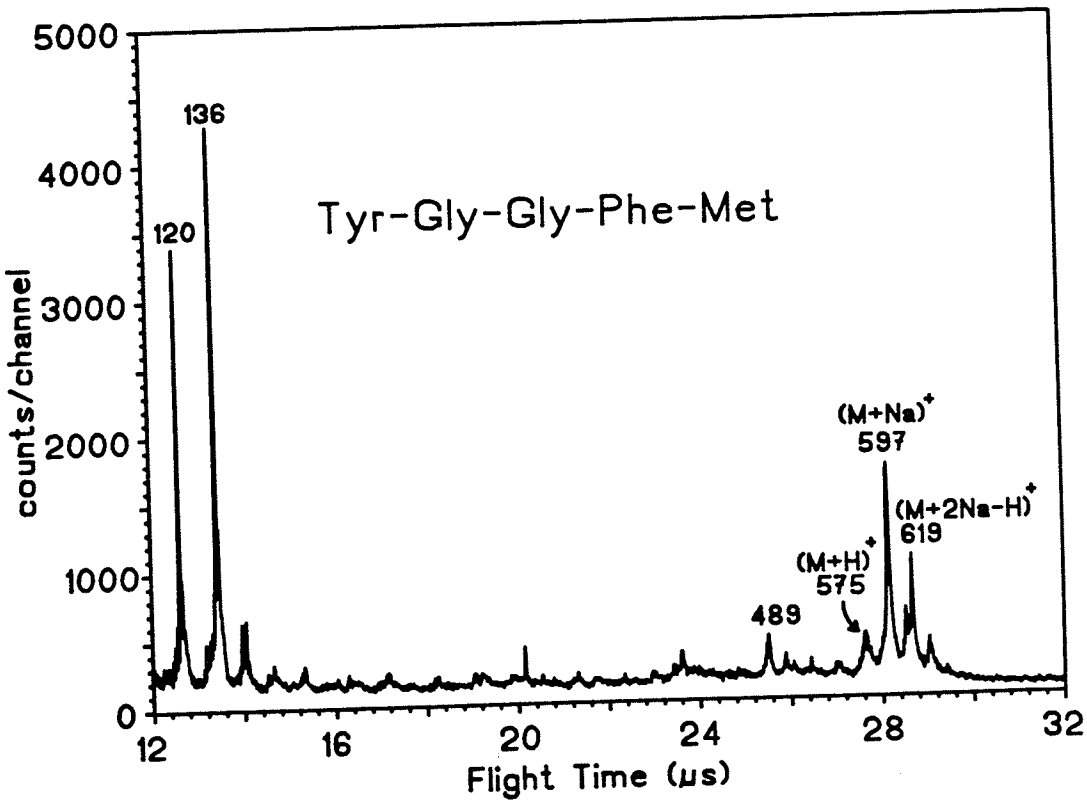

Figure 4.1 Positive ion spectrum obtained from a 150 pmole target of methionine enkephalin. Only ~20 pmole was actually hit by the beam.

~ 3 mm diameter area using a glass capillary. The beam spot diameter is ~ 1 mm so about 20 pmole of target was hit by the beam. The spectrum obtained in a 20 minute run is shown in the figure. In this spectrum 11000 counts are contained in the $(M+Na)^+$ peak. Structural information is available from the fragment ion peaks (27).

4.2 BACKGROUND

The sensitivity of a time-of-flight instrument is somewhat diminished because of the continuous background observed above m/z ~ 100. Such a continuum is apparent in the spectrum shown in fig. 4.1. The problem worsens for heavier molecules as illustrated in the typical spectrum of an oligonucleotide shown in fig. 4.2. Among the sources of background in the Manitoba instrument two may be distinguished: metastable breakup and primary ion leakage.

4.2.1 Background from Metastable Break-up

The continuum caused by metastable decomposition in a time-of-flight spectrometer has been described by Chait (56). The effect of decomposition during acceleration is illustrated in fig. 4.3; charged fragments from break-up between the target and grid have velocity between that of the parent and the fragment from prompt decomposition so they produce a continuum between the

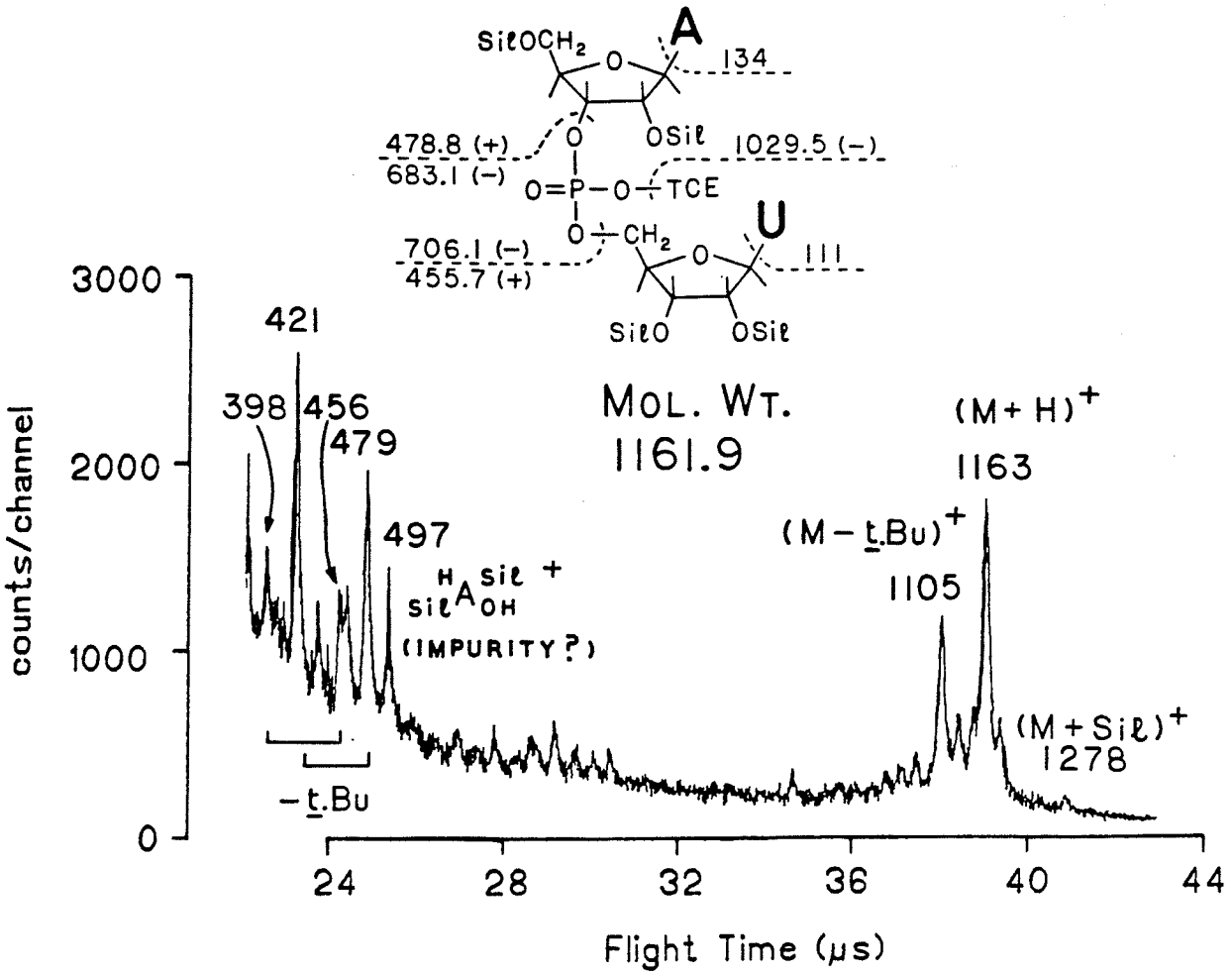

Figure 4.2 Positive ion mass spectrum of the fully protected dinucleotide ApV (see ref. 46 for details) above m/z 400. The spectrum was accumulated in 35 minutes with 8 keV Cs^+ primary ions. The spectrum illustrates the continuous background typical of mass spectra above m/z ~ 200.

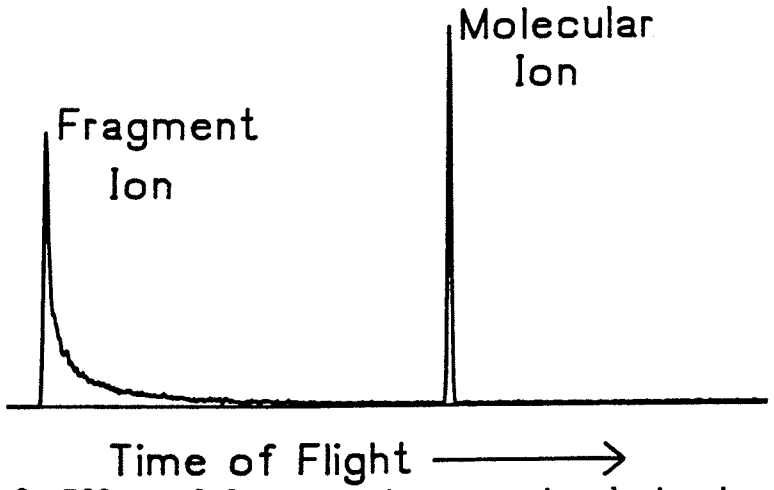

Figure 4.3 Effect of fragmentations occuring during ion acceleration (56). Charged fragments produce background between the parent and fragment peaks; neutral fragments produce a continuum above the parent peak. The data is calculated for 32000 parent ions decaying into two equal fragments (charged and neutral) with a mean lifetime of 1/2 the acceleration time.

peaks. Neutral fragments from break-up in this region always have less velocity than the parent so they produce a continuum above the molecular ion peak.

Fragmentation in the field-free flight tube causes peak broadening (§4.4.2) and the unresolved peaks also contribute to the continuum.

4.2.2 Background from Primary Ion Leakage

In the Manitoba instrument, some background is also caused by primary ions which leak from the ion gun between pulses. The ions strike the target at random times and cause an even continuum. Background resulting from leaking primary ions can be largely eliminated in one of two ways: by pulsing the anode shield (shown in fig. 2.7) or by pulsing the secondary ion deflection plates C (shown in fig. 2.1).

The latter technique takes advantage of the fact that most of the secondary ions produced are light ions (fig. 4.4). The random background therefore results almost entirely from light ions desorbed at random times. To appear in the continuum at high mass, they must pass between the plates later than the heavy ions desorbed by the primary ion pulse. Background is reduced by pulsing the plates to high voltage after the heaviest ion of interest has passed. For the compound of fig. 4.2, the plates are pulsed after the molecular ion (m/z 1163) passes; i.e. ~ 13 μs

after the primary pulse. If the fragment ion at m/z 73 desorbed by a random primary ion passes between the plates just before they are pulsed, then it appears in the spectrum at m/z 300. Thus random background above m/z 300 (due to ions with $m/z \lesssim 73$) is suppressed. The method of pulsing the plates, illustrated in fig. 4.5, is similar to the method used to pulse the primary ion beam (fig. 2.12) but here an FET is used to reduce the fall time of the pulse. This procedure has been used routinely in applications to biological compounds and was used in the spectrum shown in fig. 4.2.

Pulsing the anode shield is effective in reducing background only if the source current has a sharp dependence on the anode shield voltage; each new filament (Appendix A) has different

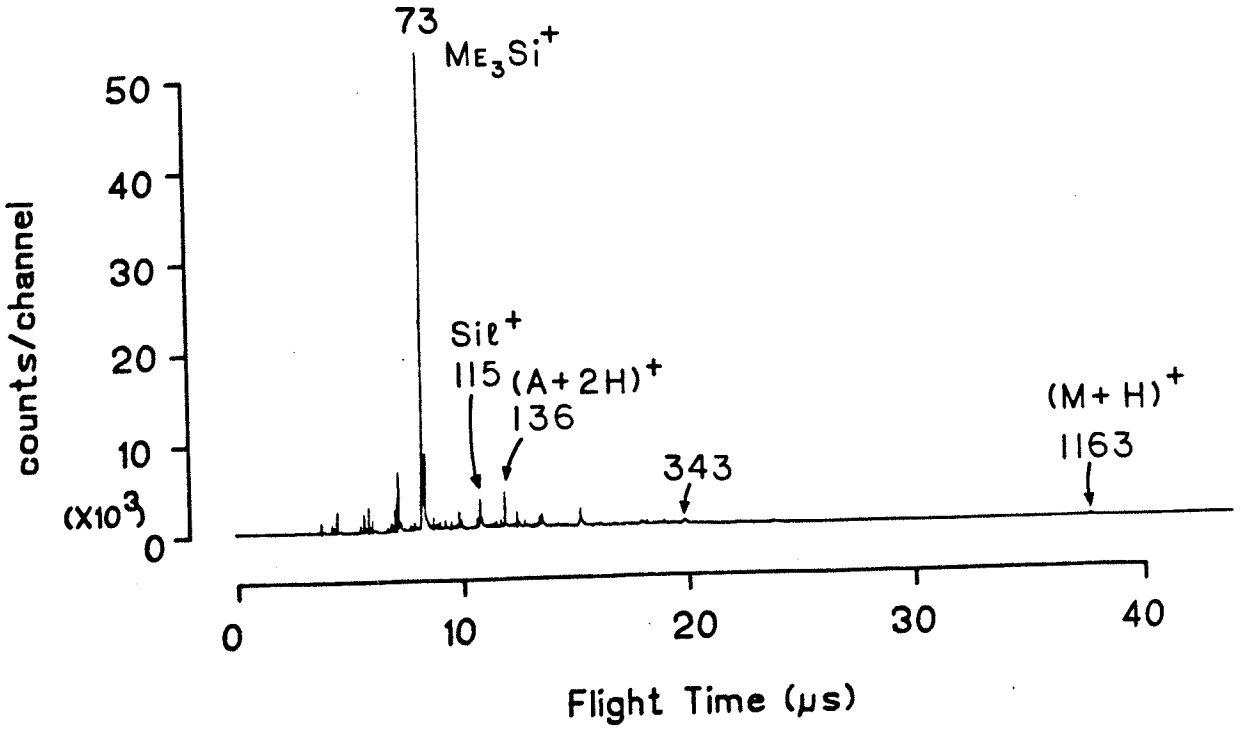

Figure 4.4 The complete spectrum of the same compound illustrated in fig. 2.2. Ions above m/z~150 represent only a small fraction of the total ions detected.

characteristics. As mentioned in §2.4.1 the anode shield voltage is adjusted to optimize the beam current. If the beam current drops significantly when the shield voltage is changed by ~ 50 V, the primary ion leakage can be reduced by "turning off" the beam between pulses. This is accomplished by using a battery powered pulser floating at the primary ion voltage and triggered through an optical isolator.

Depending on the sample, either of the above methods may reduce the background at high mass by a factor of $\gtrsim 2$.

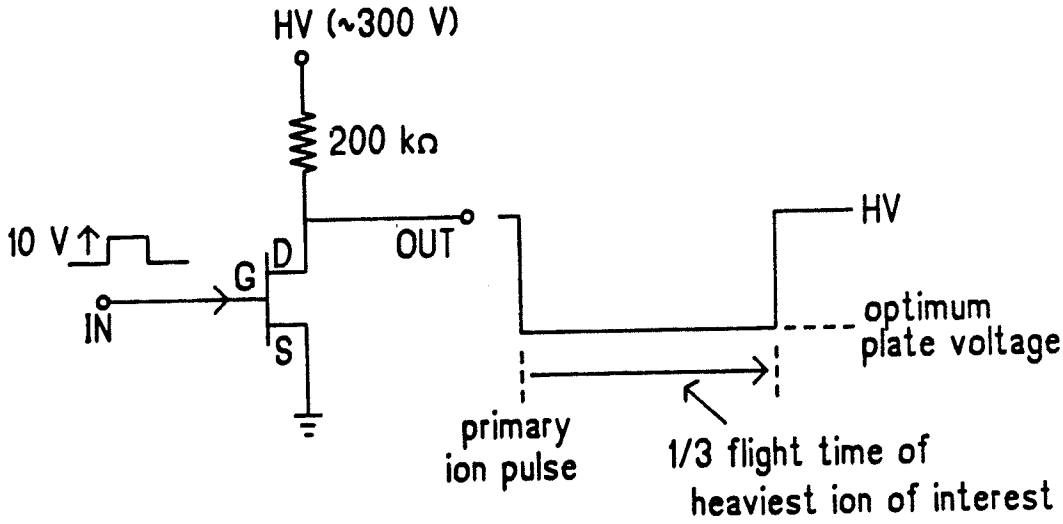

Figure 4.5 Secondary plate pulsing circuit used to reduce random background from ions leaking from the primary ion gun between pulses. For the sample of fig. 4.2, pulsing the plates 13 μs after the primary ion pulse, suppresses background above m/z 300.

4.3 MASS RANGE

A second important advantage of a time-of-flight spectrometer is the high upper mass limit and the wide mass window that are possible without sacrifice in performance. The upper mass limit is determined by the detection efficiency (§2.5.3). Measurement of CsI clusters (without post-acceleration) presented in chapter 6 indicate that this limit is well above m/z 10000. The spectrum is stored in a histogram so the mass window is limited by the channel width and the size of the histogram (§3.3.1). Using the LeCroy TDC and the LSI 11/23, 32000 channels are available with channel width any multiple of 1 ns. With 10 kV secondary ion acceleration, this corresponds to a mass window of 0 to 750 using 1 ns bins or 0 to 12000 with 4 ns bins.

As examples of the largest organic compounds analysed here, fig. 4.6 shows two spectra of fully protected oligonucleotides (30). These were taken using a single stop TAC and the data were histogrammed in a 4000 channel pulse-height analyser (§3.2). The low mass portion of the spectrum was suppressed to reduce the counting rate.

4.4 MASS RESOLUTION

Three causes of peak broadening are identified in chapter 2: the spread in initial axial velocity (§2.3), the duration of the primary ion pulse (§2.4.2), and metastable decay in the field-

Figure 4.6 Examples of time-of-flight spectra of large organic molecules: upper, positive ion spectrum of protected CpCpCpC (with CsI impurity); lower, negative ion spectrum of protected CpCpCpCpC. See ref. 30 for details. Both spectra were taken with a time-to-analogue converter (§3.2) and are displayed in 70 ns bins with a smooth background subtracted. The asterisks in the upper spectrum indicate identified fragment ions with Cs addition.

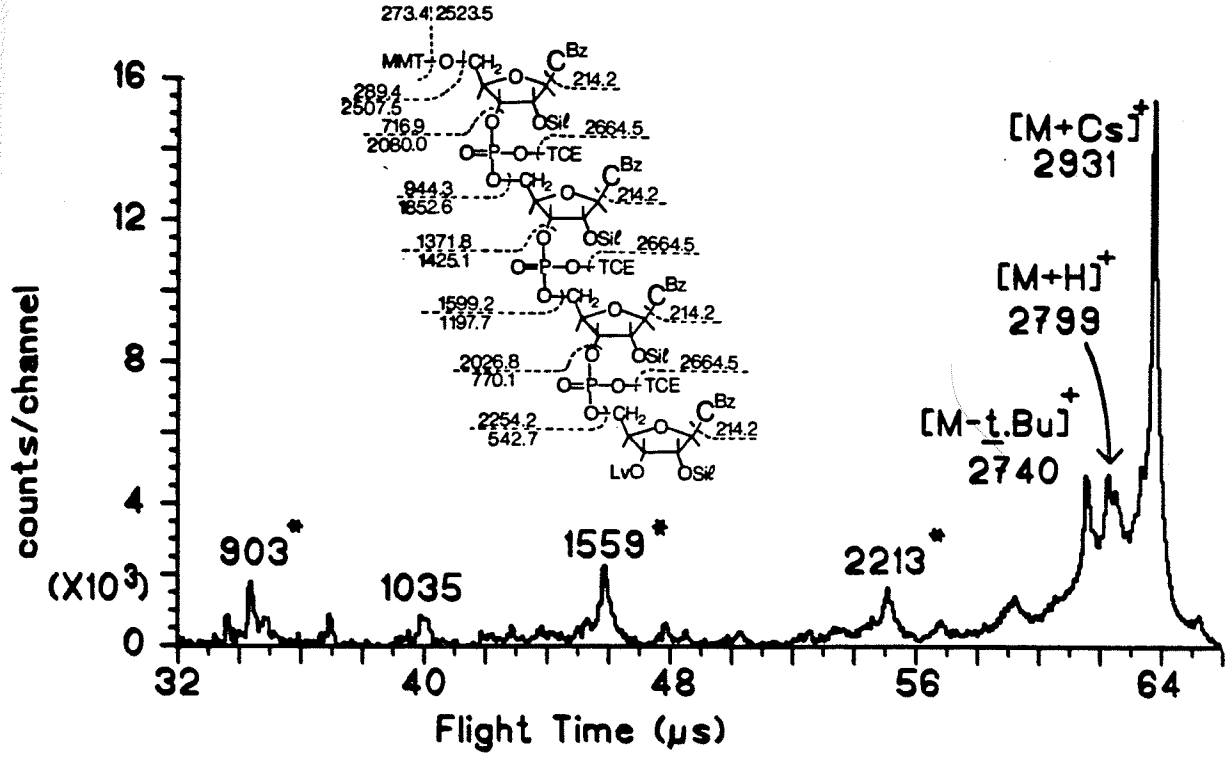
counts/channel
(X10³)
16
12
8
4
0
32
40
48
56
64
Flight Time (μs)
903*
1035
1559*
2213*
[M+Cs]⁺
2931
[M+H]⁺
2799
[M-t.Bu]⁺
2740
273.4 2523.5
MMT
Bz
214.2
289.4
2507.5
716.9
2080.0
OSiℓ
2664.5
O=P-O-TCE
944.3
1852.6
1371.8
1425.1
1599.2
1197.7
2026.8
770.1
2254.2
542.7
LvO
OSiℓ

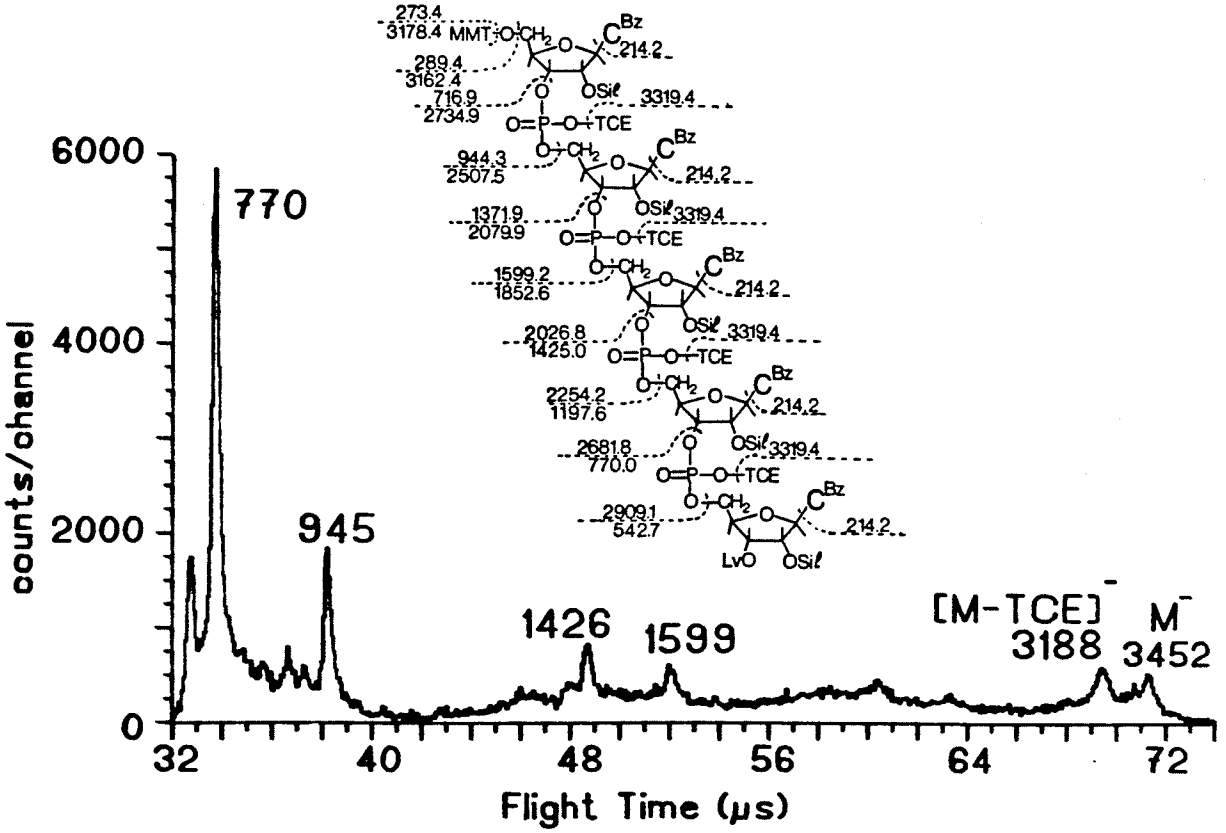
counts/channel
6000
4000
2000
0
32
40
48
56
64
72
Flight Time (μs)
770
945
1426
1599
[M-TCE]⁻
3188
M⁻
3452
273.4
3178.4
MMT
Bz
214.2
289.4
3162.4
716.9
2734.9
OSiℓ
3319.4
O=P-O-TCE
944.3
2507.5
1371.9
2079.9
1599.2
1852.6
2026.8
1425.0
2254.2
1197.6
2681.8
770.0
2909.1
542.7
LvO
OSiℓ

free flight tube (§2.5.4). When a peak is broadened by metastable break-up, this effect is usually dominant and may be treated separately. The other two effects have comparable magnitudes and are treated together.

4.4.1 Mass Resolution for Stable Ions

Since the secondary ion mass m_s is proportional to the square of the flight time t (§2.3), mass resolution is related to time resolution by

$$\frac{\Delta m_s}{m_s} = \frac{2\Delta t}{t}$$

If only the effect of the primary pulse duration is considered, $\Delta t = \Delta t_p$, so

$$\frac{\Delta m_s}{m_s} = \frac{2\Delta t}{t} = \frac{2\Delta t_p}{\ell\sqrt{m_s/2E_s}}$$

where $E_s = (1/2)m_s(\ell/t)^2$ is the secondary ion energy. Thus the mass resolution in this case improves with mass (and the flight path length ℓ) but decreases with the accelerating voltage ($V_s = E_s/q_s$).

Considering only the effect of the initial axial velocity spread Δv_{oz} giving a spread $\Delta \mathcal{E}_z$ in $\mathcal{E}_z = m_s v_{oz}^2$, the mass resolution is

$$\frac{\Delta m_s}{m_s} = \frac{\Delta \mathcal{E}_z}{E_s}$$

Here mass resolution improves with accelerating voltage and is independent of mass and flight path length.

Since the two effects are uncorrelated, they add in quadrature giving a theoretical mass resolution of

$$\frac{\Delta m_s}{m_s} = \sqrt{\frac{\Delta \epsilon_z^2}{E_s^2} + \frac{8E_s}{m_s \ell^2} \Delta t_p^2} \qquad (4.1)$$

The best resolution is obtained when $d(\Delta m/m)/dE_s = 0$ or

$$E_s = \left(\frac{m\ell^2 \Delta \epsilon_z^2}{4\Delta t_p^2}\right)^{1/3}$$

The optimum accelerating voltage therefore increases with mass. Taking $\Delta \epsilon_z = 1.2$ eV (measured for Cs^+ - fig. 2.6) and a typical pulse duration of $\Delta t_p \approx 3$ ns, this gives an optimum resolution at m/z 100 of ~1/2300 for $V_s \approx 5$ kV. The best resolution at m/z 1000 is calculated as ≈ 1/5000 with $V_s \approx 10$ kV.

The measured resolution (FWHM) of $(CsBr)_3Br^-$ at m/z 718, with $V_s = -5$ kV is ≈ 1/3200 (fig. 4.7), very close to the value

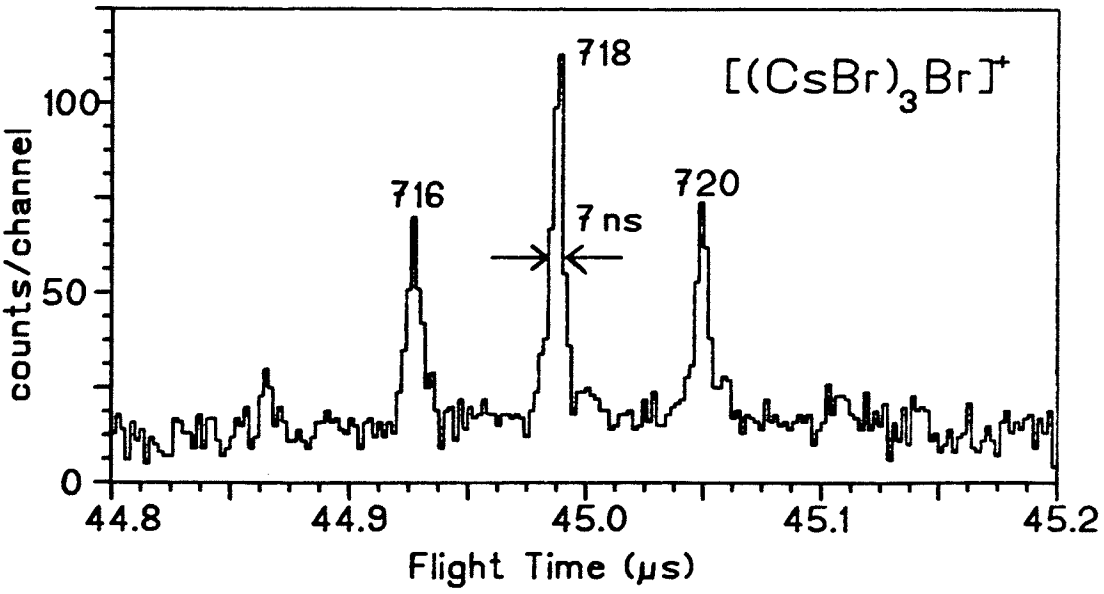

Figure 4.7 Negative ion time-of-flight spectrum of CsBr near the third cluster. Primary ion energy 28 keV, secondary ion accelerating voltage 5 kV. $\Delta t(FWHM)/t \approx 1/6400$ so $\Delta m(FWHM)/m \approx 1/3200$. Predicted resolution from the primary ion pulse duration and secondary ion velocity spread of Cs^+, under these conditions is 1/3600.

predicted by eq'n 4.1 (1/3600) using the above values for $\Delta\mathcal{E}_z$ and Δt_p. Better resolution is expected for higher accelerating voltage and higher mass according to eq'n 4.1 but this was not realized; presumably other instrumental factors such as the non-uniformity of the accelerating field become important.

4.4.2 Mass Resolution for Metastable Ions

For most molecules with $m/z \gtrsim 200$, the mass resolution is much poorer than that demonstrated in the previous section because of metastable decomposition in the field-free flight path. While $\lesssim 50$ meV are released in a typical break-up (55), the effective energy spread ΔE in the fragments is amplified by the motion of the centre-of-mass (55,62):

$$\Delta E = \sqrt{E_s T}\ \frac{4\sqrt{m_1 m_2}}{m_s}$$

Here T is the translational energy released in the fragmentation, m_1 and m_2 are the masses of the fragments, and m_s is the mass of the parent. For a 10 keV ion that breaks up into two equal fragments with an energy release of 50 meV, the effective energy spread of one of the fragments is 45 eV. Peak broadening is greatest if the ion decays near the target. Then the energy of fragment 1, $E_1 = (m_1/m_s)E_s$, is approximately related to its flight time t by $E_1 = (1/2)m_1(\ell/t)^2$. The time spread Δt is then related to the energy spread ΔE by

$$\frac{\Delta t}{t} = \frac{\Delta E}{2E_1}$$

so the mass resolution is

$$\frac{\Delta m_s}{m_s} = \frac{2\Delta t}{\Delta t} = \frac{\Delta E}{E_1} = 4\sqrt{\frac{T\, m_2}{E_s\, m_1}}$$

where m_1 is the detected fragment. If the efficiency for detection of m_1 and m_2 is equal, m_1/m_2 will average to one so

$$\frac{\Delta m_s}{m_s} = 4\sqrt{\frac{T}{E_s}} \qquad (4.2)$$

For $T = 50$ meV and $E_s = 10$ keV, this gives mass resolution of $\approx 1/100$. Eq'n 4.2 represents the resolution for the worst case. In practice the detector efficiency (§2.5.3) and transmission is better for heavier ions (the lighter fragment is more likely to be deflected out of the path of the counter by the disintegration kinetics) so m_1/m_2 is usually greater than one. Also decomposition farther from the target results in a smaller time spread and $T = 50$ meV overestimates the energy released in break-up for most compounds (50). The spectra shown in figs. 4.1, 4.2, and 4.5 have mass resolution near the molecular ion between 1/100 and 1/400.

If the bin width is sufficiently narrow, sharp peaks resulting from ions that remain intact may be observed on top of the broad metastable peaks. This is clearly seen for met-enkephalin: fig. 4.8 compares the molecular ion region of the TAC-ADC spectrum shown in fig. 4.1 with a more recent spectrum taken with the TDC. Such sharp components are observable even when a large fraction of the ions decay in the flight tube. An example is given in the spectrum of substance P shown in fig. 4.9 which also serves to demonstrate the new data acquisition system. The complete spectrum was taken in a single run using 2 ns chan-

nels. The bottom trace shows the molecular ion region expanded; the isotopic pattern of the C atoms is clearly resolved. Depending on how much of the broad component results from metastable ions, mass resolution (FWHM) is near 1/3000.

While the metastable ions enhance sensitivity because they contribute to the total peak integral, it is clearly desirable to suppress them if accurate mass measurement is required - to distinguish between protonated and radical ions for example. This has been done by Chait et al (34,54-56) using retarding grids to reflect charged daughter ions. The same could be done here but since the transmission of neutrals is comparable to that of ions, only a suppression ~1/2 of the metastable component could be expected.

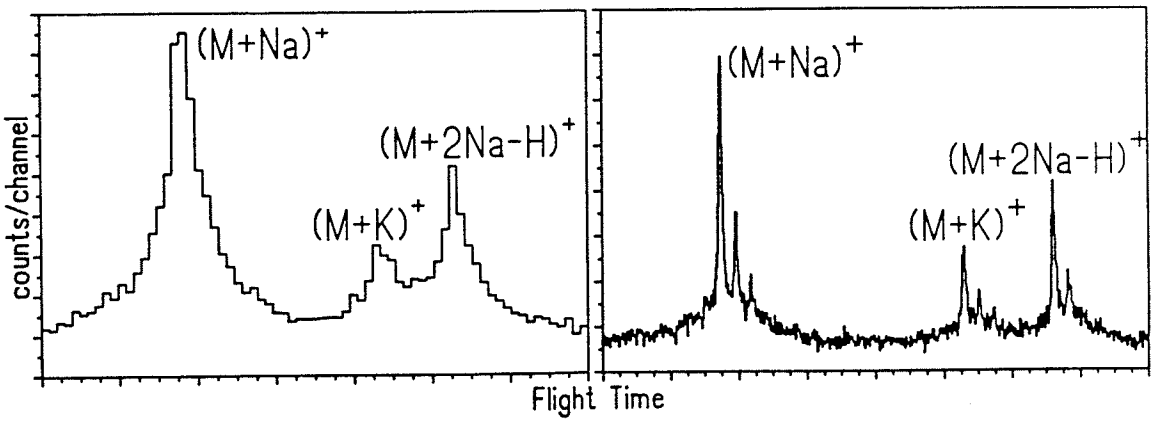

Figure 4.8 Spectrum of methionine enkephalin near the molecular ion taken before (left - expansion of fig. 4.1) and after (right) installation of the TDC.

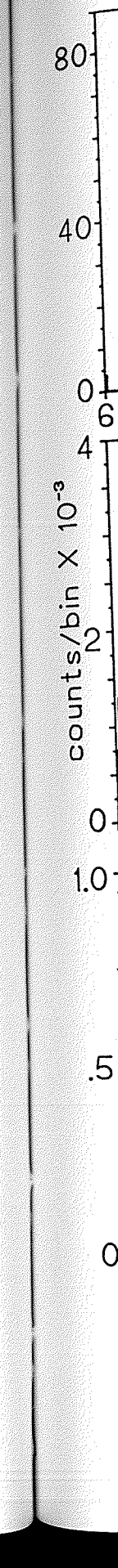

Figure 4.9 Positive ion spectrum of substance P (most abundant isotope, m/z 1346.7) acquired in 90 min. with a TDC (§3.3) using 2 ns channels. The spectrum was calibrated with the Na, m/z 70 and m/z 120 peaks. The middle trace is displayed in 8 ns bins; the top and bottom in 2 ns bins. The middle and bottom traces have a smooth background subtracted. In the bottom trace satellite peaks from ^{13}C are observed in addition to the broad metastable peak. The measured mass at these peaks is very close to the calculated isotopic mass. Similar multiplets may be observed for many of the fragment ion peaks if displayed in narrow bins; the labelled masses represent the most intense peak in the multiplet.

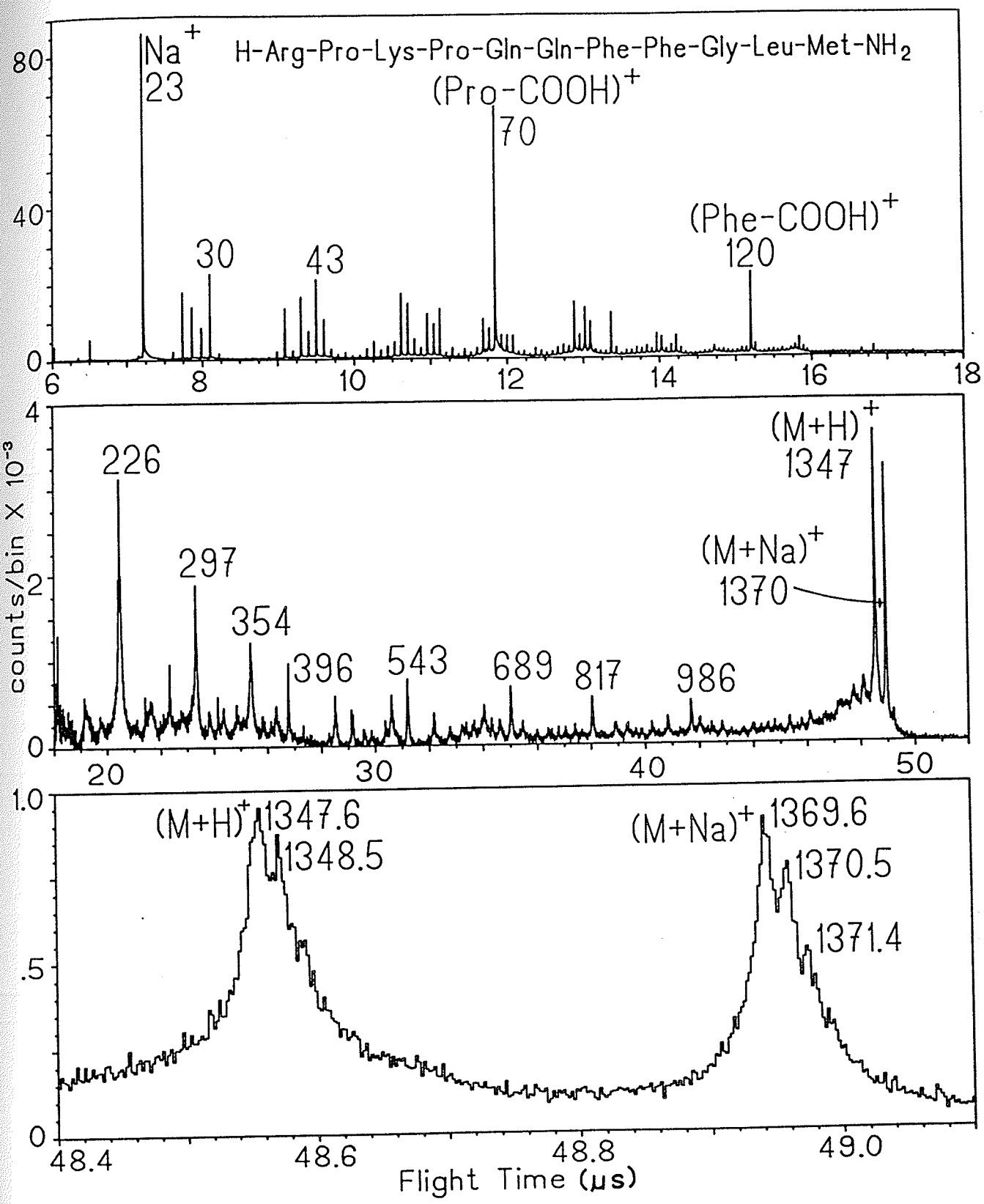
Na+
23
H-Arg-Pro-Lys-Pro-Gln-Gln-Phe-Phe-Gly-Leu-Met-NH2
(Pro-COOH)+
70
(Phe-COOH)+
120
30
43
80
40
0
6
8
10
12
14
16
18
counts/bin X 10-3
4
2
0
226
297
354
396
543
689
817
986
(M+H)+
1347
(M+Na)+
1370
20
30
40
50
1.0
.5
0
(M+H)+ 1347.6
1348.5
(M+Na)+ 1369.6
1370.5
1371.4
48.4
48.6
48.8
49.0
Flight Time (μs)

CHAPTER 5

PRIMARY ION ENERGY LOSS AND SECONDARY ION DESORPTION

5.1 INTRODUCTION

Particle induced desorption has made a valuable contribution to mass spectrometry because of its ability to desorb and ionize many large, fragile molecules intact. However, the desorption mechanism is still only poorly understood. A better understanding may be gained by studying the influence of primary ion parameters on the mass spectrum.

Stopping power (dE/dx), the energy loss per travelled path length, is an obvious parameter to consider when measuring effects of the primary ion characteristics on secondary ion yields since it depends on both mass and energy. The stopping power has two components, "nuclear stopping" (elastic collisions with the target atoms), and "electronic stopping" (energy transfer to the atomic electrons).

Fig. 5.1 illustrates the dependence of the stopping power on energy (63). The stopping powers for ^{35}Cl ions with 1 keV/u (~ low energy ion bombardment) and 1 MeV/u (~ fission fragment bombardment) on ^{27}Al are indicated in the figure. Clearly the dominant mode of energy loss is different in the two cases.

The similarity of mass spectra obtained with 2 keV Ar^+ ions (16) to those obtained with fission fragments was therefore unexpected. Direct comparison between keV ion bombardment and fission fragment bombardment was difficult, however, because the laboratories that used the different ionization techniques also used different methods of sample preparation and different types of mass spectrometer. Apart from the Manitoba mass spectrometer, this has remained true until very recently (23,24). Moreover the comparisons that had been made used relatively simple compounds with $m/z \lesssim 400$. Here a direct comparison was made of mass spectra obtained with the two techniques; the same target was used in

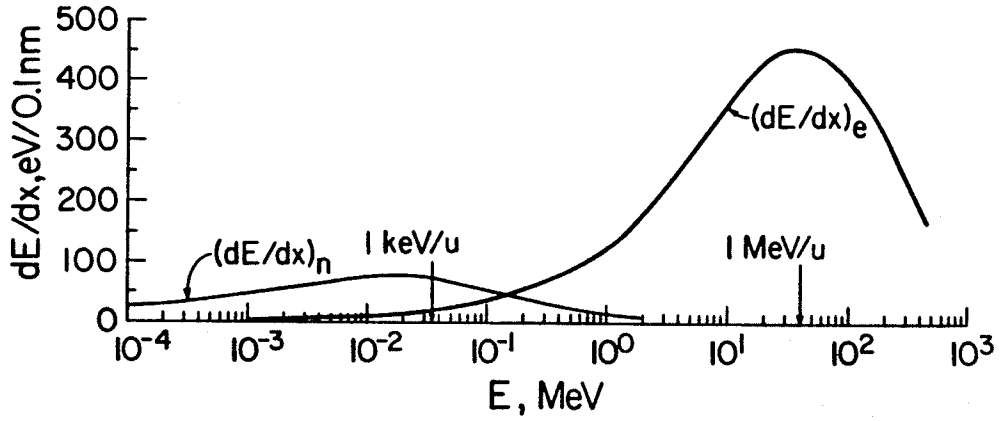

Figure 5.1 Energy deposition density (dE/dx) for ^{35}Cl impinging on ^{27}Al. The (dE/dx) curve for nuclear excitation is designated by $(dE/dx)_n$. The electronic excitation curve is designated as $(dE/dx)_e$. From ref. 63.

both measurements and both were made using time-of-flight.

Since discovery of fission fragment induced desorption (10), the effects of primary ion mass and energy have been studied using particle accelerators (13,14). The observations indicate that the desorption yields follow the electronic stopping curves (13,64,65). Since the same ionization process appears to be responsible at high and low energies (from the similarity in the mass spectra) these results seemed to indicate that molecular desorption at low energy is related to the low energy tail of the electronic energy loss curves (see fig. 5.1).

To determine which energy loss process is responsible for desorption at low energies, the yields of the amino acid alanine were measured as a function of energy for several alkali ions. These results were then compared to the nuclear and electronic stopping curves.

5.2 COMPARISON OF MASS SPECTRA FROM HIGH AND LOW ENERGY PRIMARY IONS

5.2.1 Experimental

Mass spectra obtained using ^{252}Cf fission fragments at Rockefeller University were compared with those taken using keV alkali ions at Manitoba (26). Measurements were made on the following compounds: alanine, arginine, sucrose, tetrabutylammonium iodide, adenosine 5′-monophosphate, adenylyl-(3′-5′)-cytidine (ApC), and vitamin B_{12} (cyanocobalamin). For all these compounds both positive and negative ion mass spectra were

obtained.

For these measurements, 2-20 keV K^+ or Cs^+ ions were used in the Manitoba instrument. Secondary ions were accelerated to between 2.5 and 5 keV except for positive ions from vitamin B_{12} which were accelerated to 10 keV. Time-of-flight was measured using time-to-amplitude conversion as described in §3.2 and analysis was performed using the applications program provided with the pulse-height analyser (see fig. 3.1).

The fission fragment instrument at Rockefeller is described in detail in ref. 55. While the principle of mass measurement (time-of-flight) is the same in the two instruments there are some differences in detail. The fission fragments bombard the sample foil from the back side and thus pass through the foil before reaching the sample. They are effective on a 12 mm diameter area compared to ~1 mm in the Manitoba instrument. The flight tube at Rockefeller is 3 m (compared to 1.6 m) and employs an electrostatic particle guide (66) to enhance the transport efficiency of ions to the detector.

Ions are accelerated in the fission fragment device with two grids spaced 4.5 mm from the sample foil and an equal distance apart. Secondary ion energy is typically 6.5 keV except for positive ions for vitamin B_{12} where 10 kV was used as in the low energy instrument. The differences in configurations and voltages cause the sample ions to be extracted into the field free flight tube two or three times faster in the ion bombardment mass spectrometer than in the fission fragment mass spectrometer. The fission fragment instrument uses a multistop time-to-digital converter (67) with a very low deadtime ($>$ 10 ns). The flight

times of up to 15 secondary ions per primary fragment may be measured with this device, and thus it does not give rise to spectral distortion of the kind mentioned in §3.2.1. when the single stop TAC is used. Considerable care was exercised to ensure that the primary pulsed beam was kept to a low enough intensity to ensure minimal spectral distortion.

The compounds were dissolved in mixtures of methanol and water and electrosprayed onto aluminized polyester (6.4 μm thick) to a thickness of ~ 10 $\mu g/cm^2$. The compounds were obtained from Sigma Chemical Co. except for sucrose (Fisher Scientific Co.) and tetrabutylammonium iodide (Aldrich Chemical Co.) and used without purification.

The samples were first prepared and analysed at Manitoba with low energy ion bombardment. The foils were then packed in shipping containers with the sample side free of contact, and sent by post to Rockefeller where spectra were taken with the fission fragment mass spectrometer. The average time interval between the two analyses of a sample was about 1 week.

5.2.2 Data Analysis

For determination of the background, spectra of bare sample foil were taken with both machines. Considerable backgrounds were observed in the low mass region ($m/z < 150$) for both instruments. In the positive fission fragment spectrum large ion intensities were observed at m/z 1 (H^+), m/z 23 (Na^+), m/z 39 (K^+), and m/z 63 together with numerous peaks of smaller intensity. The low-energy ion bombardment spectrum was rather different, with large peaks at m/z 23, 27, 29, 41, 43, 57, and 149. The most

intense peaks observed from the bare foil in the ion bombardment negative spectrum were m/z 1 (H^-), m/z 16 (O^-), and m/z 17 (OH^-). The ions at m/z 16 and 17 are present in relatively low intensity in the fission fragment negative spectrum, and the most intense ions are observed at m/z 1 (H^-) and m/z 25 (C_2H^-). In addition, numerous differences in ions of smaller intensity are observed. The cause or significance of these differences is not understood.

These backgrounds were subtracted from the sample spectra making use of the arbitrary criterion that sample peaks must have approximately twice the intensity of the background peak at the same m/z value to be retained in the net spectrum. The ubiquitous ions H^+, Na^+, H^-, O^-, OH^-, and C_2H^- were generally omitted from the spectral comparisons because of their uncertain origin.

All the fission fragment spectra with the exception of those of ApC and vitamin B_{12} were recorded in channels 3.125 ns wide, and the plotted intensities are the result of 5 channel sums about the peak centroids. Because of the greater length of the spectrum, ApC data were recorded at 5 ns/channel, and the intensities are the result of 3 channel sums about the peaks. The ion bombardment mass spectra were recorded at 9.2 ns/channel with the exception of that for vitamin B_{12}, which was recorded at 13 ns/channel. The plotted intensities for alanine, arginine, and sucrose were obtained from 5 channel sums, while ion intensities for the other compounds were simply obtained from the peak heights. The peak shapes for different ion species from a particular compound differ markedly, but in the same way for both methods of ionization. The method for deriving the intensities outlined above puts emphasis on peak heights, thus tending to

underestimate the total intensity under broad peaks. However, since very similar broadening effects are observed with both modes of ionization (§4.4.2), the comparisons are meaningful.

5.2.3 Results

Positive and negative mass spectra were determined with both modes of ionization for all eight compounds. Histogram spectra of 6 of the compounds are shown in figs. 5.2 - 5.9. Each pair of spectra are normalized to give equal intensities at an appropriate molecular parent ion (usually $(M+1)^{\pm}$). In all cases the spectra obtained with the two methods are highly similar. The spectra of ApC (fig. 5.6) and tetrabutylammonium iodide (fig. 5.7) are representative of the best agreement obtained between the two ionization methods, while the positive sucrose spectra (fig. 5.4a) represents the poorest agreement. The

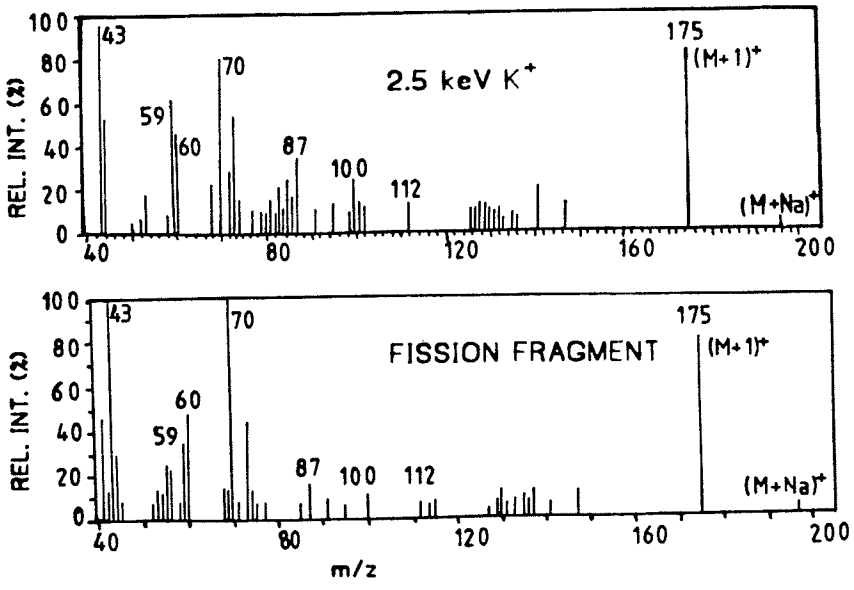

Figure 5.2 Arginine positive ion spectra: upper, 2.5 keV K^+ ion bombardment; lower, ^{252}Cf fission fragment bombardment.

agreement for the other spectra generally lie between these.

The molecular ion is formed in the same way for most of the samples (e.g. H or Na attachment). The most significant exception to this is sucrose where the low energy ion bombardment spectrum

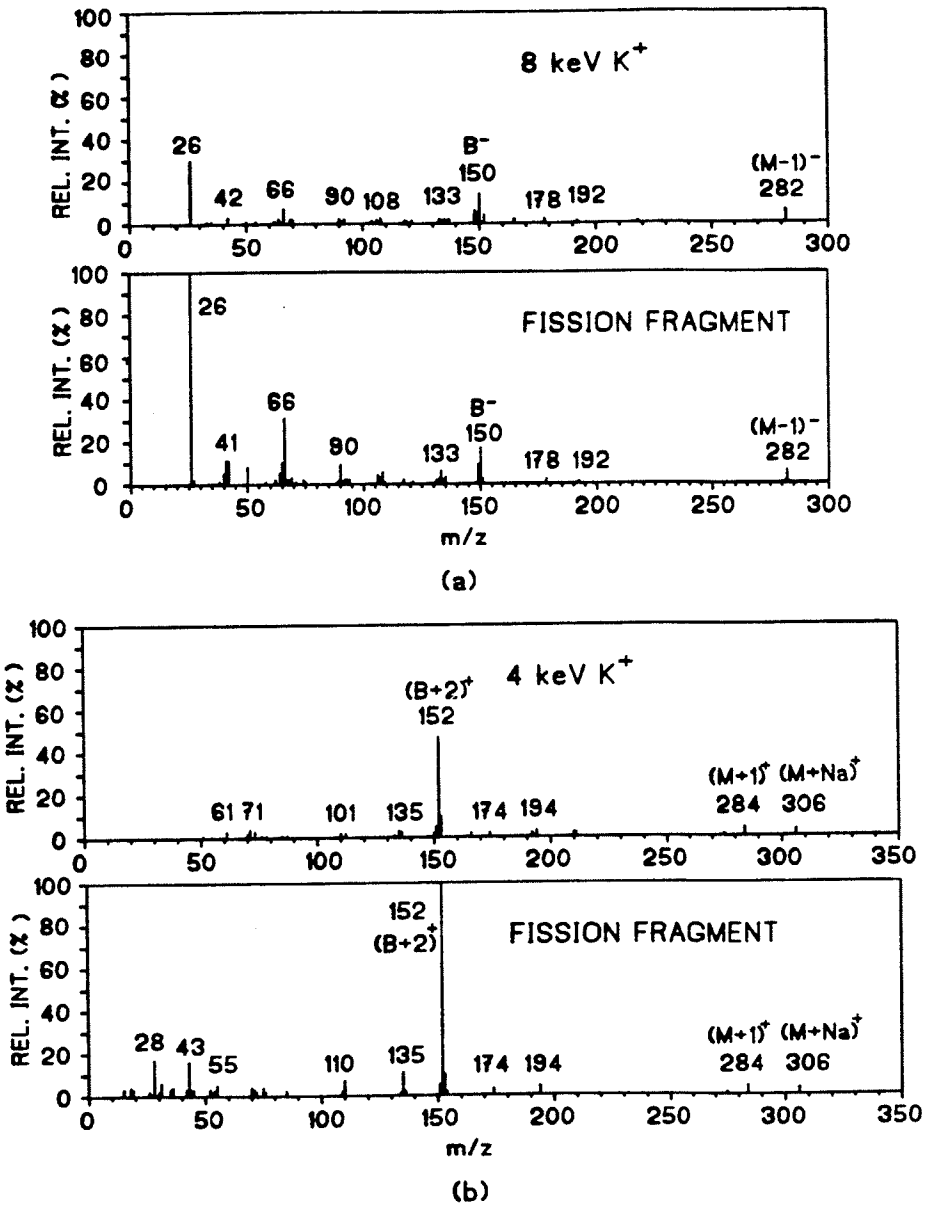

Figure 5.3 Guanosine (a) positive ion spectra: upper, 4 keV K^+ ion bombardment, lower, ^{252}Cf fission fragment bombardment, (b) negative ion spectra: upper, 8 keV K^+ ion bombardment, lower, ^{252}Cf fission fragment bombardment.

(fig. 5.4a) shows an $(M+K)^+$ peak in addition to the $(M+Na)^+$. This was not observed in the fission fragment spectrum. It is possible that a small part of the target was doped by the primary K^+ beam which was used for this measurement. Since the fission

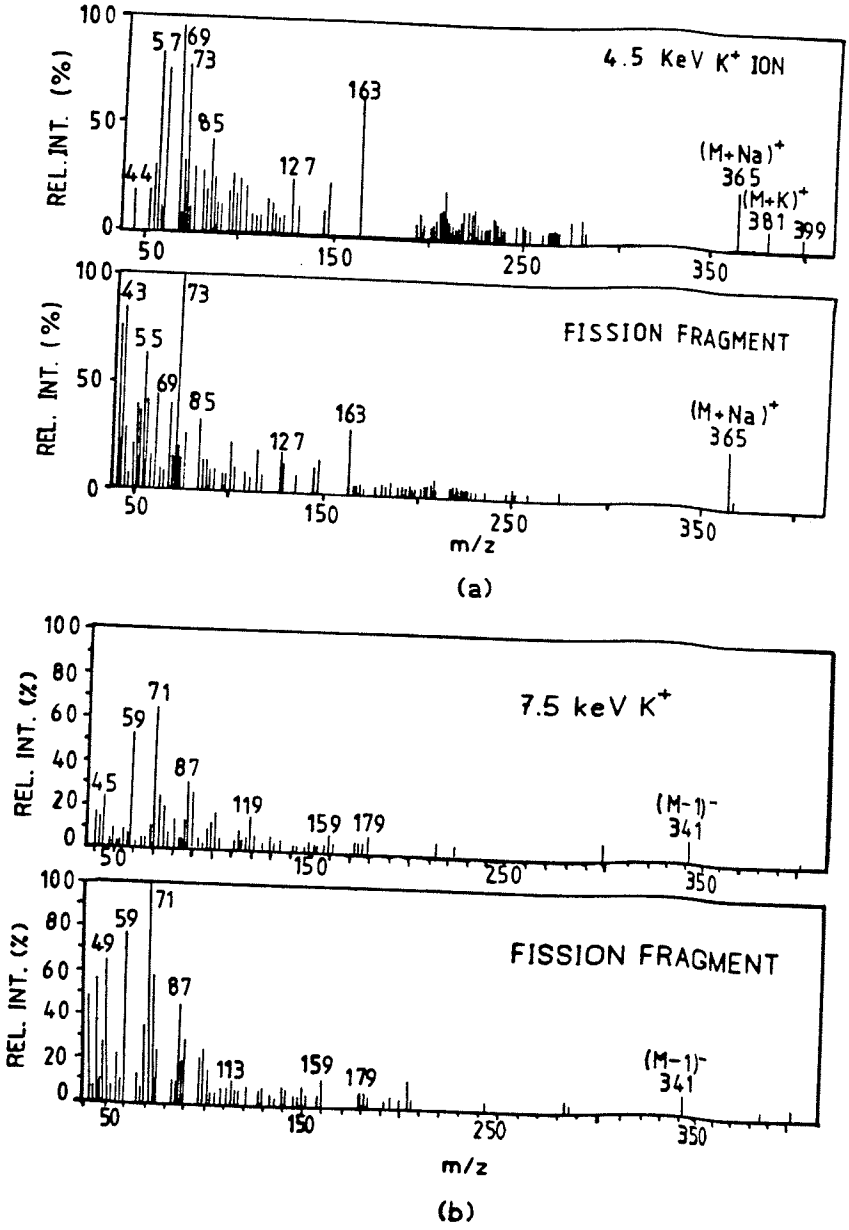

Figure 5.4 Sucrose a) positive ion spectra: upper, 4.5 keV K^+ ion bombardment; lower, ^{252}Cf fission fragment bombardment, b) negative ion spectra: upper, 7.5 keV K^+; lower, ^{252}Cf fission fragment bombardment.

fragment method averages over a much larger area, this would probably not be detected.

In general, the relative intensities of the identified fragments agree to within a factor of 2. Some differences in the

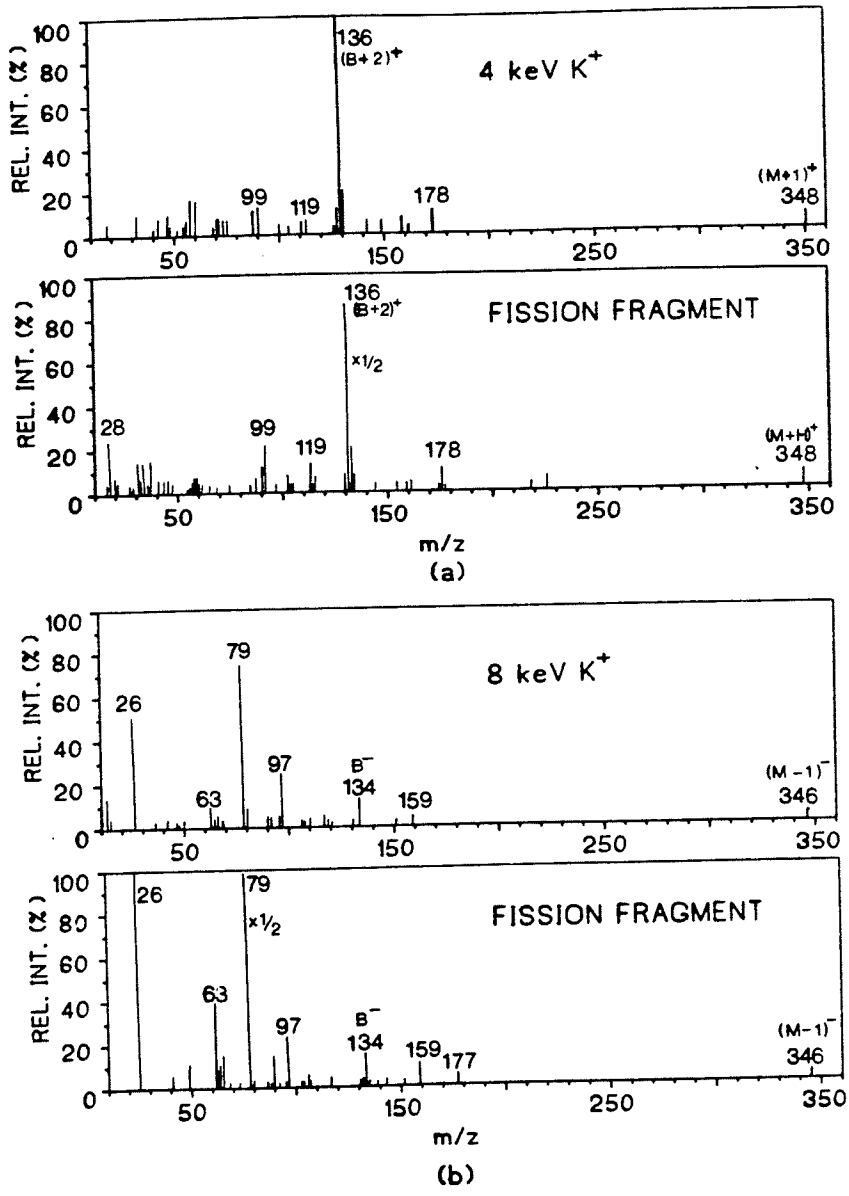

Figure 5.5 5′-AMP (a) positive ion spectra: upper, 4 keV K^+ ion bombardment; lower, ^{252}Cf fission fragment bombardment, (b) negative ion spectra: upper, 8 keV K^+ ion bombardment; lower, ^{252}Cf fission fragment bombardment.

spectra are observed but these do not appear to result from sample ions. For example, in the positive sucrose spectra (fig. 5.4a), the pattern of small peaks between m/z 200 and 300, which is quite different in the two spectra, seems to result from

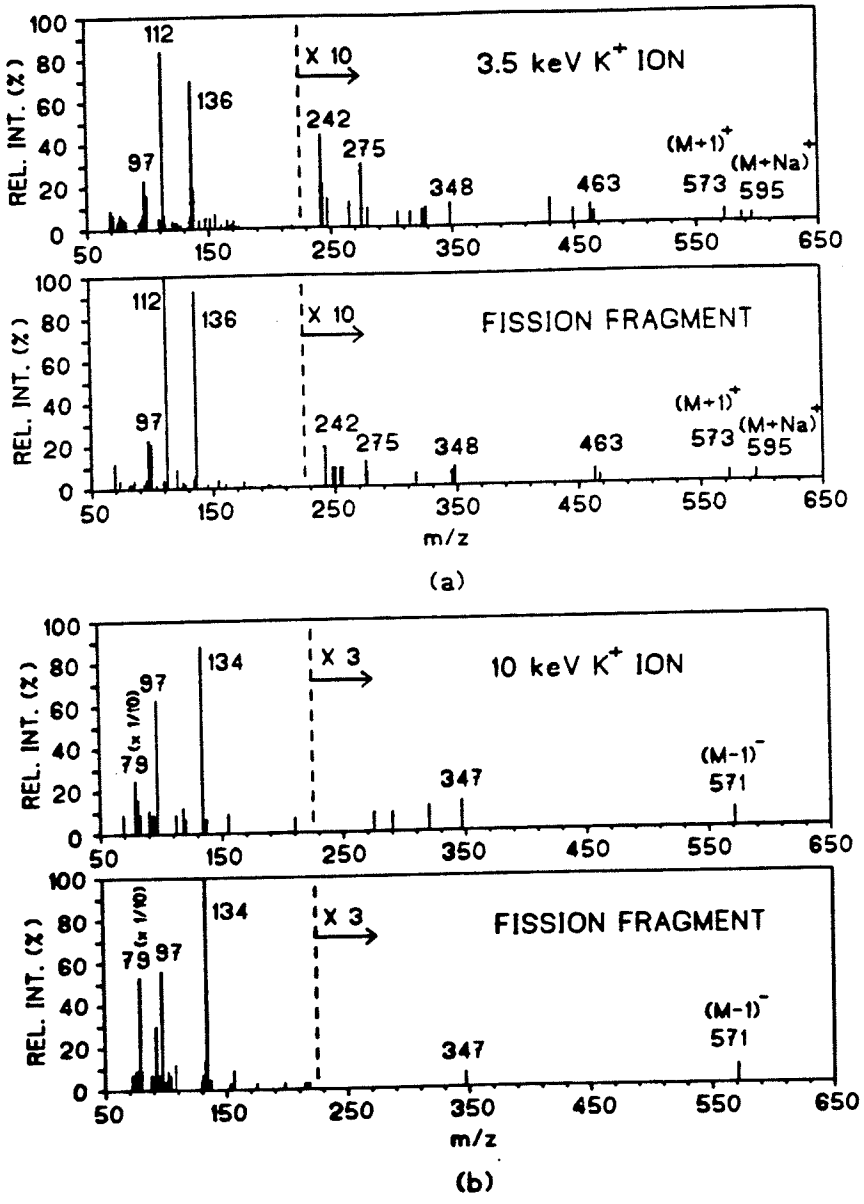

Figure 5.6 Adenylyl-(3′→5′)-cytidine (ApC) (a) positive ion spectra: upper, 3.5 keV K^+ ion bombardment; lower, ^{252}Cf fission fragment bombardment, (b) negative ion spectra: upper, 10 keV K^+ ion bombardment; lower, ^{252}Cf fission fragment bombardment.

impurities since it did not occur for independently prepared samples measured with the fission fragment apparatus. In addition, many of the peaks for which substantial differences were observed correspond to ions having large mass defects (measured at Rockefeller) and are thus inorganic in origin.

The largest molecule for which a direct comparison was made was vitamin B_{12}. The raw time-of-flight data for this sample are shown in fig. 5.8. Even for a molecule as complex as vitamin B_{12} the raw data show remarkable similarities in detail, especially above mass 150. In the positive spectrum, a peak is observed at m/z 1330 with fission fragments and at m/z 1329 with low energy ions, which probably corresponds to the loss of the cyanide ligand attached to the central cobalt atom. There is also some discrepancy in the mass assignment of the negative ion peaks at high mass, but these are probably not significant; the error in the ^{252}Cf measurements was $\lesssim$ u, but the estimated uncertainty in

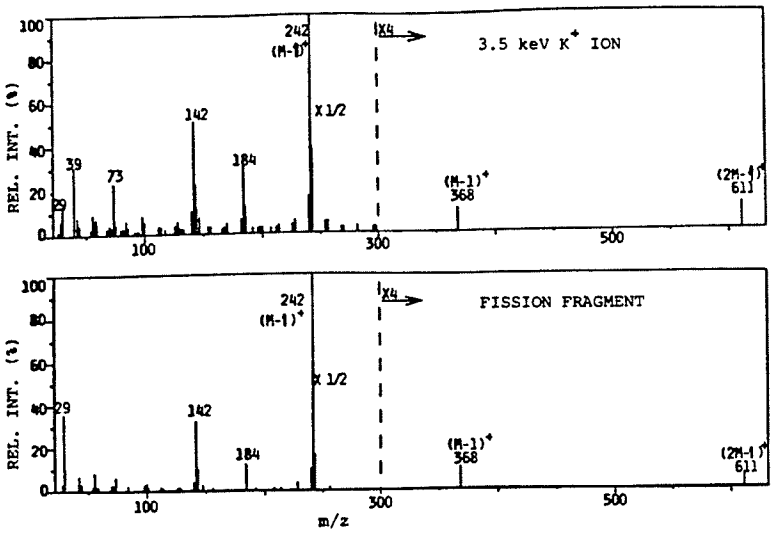

Figure 5.7 Tetrabutylammonium iodide positive ion spectra: upper, 3.5-deV K^+ ion bombardment; lower, ^{252}Cf fission fragment bombardment.

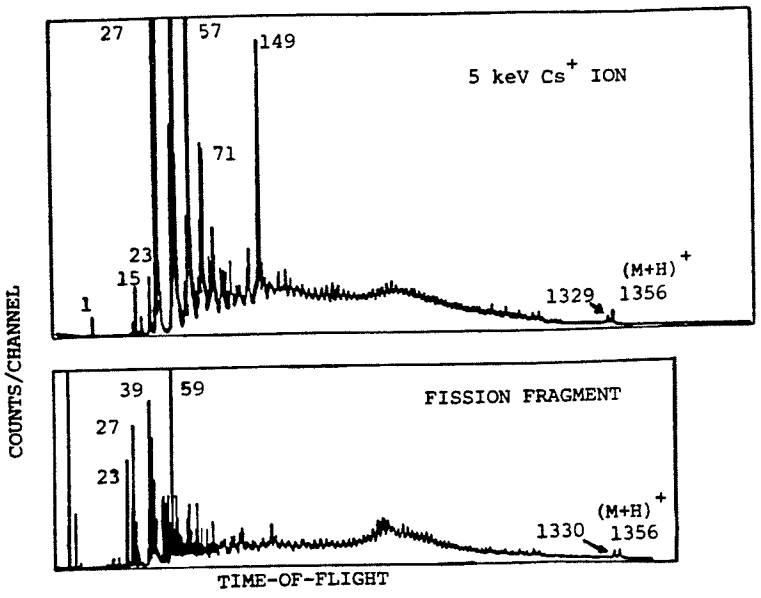

(a)

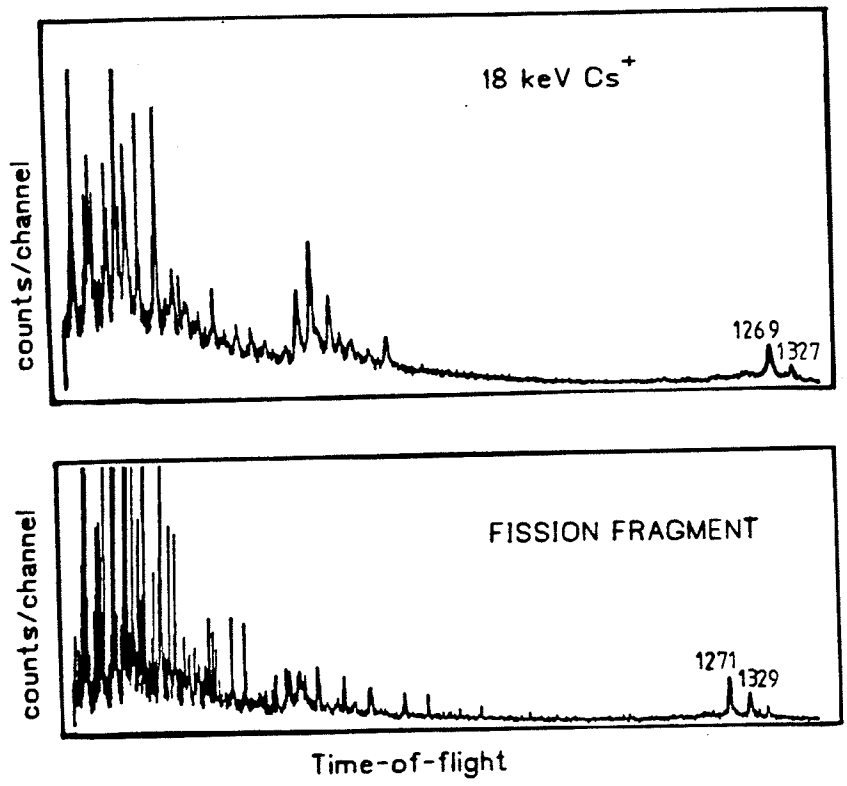

(b)

Figure 5.8 Direct time-of-flight spectra for vitamin B_{12}. (a) Positive ion spectra: upper, 5.0 keV Cs^+ ion bombardment; lower, ^{252}Cf fission fragment bombardment. (b) negative ion spectra: upper,18 keV Cs^+ ion bombardment; lower ^{252}Cf fission fragment bombardment.

the low energy measurements (where analogue circuits with inferior stability and linearity were used - §3.2) was ~2 u. Some differences do exist, as for instance the observation of a large peak at m/z 149 in the ion bombardment spectrum and its relative absence in the fission fragment spectrum. However, an impurity ion is consistently observed in the ion bombardment spectra at m/z = 149 and is only seen with weak intensity in the fission fragment spectra. This peak is probably associated with phthalate impurities at the surface. Since the fission fragments pass through the target from behind and have much higher energy, they sample a larger volume and may therefore be less sensitive to surface impurities than low energy ions striking the front of the target. Further discrepancies are to be seen in the low mass region. However, several of these may also be associated with background ions.

Although the vitamin B_{12} spectra are the only ones that show ions below m/z ~ 15, the differences observed here for the hydrogen ions are typical: If H^+ is observed in the low energy spectra its relative intensity is much less than in the corresponding fission fragment spectrum where it is usually the base peak. The H_2^+ and H_3^+ ions observed in all fission fragment spectra have not been observed in any low energy spectra.

A less direct comparison between the two methods may be made at higher mass by examining the mass spectra of fully protected oligonucleotides. McNeal et al (68,69) published a detailed study of these compounds using ^{252}Cf fission fragments, and recently

some of them have been analysed in the Manitoba instrument (29,30) with very similar results. An example is given in fig. 5.9. The ^{252}Cf spectrum has better statistics and a smooth background subtracted but otherwise is very similar to that obtained with 10 keV Cs^+ ions. Thus for this type of molecule, it appears that the close similarity extends to at least m/z ~ 2000; protected oligonucleotides up to m/z ~ 3450 have been analysed with keV Cs^+ ions (30) but the compounds were not identical to those studied with fission fragments.

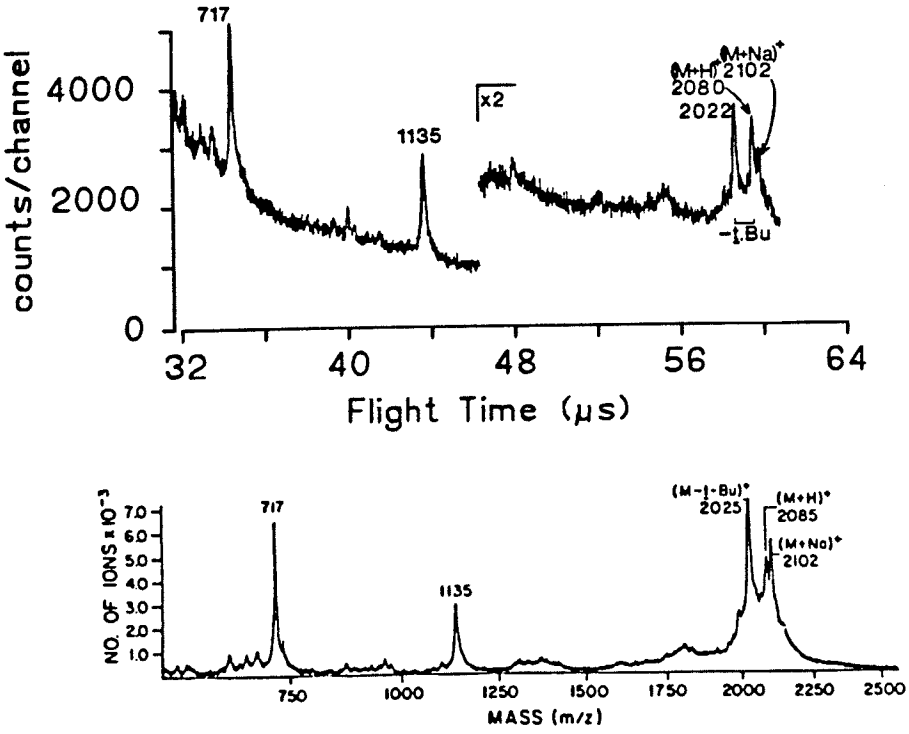

Figure 5.9 Positive mass spectra of C_pA_pU: upper, 10 keV Cs^+ ion bombardment; lower (taken from ref. 68), ^{252}Cf fission fragment bombardment. See ref. 29 or 68 for details.

5.3 SECONDARY ION YIELDS

Pronounced variations in the yield and spectra of secondary ions with changes in primary ion species and energy have been observed. The point is illustrated in fig. 5.10 which compares the positive secondary ion spectrum excited by 1 keV and 14 keV Cs^+ ions. When the primary ion energy increases from 1 keV to 14 keV, the yield of the molecular ions increases by more than an order of magnitude, their ratio to the fragment ions increases, and cluster ions $(2M+H)^+$ become apparent. Secondary ions from alanine produced by primary Cs^+, K^+, N^+ and Li^+ ions at energies up to 16 keV were measured (70).

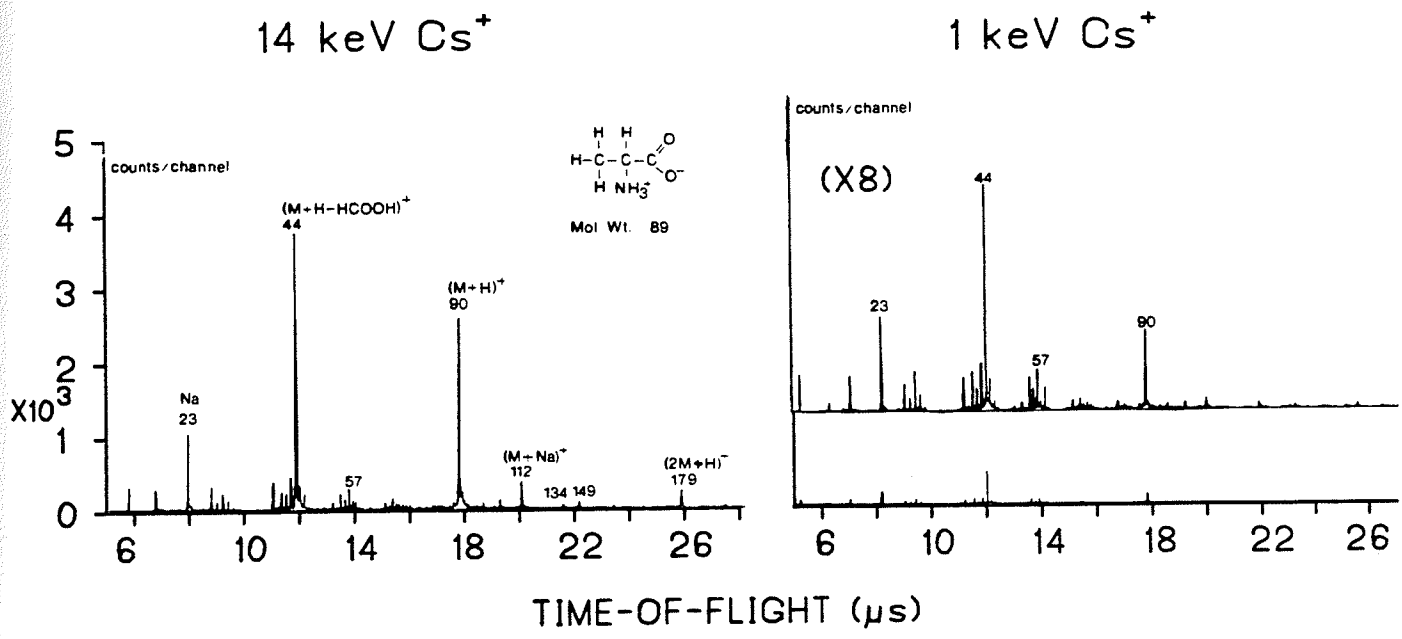

Figure 5.10 Positive ion spectra for alanine with 14 keV Cs^+ (left) and 1 keV Cs^+ (right) primary ions. The scale in the lower right spectrum corresponds to that in the left one. The upper right spectrum is magnified 8 times.

5.3.1 Energy Loss Calculations

Calculations of electronic and nuclear stopping power for alkali metals incident on alanine were made using the Lindhard theory (71) as modified by Wilson, Haggmark and Biersack (72). The results are shown in fig. 5.11.

For low velocities ($v < v_o Z_1^{2/3}$; v_o is the Bohr velocity and

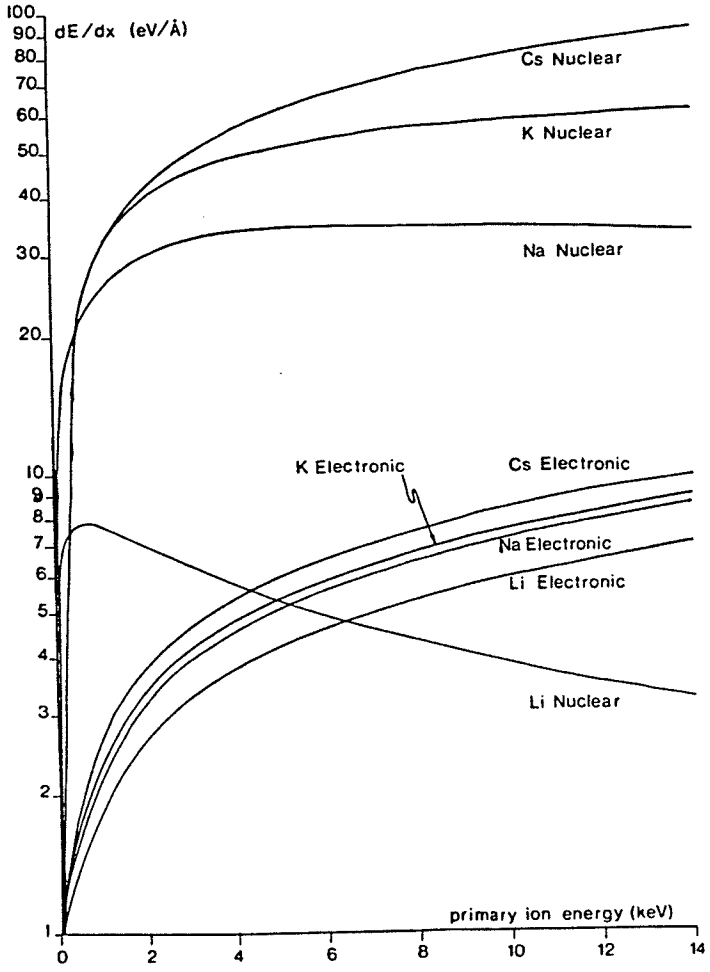

Figure 5.11 Nuclear and electronic energy losses at the surface of an alanine target as a function of primary ion energy for Li^+, Na^+, K^+ and Cs^+. Nuclear stopping curves were calculated using the "average" parameters quoted in ref. 72.

Z_1 the atomic number of the projectile), the electronic cross section S_e is nearly proportional to the projectile velocity (73); this may shown for an atom moving through an electron gas of constant density. The dependence on the projectile and target atomic numbers was determined assuming a Thomas-Fermi model of the atom*:

$$S_e = \xi_e 8\pi e 2a_o \frac{Z_1 Z_2}{Z} \frac{v}{v_o}$$

where a_o is the Bohr radius, $\xi_e \approx Z_1^{1/6}$ and $Z^{2/3} = Z_1^{2/3} + Z_2^{2/3}$. Stopping power is then given by $(dE/dx)_e = NS_e$ where N is the volume density of target atoms.

Nuclear stopping is given by

$$(dE/dx)_n = N \int_0^{T_m} T\, \sigma(T)\, dT \qquad (5.1)$$

where T is the energy transferred to the target atoms and $\sigma(T)$ is the differential cross section for energy transfer. In the Lindhard theory, the cross-section is calculated assuming a potential of the form

$$V(r) = \frac{Z_1 Z_2 e^2}{r} \phi_o(r/a)$$

where ϕ_o (the Fermi function) is a screening function based on the Thomas-Fermi atom; $a = 0.8853 a_o / Z^{1/3}$ is the screening length. The stopping power is then determined by numerical integration of eq'n 5.1. Wilson et al obtained more accurate results with the screening function

$$\phi(r) = \sum C_i e^{-b_i r/a}$$

* The field is assumed to vary slowly over the dimensions comparable to the wavelength of an electron. The model predicts the radius of an atom decreases as $Z^{-1/3}$.

where C_i, b_i were calculated using the free-electron method (74) for several atom pairs over a range of atomic numbers and masses. The results for six neutral atom interactions were averaged to give a representative set of parameters. They found simple analytical expressions to present their results; the reduced stopping power $S_n(\epsilon)$ is given by

$$S_n(\epsilon) = \frac{A\ln(B\epsilon)}{B\epsilon - (B\epsilon)^{-C}}$$

where $\epsilon = aM_2E/Z_1Z_2e^2(M_1+M_2)$ is the reduced energy (M_1, M_2 are the projectile and target masses and E is the projectile energy). The constants A, B, C were tabulated for various atom pairs and for an average over a range of pairs. The stopping power may then be calculated from

$$(dE/dx)_n = \frac{4\pi a^2 NE}{\epsilon} \frac{M_1M_2}{(M_1 + M_2)^2} S_n(\epsilon)$$

The total stopping power for alanine was calculated by adding the contributions from the individual atoms in alanine. For the nuclear stopping, the "average" parameters quoted in ref. 72 were used.

5.3.2 Experimental

Samples of alanine (Sigma Chemical Co., St. Louis, Mo.) were dissolved in methanol and water, then electrosprayed onto aluminized polyester film to give a sample thickness $\sim 40\,\mu g/cm^2$. A typical time-of-flight spectrum is shown on the left in fig. 5.10. The most prominent lines correspond to the molecular protonated ion at mass 90, the fragment at mass 44, and the Na^+ background ion at mass 23.

Secondary ions from alanine produced by Cs^+, K^+, Na^+ and Li^+ ions at energies up to 16 keV were measured. The secondary ion energy was 8 keV. Spectra were taken using a time-to-amplitude converter and a pulse-height analyser as described in §3.2.

The number of secondary ions detected in each peak N_D, was determined by integrating the counts in the corresponding channels of the pulse-height analyser. The analysis was performed using the applications program supplied with the analyser. The number of desorbed ions is then $N_s = N_D/G$ where G is the transmission of the acceleration grid (60%). The efficiency for detection is assumed to be near 100%. The number of primary ions hitting the target N_p was calculated from the measured slit current using eq'n 2.4. The total yield is then given by

$$Y = \frac{N_s}{N_p} = K \frac{N_d V_{def}}{Q \sqrt{2 m_p V_p}}$$

where

$$K = \frac{e^{3/2} L}{G^2 sdf} = 1.32 \times 10^{-27}\ C^{3/2} m^{-1} s$$

is determined from geometrical constants (§2.4.2) and the primary pulse frequency (f = 5 kHz for these measurements); Q is the integrated slit current ($I_{slit} \cdot T$), m_p, V_p are the mass and accelerating potential of the primary ion, and V_{def} is the deflection pulse height ($\approx$ 400 V for these measurements). As mentioned in §2.4.4 the measured slit current may overestimate the primary current so the absolute yields should be treated as lower limits.

The secondary ion yield is strongly affected by target preparation so the same target was used for Li^+, K^+ and Na^+ pri-

mary ions. However, because of target damage from sparking, it was necessary to use a different target for the measurements with Cs^+ ions. Since the $(M+H)^+$ yield from this target was ≈ 3 times lower (measured for 6 keV Cs^+ ions) than that from the target used with the other primary ions, the Cs^+ yields were scaled accordingly.

5.3.3 Results

Figs. 5.12 - 5.15 show the relative yields for various secondary ions when alanine is bombarded by Cs^+, K^+, Na^+ and Li^+

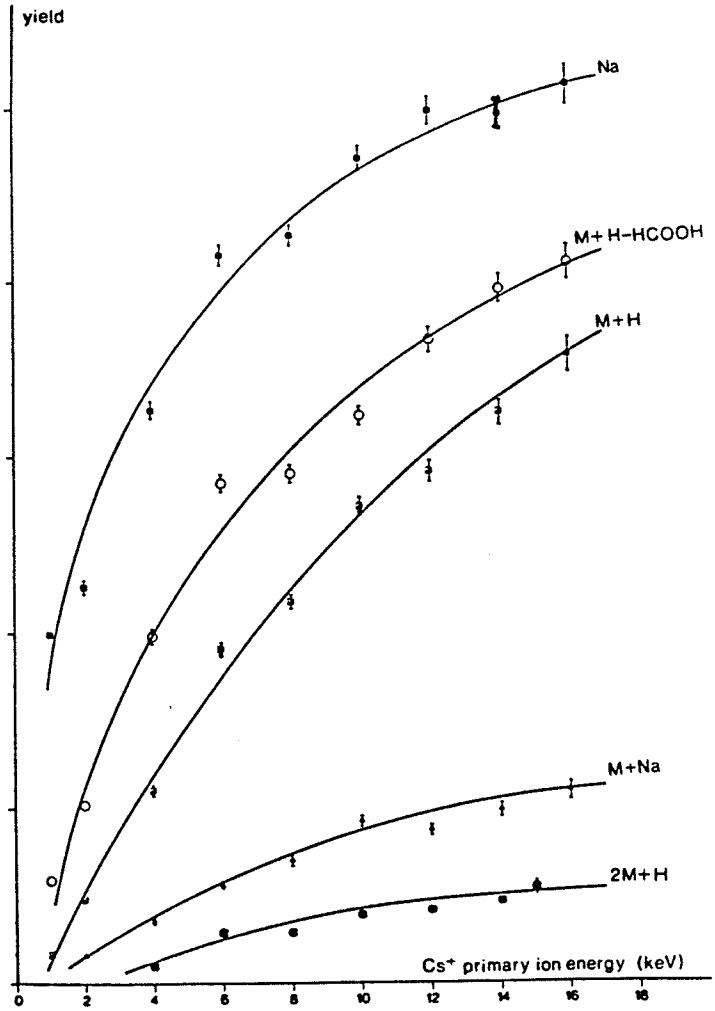

Figure 5.12 Secondary ion yields from alanine produced by Cs^+ primary ions. (The vertical scale is linear.)

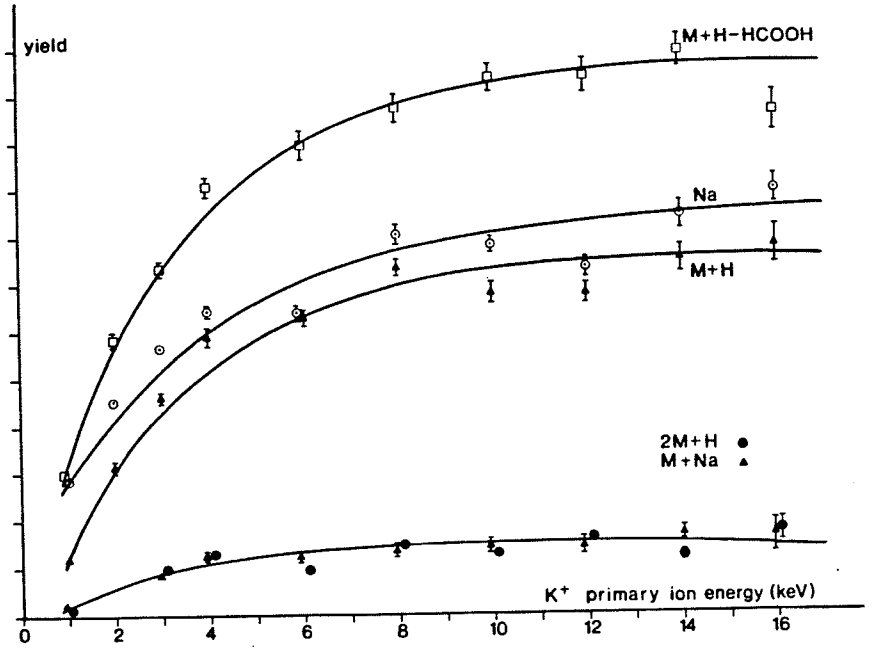

Figure 5.13 Secondary ion yields from alanine produced by K^+ primary ions. (Linear vertical scale)

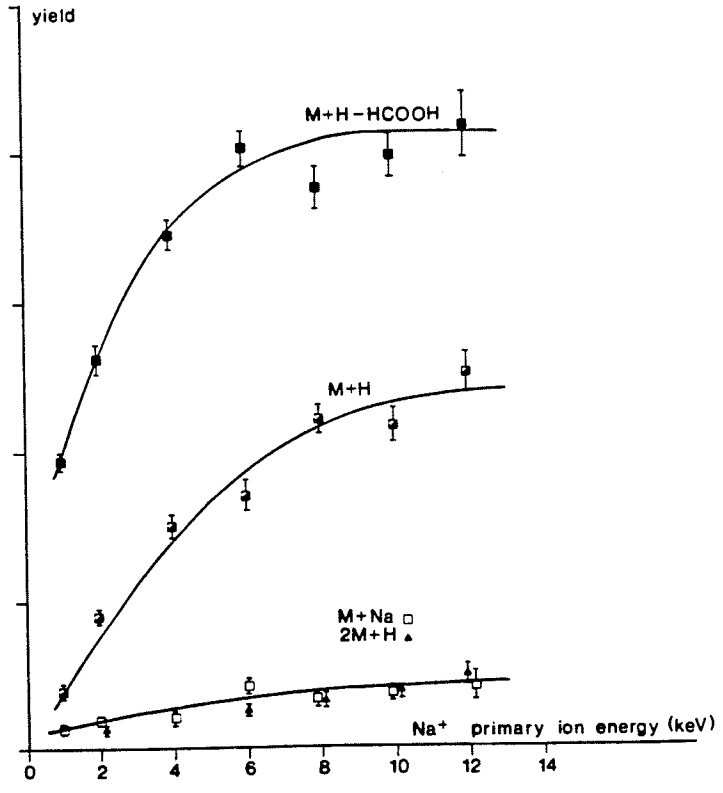

Figure 5.14 Secondary ion yields from alanine produced by Na^+ primary ions. (Linear vertical scale)

ions of energies up to 16 keV. For the lighter ions the curves tend to flatten out between 5 keV and 10 keV, but for Cs^+ the yields are still increasing at 16 keV. The ratio of the molecular protonated ion $(M+H)^+$ to the fragment ion $(M+H-HCOOH)^+$ increases with increasing primary energy and with the mass of the bombarding particle, having values ~0.1 for 10 keV Li^+, ~0.5 for 2 keV Cs^+ and ~0.9 for 16 keV Cs^+. On the other hand, the ratio of the cluster ion $(2M+H)^+$ to the molecular parent ions $(M+H)^+$ and $(M+Na)^+$ remains fairly constant (for Na^+, K^+, and Cs^+).

The error bars in figs. 5.12 - 5.15 represent the statistical error in the peak integrals. Other random error such as

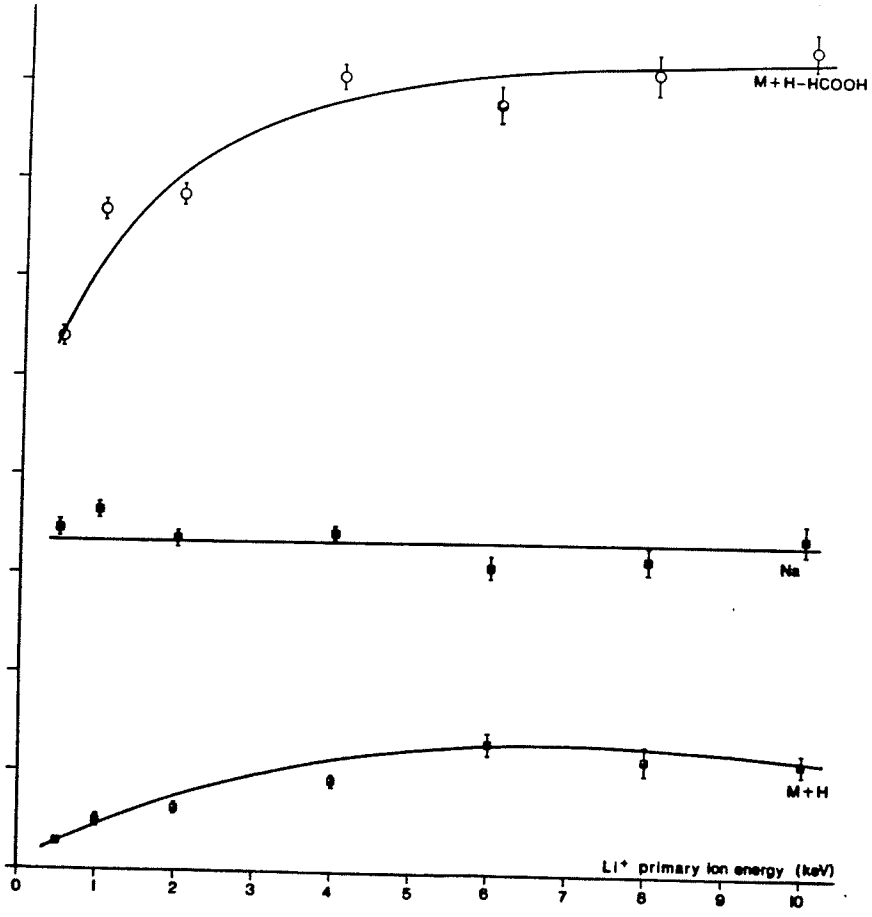

Figure 5.15 Secondary ion yields from alanine produced by Li^+ primary ions. (Linear vertical scale)

fluctuation of the slit current during a measurement also affect the calculation of the yields. These are difficult to estimate but are unlikely to affect the observations made below.

Fig. 5.16 shows the relative yields for the ion $(M+H)^+$ as a function of primary ion energy and species. Clearly there is a strong dependence on the mass of the incident ion. Comparison of the experimental yields (fig. 5.16) with the stopping powers (fig. 5.11) suggests that it is the nuclear energy loss (or perhaps the total energy loss) which is responsible for the

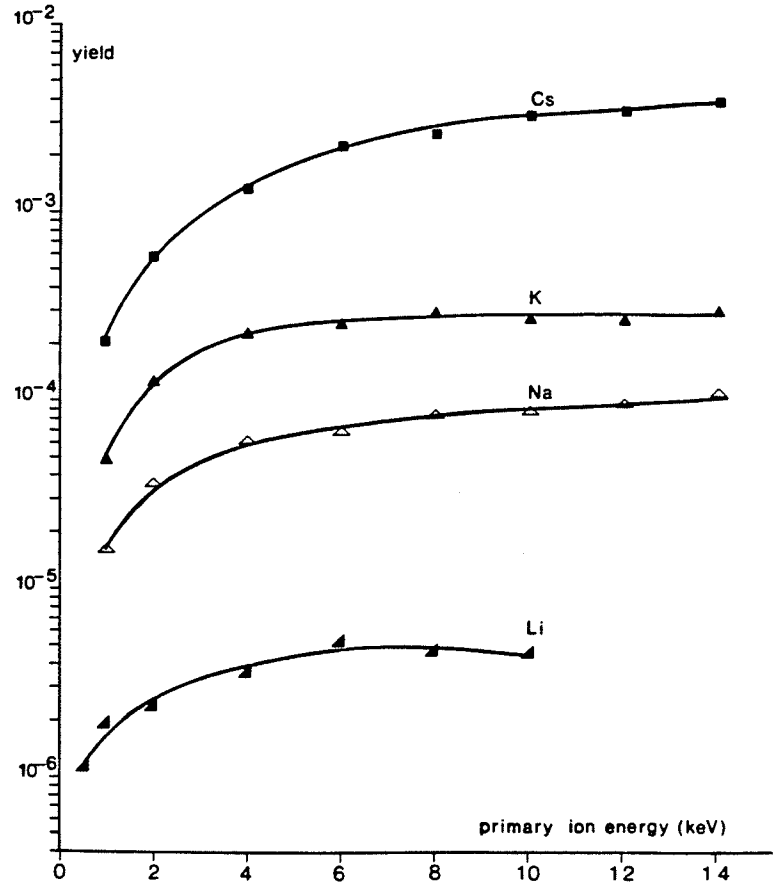

Figure 5.16 Yields of $(M+H)^+$ secondary ions from alanine produced by Cs^+, K^+, Na^+ and Li^+ primary ions. The scale gives the absolute yield (secondary ions/primary ion) estimated by the method described in §2.4.3, so the experimental points should be taken as lower limits.

production of secondary ions in the keV energy region. To illustrate the point, the yields are plotted as a function of electronic stopping (fig. 5.17) and nuclear stopping (fig. 5.18). Apparently electronic stopping is not an important parameter; for

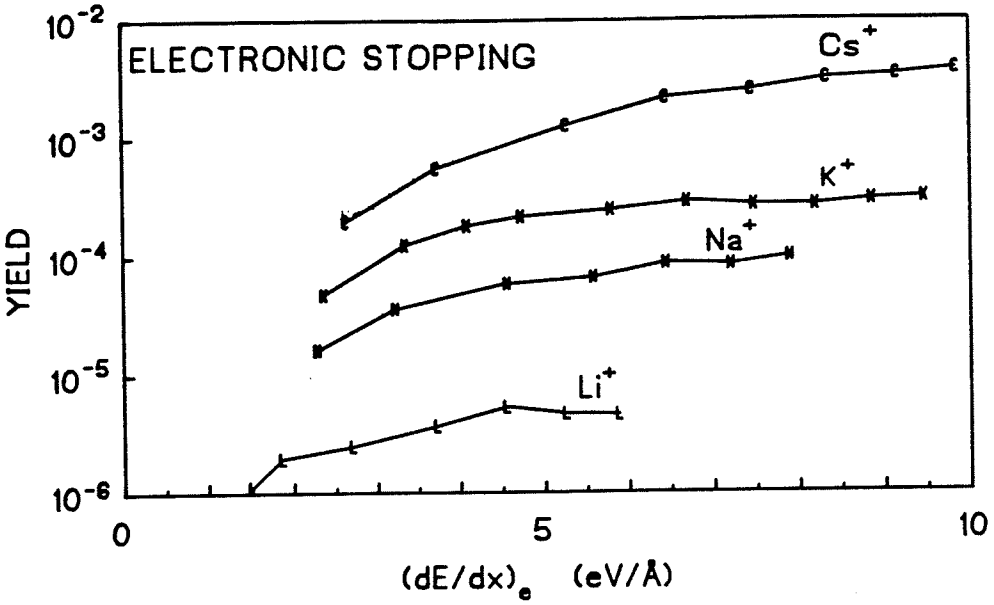

Figure 5.17 Yield dependence of $(M+H)^+$ secondary ions from alanine on electronic stopping power of Li^+, Na^+, K^+, and Cs^+ primary ions.

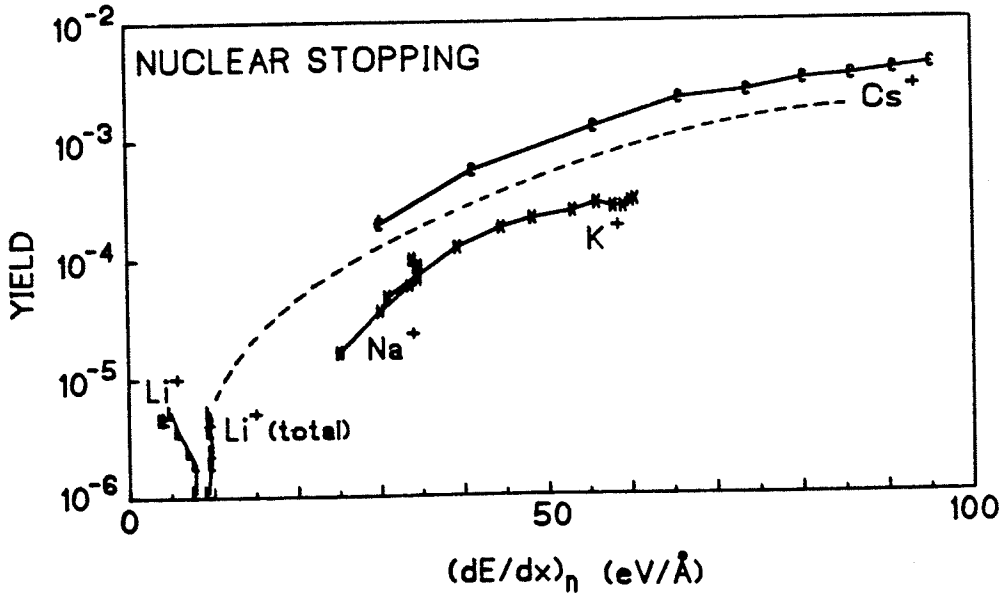

Figure 5.18 Yield dependence of $(M+H)^+$ secondary ions from alanine on nuclear stopping power of Li^+, Na^+, K^+, and Cs^+ primary ions. For primary Li^+ ions, the yield is also plotted against the total energy loss. The dashed line indicates an estimated average curve.

the same electronic energy loss, four different yields ranging across 3 orders of magnitude are obtained. In contrast the yield shows a clear dependence on nuclear stopping; the deviation from an estimated average curve (indicated by the dashed line) is within a factor of ~2. Other factors affecting desorption may explain the deviations or they could result from experimental error - possibly due to the fact that a different area of the target was used for each ion type.

The electronic and nuclear stopping powers have the same order of magnitude but quite different shape for incident Li^+ ions (fig. 5.11). The experimental yields of $(M+H)^+$ for primary Li^+ (fig. 5.16) suggest a dependence on the total energy loss. The yield dependence on the total energy loss for Li is also plotted in fig. 5.18.

5.4 DISCUSSION

The results of the yield measurements (§5.3) show that nuclear stopping causes molecular ion desorption at keV energies in contrast to the high energy (MeV) region where electronic stopping must be responsible for the observed production. Thus it appears that both mechanisms of energy loss are effective in production of secondary organic ions, as suggested also by results reported by Albers et al (75). The similarity in the mass spectra obtained with low energy ions and ^{252}Cf fission fragments (§5.2) indicates that the major processes for the formation of molecular ions are closely related. These observations suggest

that desorption of molecular ions is independent of form of the incident energy but strongly dependent on the the amount of energy deposited; the desorption process is a secondary effect. Other demonstrations of similar mass spectra obtained with different desorption methods have been made (76) However, a comparison between time-of-flight spectra using keV primary ions and fission fragments provides convincing evidence because the difference in energy loss mechanisms may be isolated from experimental parameters. This is not true, e.g., of a comparison between particle and laser desorption, since much higher spatial resolution is normally used with laser desorption and a transient recorder is used to digitize an analogue signal to record laser desorbed time-of-flight spectra.

The constant ratio observed between the yield of clusters $(2M+H)^+$ and the yield of protonated molecular ions $(M+H)^+$ contradicts the result predicted if the cluster were formed in front of the surface by two molecules emitted independently; in that case the yield would be expected to vary as the square of the number of molecules emitted in an individual event (77). Thus the experimental result supports the idea that the clusters already exist on the surface and are ejected as a unit by the primary ion.

The relative yields from keV ions and fission fragments were not measured in this experiment. However since these results were first reported (26) Kamensky et al (78) have performed a comparison of the yield of several organic compounds for 3 keV

Cs^+ and 54 MeV $^{63}Cu^{9+}$ primary ions. They report somewhat different spectra of ergosterol with the two primary ions but the differences may result from other components (background and CsI clusters) in the low energy primary beam, and the difference in time resolution. The ratio of yield from 54 MeV $^{63}Cu^{9+}$ ions to that from 3 keV Cs^+ ions was always greater than 1 and increased with the mass of the sample molecule (to 196 ± 50 for trinucleoside diphosphate, m/z 1884). These ratios would probably be considerably lower if somewhat higher Cs^+ energies were used; according to fig. 5.12, the yield of alanine from primary Cs^+ ions is still increasing rapidly at 3 keV. Indeed, it is not clear that the Cs^+ ion energy at the target was 3 keV since they were accelerated to 3 keV but the target was at high voltage (apparently near 3 kV) to accelerate the secondary ions.

The lower yield from keV ions can be compensated for to some extent by bombarding with larger primary ion fluxes. The flux of fission fragments or accelerated ions (from continuous beams) is limited by the random time distribution; if the flux is too high there is confusion as to which primary ion caused desorption. The flux of fission fragments is also limited by the availability of strong ^{252}Cf sources and the problem of containing the radioactivity. On the other hand, with a pulsed ion beam the number of ions in each pulse may be increased to a large value. In the present apparatus it has been straightforward to produce a flux of pulsed ions 2-3 orders of magnitude more intense than that available from the strongest practical californium source. However, increasing the bombarding ion flux may at some point produce sample charging effects or radiation damage.

If an increase in primary ion flux is accompanied by an increase in background, then poorer signal-to-noise ratios are expected for low energy ions. The result that the ratio of yields increases for larger molecules (78) then has important implications; this suggests that the mass limit may be higher for more massive or more energetic ions. In fact, this appears to be true; molecular ions from vitamin B_{12} were not observed using primary K^+ ions but the spectra taken with Cs^+ ions (fig. 5.8) show molecular parent ions with signal-to-noise ratios comparable to the fission fragment spectra. Until now we have not been able to observe molecular ions from bovine insulin (m/z 5739) using 10 keV Cs^+ ions* although high yields of this compound have been measured with ^{252}Cf fission fragments and 90 MeV $^{127}I^{18+}$ (12). Recently molecular ions from insulin were observed at Rockefeller University using fission fragments incident on the same target analysed here.

It was suggested (78) that high energy bombardment activates a larger area and that this may be necessary to desorb the larger more extended molecules. Recent measurements of secondary ion multiplicity for high energy bombardment of large organic molecules (79,80) support this idea. The <u>average</u> number of secondary ions detected per primary projectile was ≥ 4, and some incident particles ejected more than 32 secondary ions; the observation of insulin molecular ions was correlated with events

* Bovine insulin has been observed (with rather poor yield) with 9.5 keV Xe atoms incident on a glycerol matrix (18). The difference is probably a result of the liquid matrix which may reduce the amount of energy required for desorption of molecular ions.

in which the average multiplicity was greater than the overall average. We have made similar measurements here using low energy primary ions (81). In contrast to the results obtained with high energy primary ions, events yielding more than one secondary ion were almost one hundred times less probable than those yielding a single secondary ion.

Thus there are considerable advantages (figs. 5.12 - 5.15) in bombarding the target with particles having a larger energy loss. Cs^+ ions at 16 keV gave higher yields and less fragmentation than any others measured; installation of a liquid metal ion source is planned to see if this behavior extends to heavier primary ions and perhaps to bombardment by cluster ions.

CHAPTER 6

METASTABLE MEASUREMENTS OF CsI CLUSTERS

6.1 INTRODUCTION

Clusters are aggregates of too few atoms or molecules to take on the bulk properties of a solid. Their study is important to the understanding of nucleation phenomena valuable in many areas of physics and industry. Since their properties are distinct from those of solids and gaseous molecules the study of clusters has become a discipline in itself. The study of the desorption of clusters by particle impact may also contribute to an understanding of the desorption of involatile organic molecules.

Because it is a many-body problem, most of the theoretical work has been limited to inert gas clusters since they allow a simple potential to be assumed (82). Recently a theoretical treatment of alkali halides has been developed by Martin (83).

Limited experimental data exist on clusters with more than a few atoms because it has been difficult to produce large stable clusters for spectroscopic analysis. However large secondary cluster ions ejected from CsI surfaces by 4.7 keV Xe^+ ion bombardment have recently been observed in a sector-field mass spectrometer (84-86). Positive ions $[(CsI)_nCs]^+$ were detected up to $n = 70$, and negative clusters $[(CsI)_nI]^-$ up to $n = 4$. For the positive clusters the ion intensity decreased rapidly with increasing n, but superimposed on this general decrease were pronounced anomalies; e.g., the intensity of the $n = 13$ cluster was enhanced by a factor ~2, but the clusters with $n = 14$ and 15 lay more than an order of magnitude below the average curve. It was noted that the anomalies were correlated with particularly symmetrical cluster geometries, e.g., $3\times3\times3$ at $n = 13$; clusters formed by the addition of CsI molecules to these structures were evidently suppressed, either in the production process or through instability (84-86). The anomalies were then interpreted (84,87) by a bond-breaking or a cleavage model, under the assumption that they arose in the ion production process.

We have observed similar clusters (88,89) when electrosprayed deposits of CsI were bombarded with 8 keV Cs^+ ions. Positive clusters with n up to ~40 and negative clusters with n up to ~20 were detected (the latter with 28 keV Cs^+ bombardment). The positive and negative time-of-flight spectra are shown in fig. 6.1. In striking contrast to the results mentioned above, the ion yield varies smoothly with n; no significant anomalies are observed. Fig. 6.2 compares the two measurements.

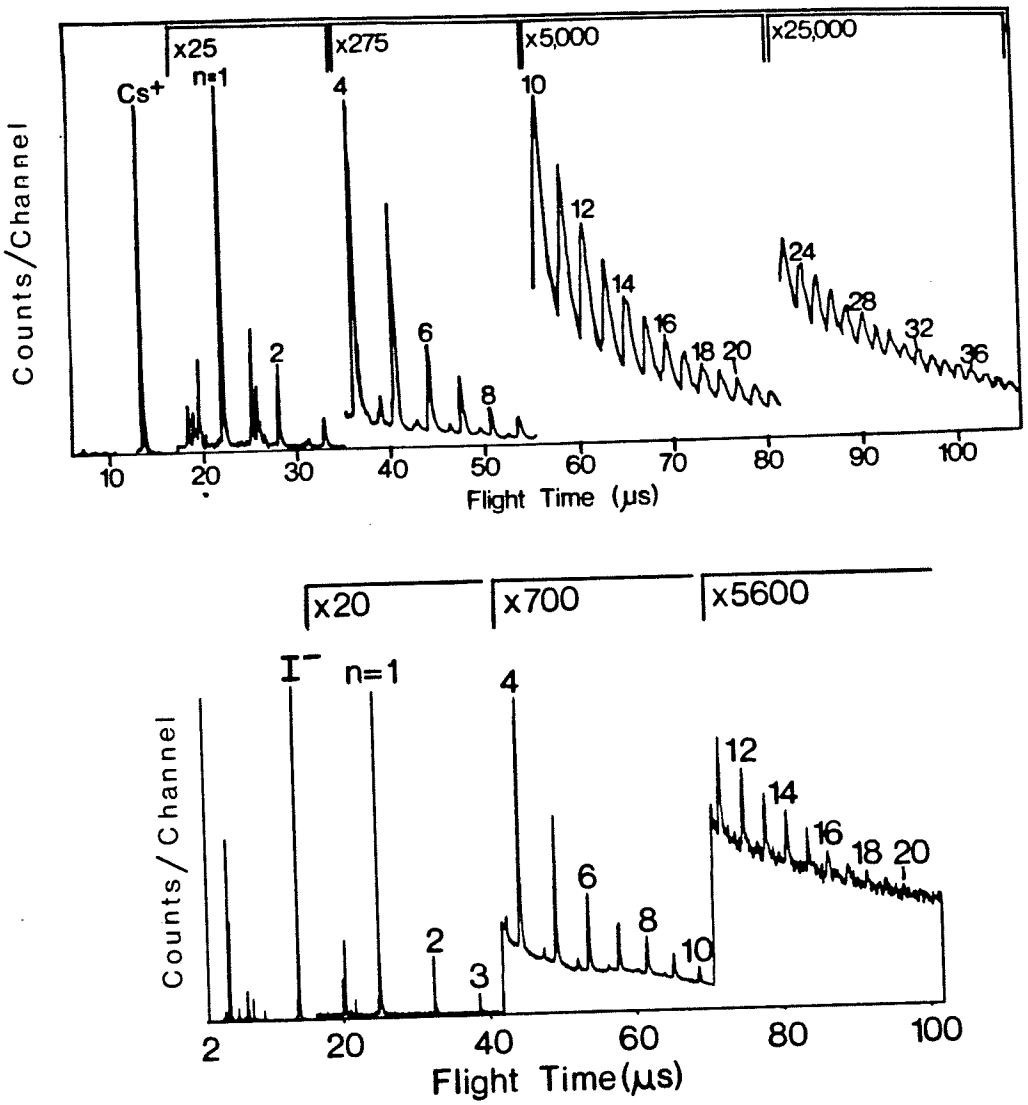

Figure 6.1 Time-of-flight spectra of positive and negative ion clusters, $[(CsI)_nCs]^+$ or $[(CsI)_nI]^-$, at primary Cs^+ average current densities ~2×10^{-10} A/cm^2 after a total irradiation of ~4×10^{15} Cs^+ ions/cm^2. The positive spectrum was taken in 3 sections (6 to 35, 35 to 55, and 55 to 110 μs) and normalized at n = 4 and 10; measurement times were 15, 90, and 120 minutes. The negative spectrum was taken in two sections (0 to 45, and 43 to 100 μs) and normalized at n = 4; measurement times were 10 and 75 minutes. The structures between the main cluster peaks correspond to clusters with replacement of one Cs atom by a Na atom or to replacement of one I atom by a Cl atom.

Methods of target preparation and conditions of ion bombardment were somewhat different in the two cases. However, the most significant difference between them lies in the time scales of the observations, an important factor if the clusters are unstable. In the sector-field spectrometer (90) a cluster ion with $n = 13$ ($m/z \sim 3500$) and energy 0.3 keV requires ~750 μs to traverse the instrument; if the ion decomposes within that time it is not observed, at least not at its original mass. By

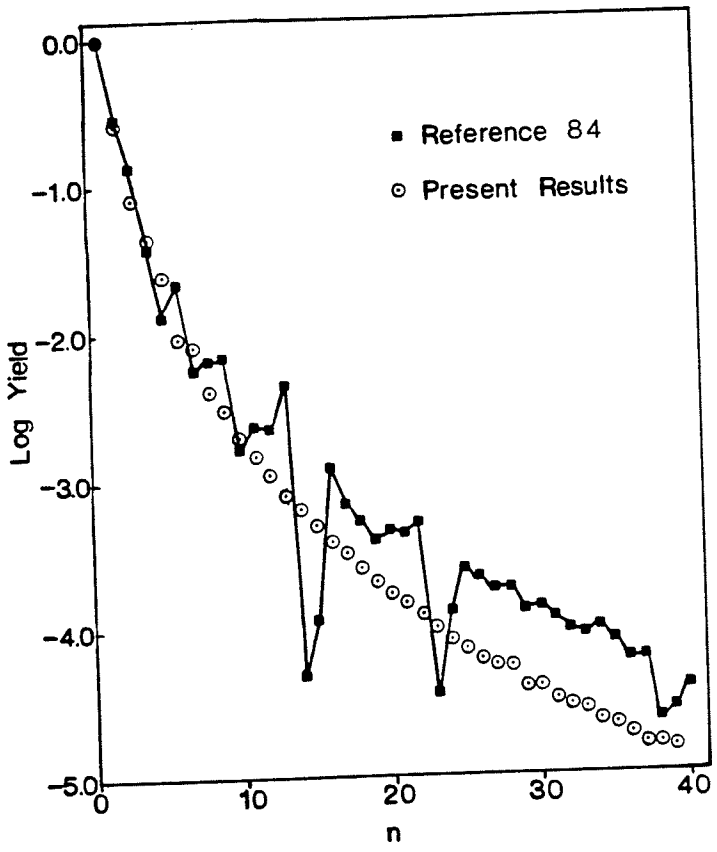

Figure 6.2 Relative yields of $[(CsI)_nCs]^+$ clusters in the present measurements and in the previous measurements (84-86), both normalized to $n = 1$. The slope of the yield function in the present measurements varied for different targets but was always a smooth curve. Neither measurement is corrected for spectrometer or detector efficiency, but these corrections are expected to vary smoothly with n.

contrast, an ion in a time-of-flight spectrometer need survive only long enough to be fully accelerated in order to appear at its original mass number; subsequent decays simply increase the width of the peak (§2.5.4, §4.5.2). In the Manitoba instrument the n = 13 cluster ion is accelerated to its full energy of 10 keV in 0.17 μs, and so these measurements yield the population of n = 13 ions 0.17 μs after their emission.

The retarding grids described in §2.5 were inserted in front of the detector at the end of the flight tube to investigate the stability of the CsI clusters.

6.2 SAMPLE PREPARATION; EFFECTS OF IRRADIATION

A solution of CsI in methanol and water was electrosprayed onto aluminized polyester to give rather thick targets ($\gtrsim 500$ nmoles/cm^2). Initially the relative yields of CsI cluster ions were considerably lower than those reported by Campana et al (84-86); for many targets, clusters with $n \gtrsim 7$ could not be observed. Since the primary current density is several orders of magnitude lower here, the sample was irradiated with the dc ion beam to approximate conditions under which the Xe^+ bombardment spectra were taken. A marked increase in the yield of cations, anions, and all cluster ions was observed after irradiating the sample with $\gtrsim 10^{14}$ Cs^+ ions/cm^2; the same effect was observed with several alkali halides after irradiation with Cs^+ or K^+ (59,91). Fig. 6.3 shows the spectrum of CsI before and after irradiation

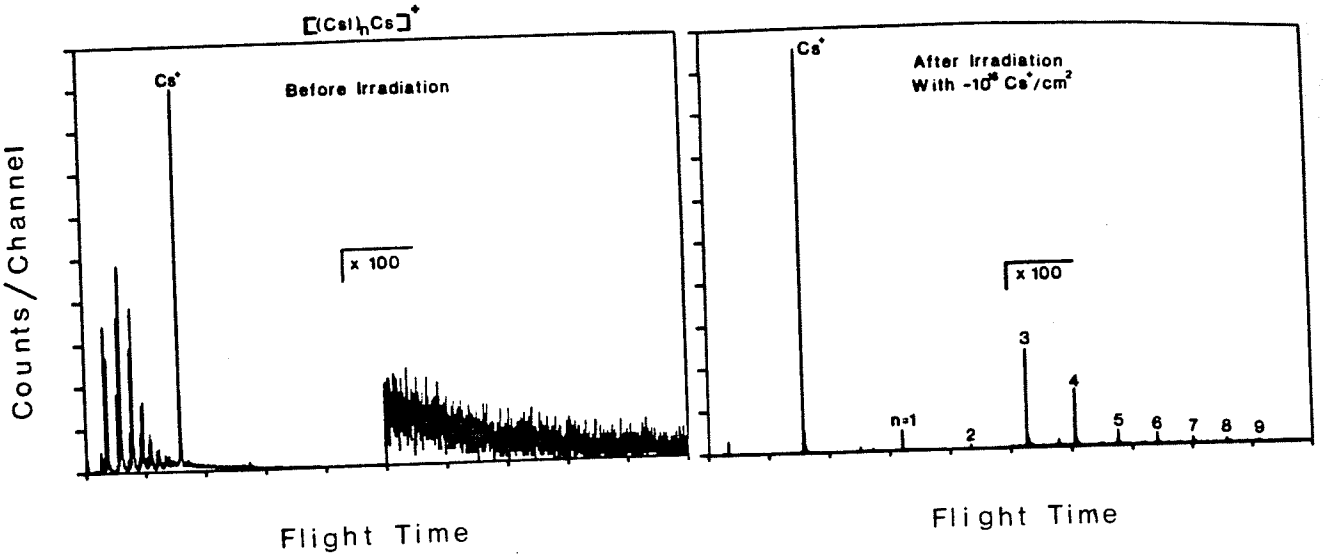

Figure 6.3 Time-of-flight spectra of ions from 8 keV Cs^+ ion bombardment of CsI before and after bombardment with ~10^{16} Cs^+ ions/cm^2 (at 18 keV). The scale on the spectrum before irradiation has been magnified by a factor of 100; i.e. irradiation has increased the yield of Cs^+ ions by a factor ~100.

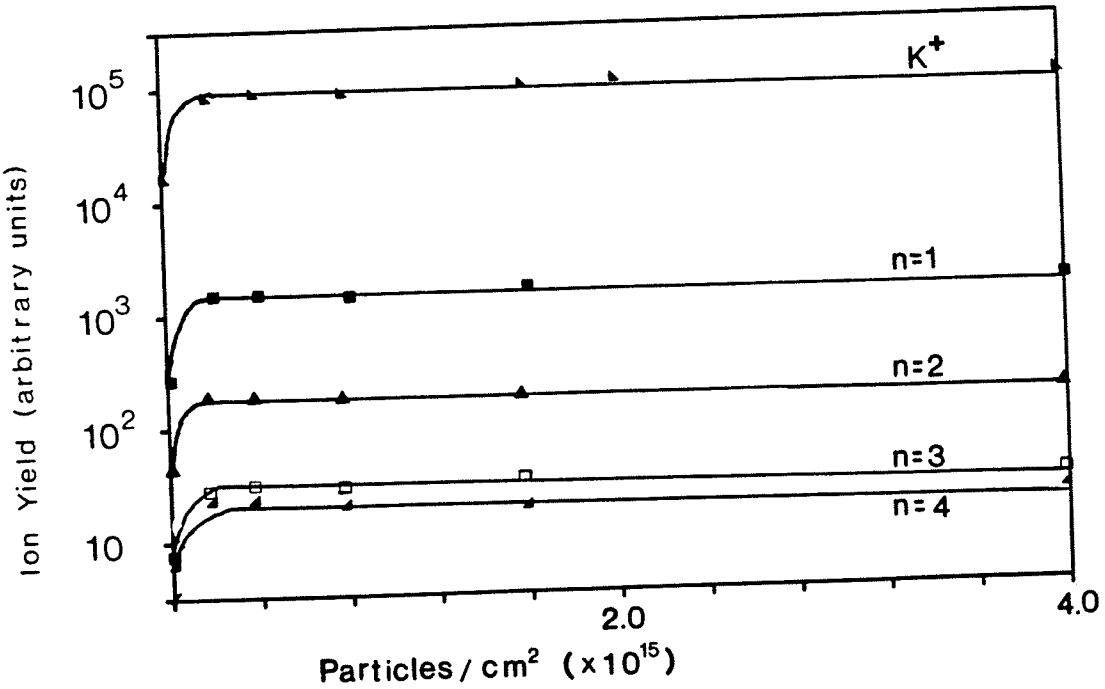

Figure 6.4 Ion yield for K^+ ions and various clusters $[(KI)_nK]^+$ from 8 keV Cs^+ ion bombardment of electrosprayed KI, as a function of the total number of incident Cs^+ ions (at 18 keV) per cm^2.

with ~10^{16} Cs^+ ions/cm^2. Irradiation has increased the yield of Cs^+ ions by a factor ~100 and has given correspondingly large increases in the abundance of cluster ions. After the initial increase, further irradiation produces little effect as shown in fig. 6.4 for KI. Surface cleaning may account for part of the increase, but it appears that the irradiation causes some other changes in the sample properties (possibly in the crystal structure) since most of the improvement remains even after a sample is exposed to air for more than a week.

Irradiation of KI with Cs^+ allows the additional effect of ion implantation to be observed; fig. 6.5 shows the appearance of clusters containing the implanted ions after irradiation. The increase in yield of these clusters with irradiation is much more gradual but continues for larger doses as shown in fig. 6.6. The appearance of these mixed clusters indicates that in fact substantial changes in the surface properties occur.

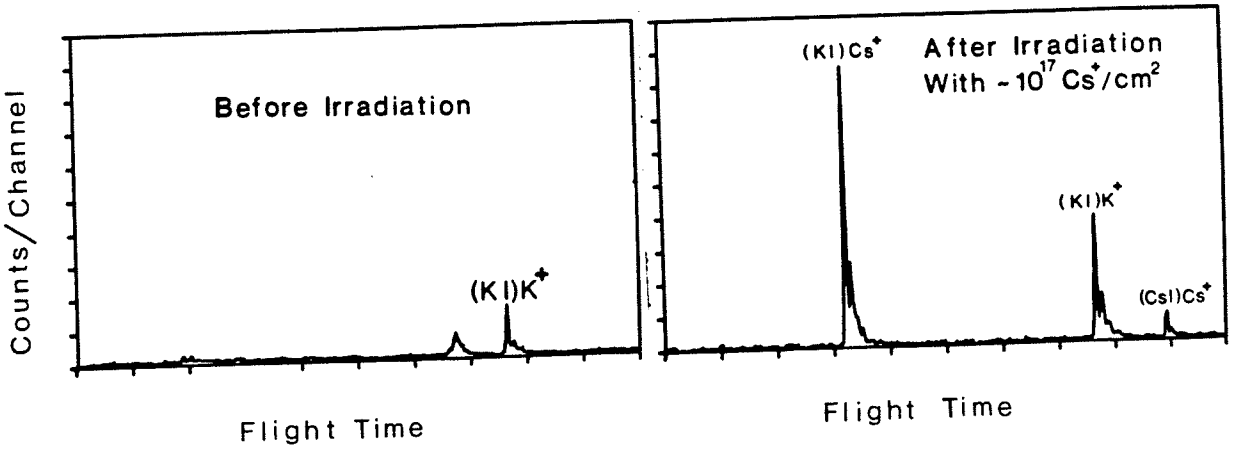

Figure 6.5 Time-of-flight spectra of ions from 8 keV Cs^+ ion bombardment of KI before and after bombardment with ~10^{17} Cs^+ ions/cm^2 (at 18 keV). Clusters containing implanted Cs^+ ions appear after irradiation.

Because the enhanced emission diminishes gradually after irradiation, targets used in this experiment were irradiated before each measurement with ~4×10^{15} Cs^+ ions/cm^2. Since CsI was bombarded with Cs^+ ions, both of the above effects were present but the effect of implantation is evidently small; the CsI cluster yields flatten out after ~10^{15} incident Cs^+ ions/cm^2.

Target irradiation also causes delayed emission of some secondary ions; broad secondary peaks were observed ~200 ns, after each of the cation and cluster peaks. The identification of these peaks with delayed emission was confirmed by pulsing the target potential. The results for the $(CsI)Cs^+$ peak are shown in fig. 6.7; peaks corresponding to ions emitted promptly shift independently of the peaks corresponding to the delayed ions for

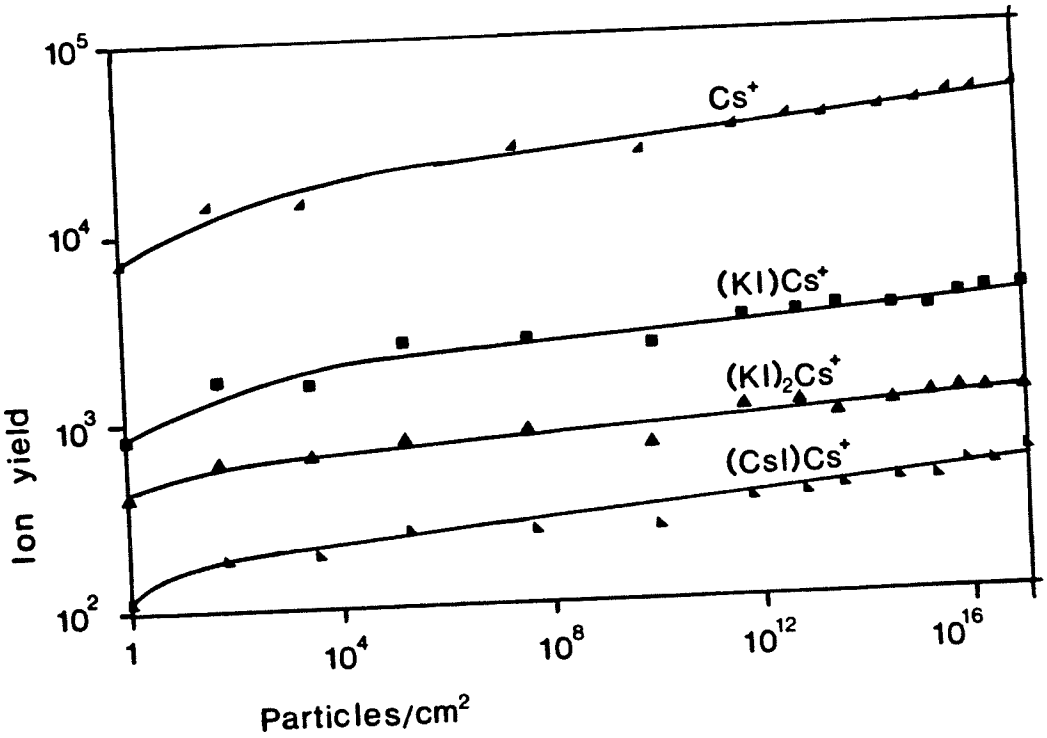

Figure 6.6 Ion yield for mixed clusters from 8 keV Cs^+ ion bombardment of electrosprayed KI, as a function of the total number of incident Cs^+ ions (at 18 keV) per cm^2

target pulses applied 170 ns apart. The relative height of the delayed peaks increases for larger clusters, and for $n \gtrsim 7$ the effect produces a high-time tail on the peaks. This is the reason

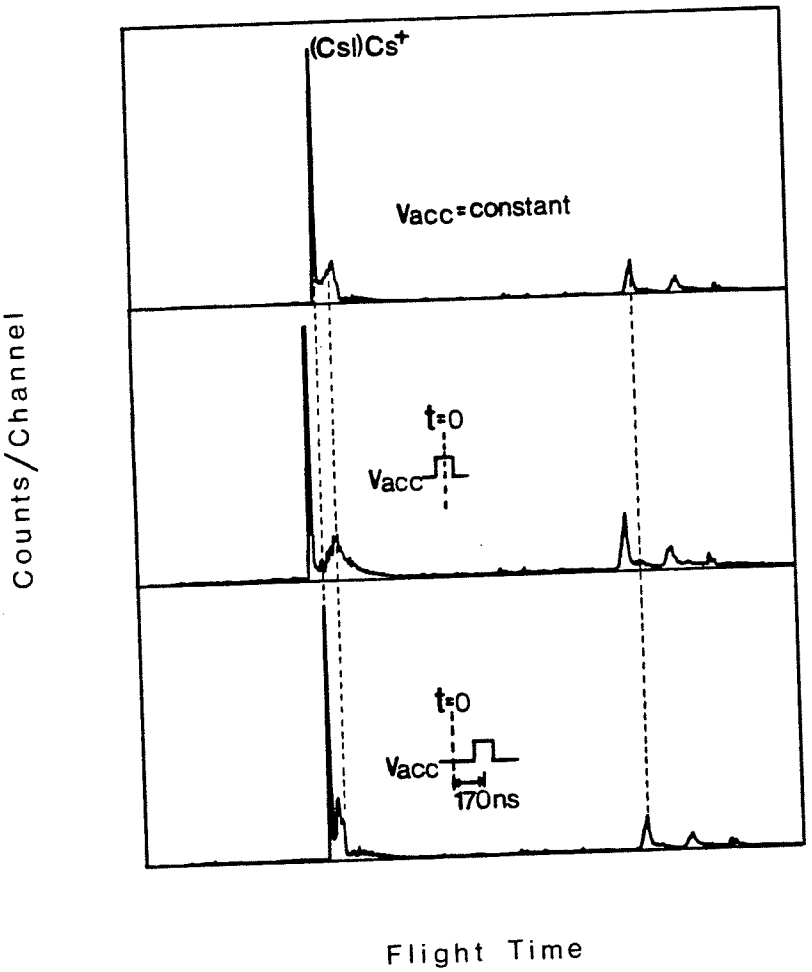

Figure 6.7 Effect of pulsing the target potential from 10 kV to 10.25 kV on the time-of-flight spectrum of CsI near the $(CsI)Cs^+$ peak after the target was irradiated by $\gtrsim 10^{16}$ Cs^+ ions/cm^2. When the pulse is applied at $t = 0$ (when the primary ions hit the target) ions desorbed promptly receive more acceleration and the corresponding peaks shift to shorter times but the broad secondary peaks are not shifted. When the pulse is applied at $t = 170$ ns, the delayed peak is shifted to shorter times. The target was pulsed with an Avtech AVL-A pulse generator triggered through an optical isolater. Its output pulse had 250 V amplitude and 100 ns width; the rise and fall times were $\lesssim 3$ ns.

for the rather broad peaks in the positive spectrum shown in fig. 6.1; the effect is considerably smaller for negative ions and the peaks are correspondingly narrower. In measuring relative yields, the peak integrals included the contribution from the delayed emission.

6.3 MEASUREMENTS

Time-of-flight spectra were measured with a time-to-amplitude converter and analysed with an LSI 11/23 computer (fig. 3.1). Spectra were recorded for various retarding potentials between 7 and 10 kV applied to the central grid of fig. 2.15. Results for the positive clusters with $n = 4$ to 7 are shown in fig. 6.8. For clusters $[(CsI)_nCs]^+$ up to $n = 4$, the parent ions were predominant, but for $n > 4$ fragmentation increased rapidly. Above $n = 7$, no parent ions could be observed, only fragments. The measurements were taken at a pressure of $\sim 10^{-7}$ Torr; an increase in pressure by a factor of 3 gave no observable change in fragmentation. Thus collisions in the flight tube appear to play no important role in the fragmentation observed here*. On the other hand, the results are consistent with metastable decay; evidently the larger clusters acquire enough internal energy during emission to make them unstable on a time scale $\ll 100\,\mu s$.

* Baldwin et al (92) have recently observed collision-activated dissociation when sufficient pressure of He is introduced. They found that the collision cross-section varied in a similar way to the stability.

In fig. 6.8, the peaks labelled "F" correspond to the ejection of one CsI molecule; the dominant mode of decay was found to be ejection of 1 to 3 CsI molecules. For these smaller clusters the mode of fragmentation could be identified by measuring the delay time between the peaks. For larger clusters,

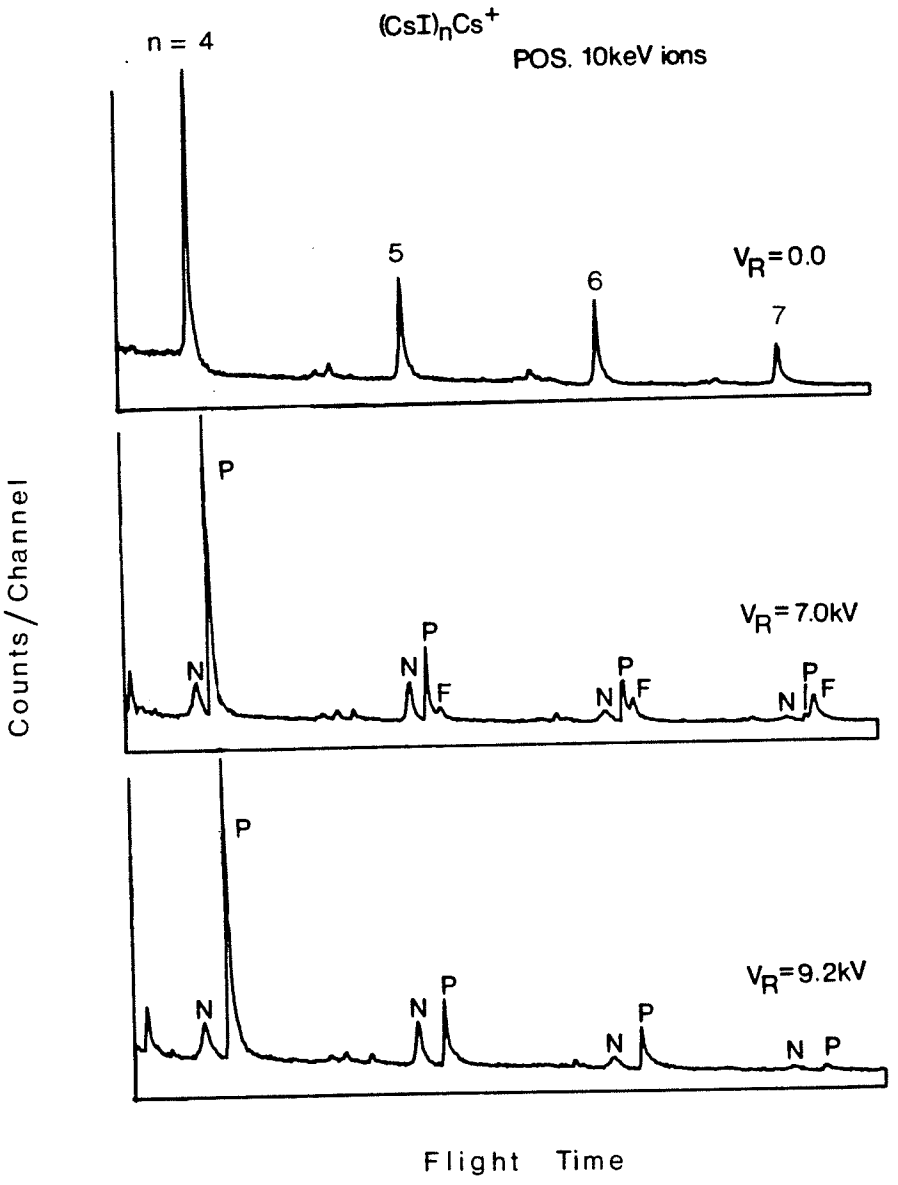

Figure 6.8 Time-of-flight spectra of 10 keV $[(CsI)_nCs]^+$ cluster ions with zero retarding voltage V_R and with V_R = 7.0 and 9.2 kV. P labels the parent ion, N a neutral fragment and F a charged fragment resulting from the loss of one CsI molecule.

the peaks resulting from delayed fragments could not be separated so the fragmentation patterns were determined by selectively reflecting charged daughters.

Decay of the positive clusters above n = 13 was investigated in some detail. Mass spectra were recorded above the n = 9 cluster (the start was delayed by ≈ 55 μs) for retarding voltages V_R 0, 7.0, 7.5, 8.0, 8.4, 8.6, 8.9 and 9.5 kV. The spectrum at $V_R = 0$ shown in fig. 6.9 (upper trace) corresponds to the number of desorbed parent clusters intact after ~0.17 μs. With $V_R = 9.5$ kV all charged fragments resulting from decay in the flight tube are reflected. Since no intact parent ions were observed in this range the resulting spectrum shown in fig. 6.9 (lower trace)

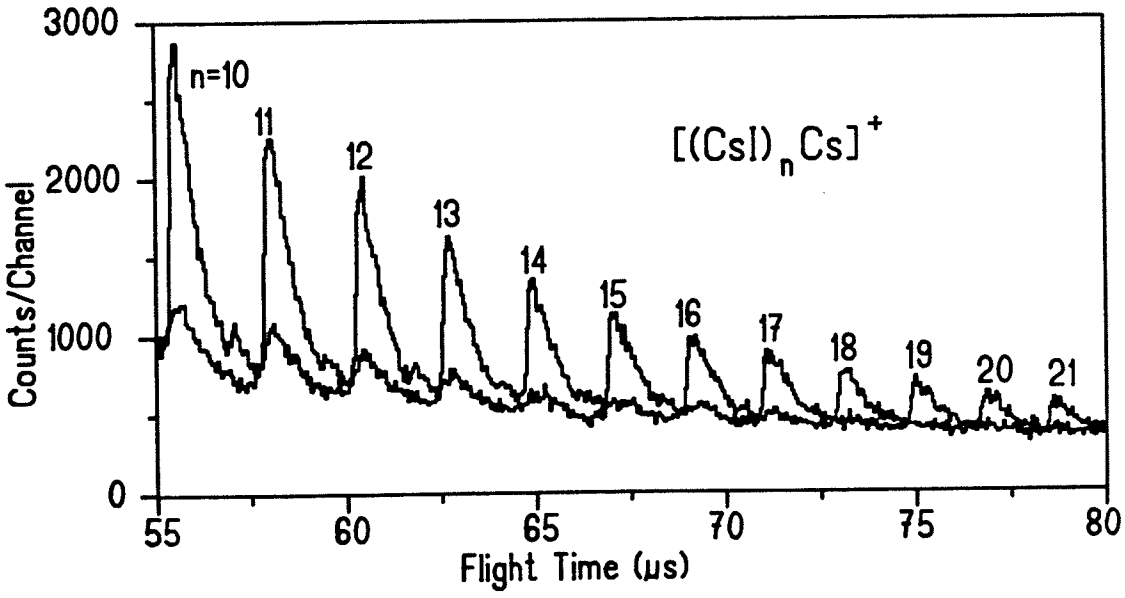

Figure 6.9 The positive spectrum of CsI between n = 10 and n = 20 taken with zero (upper trace) and 9.5 kV retarding potential. The upper trace corresponds to the total number of parents at 0.17 μs. The lower trace corresponds to the number of neutral fragments from decay in the flight tube.

corresponds to neutral fragments. As V_R is increased from 7.0 kV to 9.5 kV, successively larger fragment ions are reflected. For example, fig. 6.10 shows time-of-flight spectra for retarding voltages of 8.0 and 8.4 kV. Here the n = 16 cluster is prominent at V_R = 8.0 kV (≈ 62% of its original yield), but has disappeared at V_R = 8.4 kV. This is consistent with decay of ~60% of the n = 16 parent to n = 13 in the flight tube since the potential required

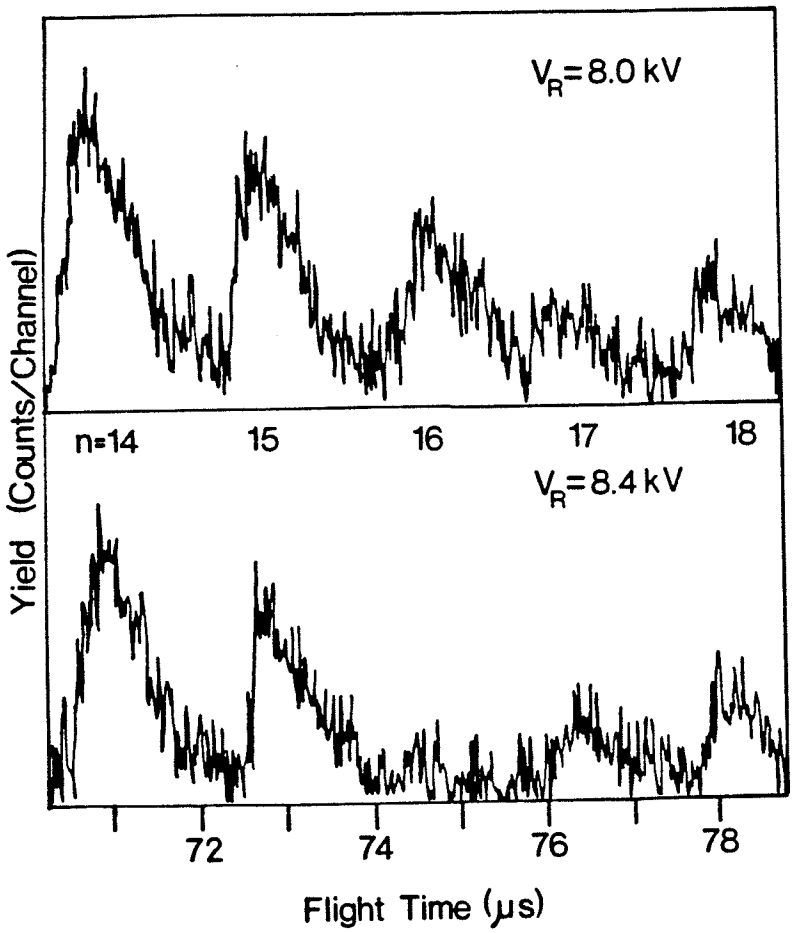

Figure 6.10 Yields of $[(CsI)_nCs]^+$ clusters above n = 13 for retarding potentials V_R = 8.0 and 8.4 kV on the grid in front of the detector. Here background (the spectrum at V_R = 9.5 kV) has been subtracted.

to stop this fragment is

$$V_R = (10\,kV)\,\frac{(13\times 260) + 133}{(16\times 260) + 133} \approx 8.2\,kV$$

Peak integration was performed after the background (the spectrum at $V_R = 9.5$ kV) was subtracted. A smooth background was subtracted from the neutral spectrum (fig. 6.10 - lower trace) to obtain the contribution from neutral fragments. The number of counts in the $n = 2$ cluster peak was used for normalization; these ions are stable so the retarding potential does not affect the peak integral. The $n = 2$ peak was not available in these spectra, however, because the start had to be delayed past the $n = 9$ peak to avoid spectrum distortion (§3.2). To obtain the normalization, the detector output was connected to a scaler through a gate (fig. 6.11) which was set to allow pulses corresponding to ions with the desired flight time.

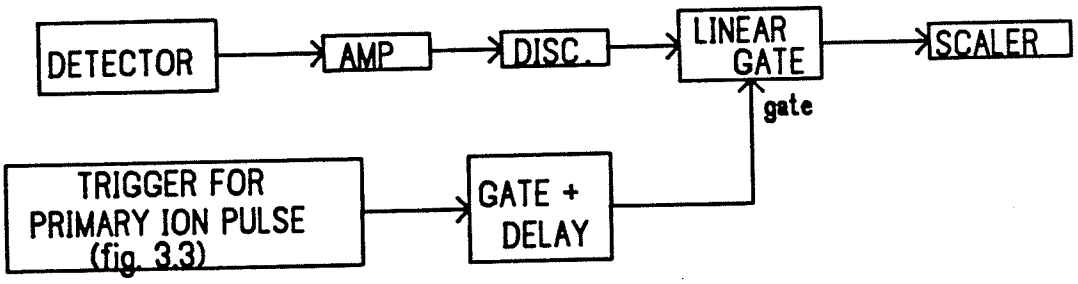

Figure 6.11 Circuits used to obtain normalization from the $n = 2$ cluster peak. The delay was set to the flight time of an $n = 2$ cluster (≈ 28 μs) and the gate width was ≈ 4 μs. (The apparatus is a subset of that specified in fig 3.3.)

Table 6.1 shows the measured decay pattern for parent cluster ions with n = 14 to 18. Disintegrations which yield fragments with n = 13 are strongly favored and fragments with n = 14 and 15 have very low yields. Thus the present distribution also exhibits an anomaly near n = 13, but only at times $\gg 1\,\mu s$ after emission; the anomaly is a result of the pattern of metastable decay, not a consequence of the production process. In the sector-field measurements (84-86,90), an ion with n = 13 spends ~50 μs within the extraction lens before entering the spectrometer, and so it appears likely that many of the large clusters observed were disintegration products originating from regions close to the target. The same comment may apply to some of the

TABLE 6.1

Yield of fragments from CsI clusters measured at ~70 μs after emission, both parent and fragment having structures $[(CsI)_nCs]^+$. Each column lists the percentage yield of fragments with various values of n, i.e., the number of fragments detected per 100 detected events in the parent peak. The last row gives the percentage yield of neutral fragments (measured at $V_R = 9.5$ kV). Estimated errors in these numbers are ±5 or less.

Fragment \ Parent n=	14	15	16	17	18
n= 11	6	6	5	1	0
12	24	22	2	11	0
13	40	40	62	45	26
14	0	0	0	0	6
15		0	0	8	11
16			0	20	19
17				0	22
18					0
Neutrals	17	17	19	16	15

clusters observed earlier in a quadrupole mass spectrometer (93). In more recent measurements with sector-field instruments, Campana et al (94,95) and Baldwin et al (92) have confirmed that metastable decay is responsible for the observed anomalies; they are found to "wash out" as the accelerating voltage is increased (94,95).

The peaks in the spectra of parent ions include neutral as well as charged fragments, indicated in Table 6.1. Some of these neutral fragments are CsI molecules ejected in the decays discussed above. Their number may be estimated from the number of charged fragments observed if it is assumed that the efficiency of the microchannel plate detector is proportional to the number of atoms in the fragment (52); for example, the number of neutral fragments in the $n = 15$ parent peak corresponding to the charged daughter $n = 13$ would then be $(2/13) \times 40 \approx 6.2$. For $n = 15$ to 18, the calculated sums of the neutral fragments corresponding to the charged daughters observed account for most, if not all, of the neutral fragments detected. Instead of emitting one or more CsI molecules, the parent ion might decay by emission of small charged fragments, e.g., Cs^+. The large neutral fragments produced in this process would be detected with high efficiency. Since the neutral fragments observed are already accounted for, it appears that this mode of decay is relatively improbable.

6.4 CONCLUSIONS

(i) Our measurements give no evidence for anomalies in secondary-ion production; cluster yields were found to decrease smoothly with n when they are measured at sufficiently short times ($\ll 1\,\mu s$) after emission. Such a smooth variation is predicted by a thermal evaporation model (96) or if the clusters are formed by statistical recombination above the surface (86,97); anomalies in cluster emission would contradict such models (86).

On the other hand, a smooth variation in yield might also be expected from ejection of preformed cluster ions directly from the solid state if the probability for their existence in the condensed phase varies smoothly with size. The enhanced yield after irradiation (fig. 6.4) may result from the formation of such clusters by the break-up of larger microcrystals.

(ii) Secondary-ion clusters $[(CsI)_nCs]^+$ produced by 8 keV Cs^+ ion bombardment are predominantly metastable for $n > 7$, with lifetimes $\ll 100\,\mu s$. Decay of the clusters occurs mainly by emission of one or more CsI molecules. The distribution of decay products, observed at times $\sim 70\,\mu s$ after emission, exhibits a striking anomaly; product clusters with $n = 13$ are favored, and clusters with $n = 14$ and 15 are suppressed. This is consistent with the theoretical treatment of alkali halides developed by Martin (83). His simplest calculations use a two-body interaction potential with a point ion Coulomb term and a Born-Mayer

repulsive term:

$$V_{ij} = \frac{Z_i Z_j}{r_{ij}} + Ae^{-r_{ij}/p}$$

where Z_i, Z_j are the atomic numbers of the atoms separated by a distance r_{ij}. The parameters A and p are determined from the crystalline interatomic distance and the crystalline compressibility. The total energy is the sum of all the two-body interactions. The total energy was minimized with respect to r_{ij} to find stable configurations. The calculations indicate (among other things) that clusters with a high degree of cubic symmetry (e.g. $3 \times 3 \times 3$ at $n = 13$) should be particularly stable and additions to these structures should have low binding energies.

(iii) The present measurements give no direct information on the production of neutral clusters. However, sputtering yields of molecules and neutral clusters have necessarily been measured at times $\gg 1\,\mu s$ after emission, and these yields have normally been interpreted as giving the actual distribution of particles ejected in the sputtering process. These results suggest that such interpretations should be accepted with some caution.

APPENDIX A

PREPARATION OF A THERMIONIC ALKALI METAL ION SOURCE

Positive alkali metal ions are produced by heating synthetic alkali alumino silicates on the end of a tungsten filament (38,39). Blewett and Jones (39) studied the dependence of emission from Li^+ sources on composition and found maximum emission for β-eucriptite ($Li_2O \cdot Al_2O_3 \cdot 2SiO_2$). The β-eucriptite for any alkali (alk) is prepared according to

$$alk_2CO_3 + Al_2O_3 + 2SiO_2 \longrightarrow alk_2O \cdot Al_2O_3 \cdot 2SiO_2 + CO_2$$

The reactants are intimately mixed by grinding in a mortar. The resulting powder is then placed in a suitable crucible (zirconium oxide e.g.) and heated to approximately 1400°C for ~15 minutes in an induction furnace. The resulting hard pellet is ground in a mortar.

The filament is an ≈1.5 cm length of 127 μm diameter tungsten wire (Ventron 00369 Tungsten Wire) bent into a hairpin shape and spot-welded to a filament holder (see fig. A.1).

A small amount of the β-eucriptite is mixed with a few drops of amyl acetate in a watch glass, and applied to the tip of the filament to form a bead ~2 mm in diameter. The most stable and symmetric beads have been formed by repeatedly heating the filament red hot over a flame and dipping it in the mixture. A small amount of the β-eucriptite adheres to the filament each time and binds more securely when it is melted over the flame. The procedure is repeated until the desired shape and size is achieved; emittance seems to diminish if the bead is too large ($\gtrsim 2$ mm in diameter) presumably because the temperature at the surface is lower. With a smaller bead set $\gtrsim 1$ mm back from the opening in the anode shield (see fig. 2.7) the beam current tends to have a sharper dependence on the shield potential. This allows some reduction in background if the shield is pulsed (§4.2).

After a new source is installed, current through the filament is increased gradually from 1.0 to ~1.8 A over a period of an hour and then left at ~1.8 A until the beam current measured on the collimator or the slit stabilizes (usually ~1 hour). The cathode plate is then adjusted to give maximum current

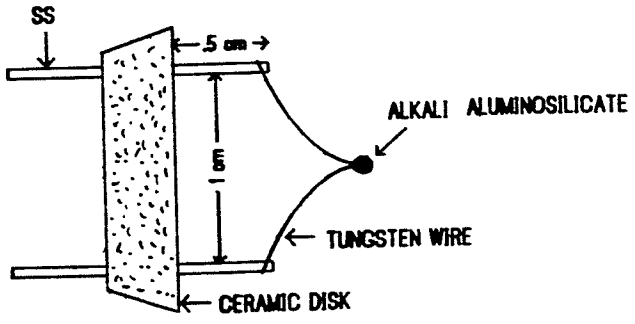

Figure A.1 Filament and holder for thermionic alkali metal ion source. The filament is 127 μm diameter tungsten wire.

(~ 100 nA) on the slit. The dc conditions are obtained by adjusting the anode shield, einsel lens and deflection potentials to maximize current on the target.

The lifetime of a source varies widely from a few hours to several days depending on the size and shape of the β-eucriptite and on the filament current; the effects of these factors have not been measured. Often the filament becomes bent during use and becomes misaligned before the material is depleted. In these cases it is usually easier to replace the source than to realign it.

APPENDIX B

COMPUTER ALGORITHMS

Time-of-flight spectra are displayed on a VT640 graphics terminal with 640 × 480 resolution. Since the spectra may have up to 32000 channels they are binned and sampled so that any region may be examined. However the data analysis routines described below use the raw data unless a bin width is specified for the analysis. If background is subtracted from a region of the spectrum, then the background subtracted data is used for the centroid calculation but not for the peak searching routine.

B.1 PEAK CENTROID, WIDTH AND INTENSITY DETERMINATION

This analysis is similar to that described by McNeal (69). The approximate position and width of a peak are required; these may be entered for individual peaks using cursors or they may be supplied by the peak searching routine (§B.3). In the latter case, the width of the square wave correlator is taken as an

approximate peak width.

The program first determines the points of maximum slope, σ_1 and σ_2, on each side of the peak. Since some peaks may be quite narrow ($\lesssim 3$ channels) these points are calculated to fractional channels; the procedure is illustrated in fig. B.1.

The full width at half maximum is taken as the difference between σ_2 and σ_1 and the intensity as

$$I = \frac{1}{\ln 2}\left[(1 - \sigma_{1f})H(\sigma_{1i}) + \sum_{j=\sigma_{1i}+1}^{\sigma_{2i}} H(j) + \sigma_{2f}H(\sigma_{2i} + 1) \right]$$

where the subscripts i and f indicate integer and fractional part of σ_1 or σ_2 and H(i) is the number of counts in channel i. These values are correct for a gaussian peak shape and give a reasonably consistent approximation for the present peaks. The peak centroids are calculated between the channels σ_{1i} and $\sigma_{2i} + 1$:

$$\text{Centroid} = \frac{\sum_{i=\sigma_{1i}}^{\sigma_{2i}+1} iH(i)}{\sum_{i=\sigma_{1i}}^{\sigma_{2i}+1} H(i)}$$

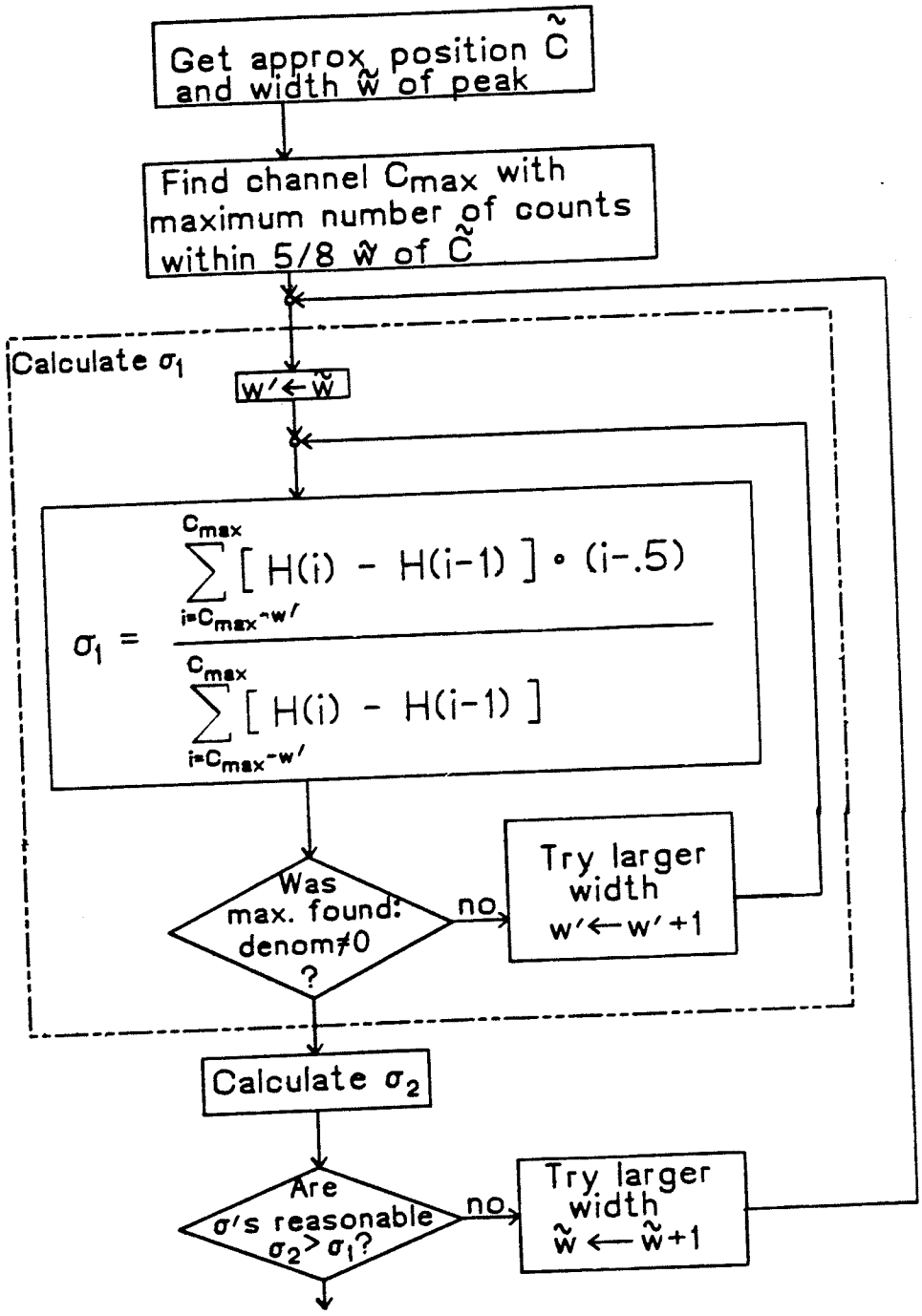

Figure B.1 Determination of points of maximum slope in a peak. H(i) represents the number of counts in channel i of the histogram.

B.2 PEAK SEARCHING

A selected region of the spectrum may be analysed automatically by supplying a representative peak width w and a search sensitivity n. The peak search routine passes a square-wave correlator through the data.

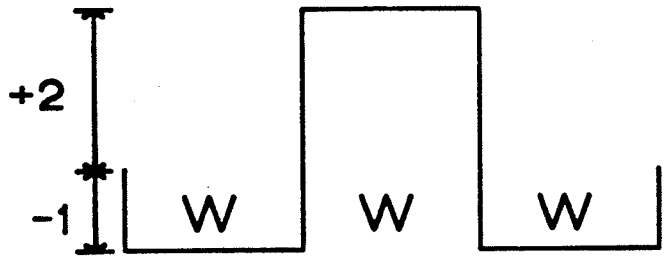

In the absence of a peak, the correlation signal

$$S(i) = -\sum_{k=i}^{i+w-1} H(k) + 2\sum_{k=i+w}^{i+2w-1} H(k) - \sum_{k=i+2w}^{i+3w-1} H(k)$$

should be zero. If it is greater than zero by more than n (usually ≥ 4) standard deviations:

$$S(i) > n\sigma(i) = n\left[\sum_{k=i}^{i+w-1} H(k) + \sum_{k=i+w}^{i+2w-1} H(k) + \sum_{k=i+2w}^{i+3w-1} H(k)\right]^{\frac{1}{2}}$$

then a peak is found. The peak is then analysed using the procedure described in §B.1 taking w as the approximate peak width.

B.3 BACKGROUND SUBTRACTION

Background may be subtracted in any region of the spectrum to improve the accuracy of the centroid determination (§B.1) or for display purposes. Regions of background are indicated using cursors. The data in these regions are then fitted, using a least squares procedure (98), to a function of the form

$$e^{-P_n(x)}$$

where

$$P_n(x)=\sum_{i=0}^{n} a_i x^i$$

is a polynomial of order n; any value of n up to 9 may be used. The coefficients of the polynomial are obtained by solving n simultaneous equations:

$$\sum y_i = a_1 \sum 1 + a_2 \sum x_i + \cdots + a_n \sum x_i^n$$

$$\sum x_i y_i = a_1 \sum x_i + a_2 \sum x_i^2 + \cdots + a_n \sum x_i^{n+1}$$

$$\sum x_i^2 y_i = a_1 \sum x_i^2 + a_2 \sum x_i^3 + \cdots + a_n \sum x_i^{n+2}$$

$$\vdots$$

$$\sum x_i^n y_i = a_1 \sum x_i^n + a_2 \sum x_i^{n+1} + \cdots + a_n \sum x_i^{2n}$$

REFERENCES

1) G. Junk and H. Svec, J. Am. Chem. Soc. 85 (1963) 839.

2) M.S.B. Munson and F.H. Field, J. Am. Chem. Soc. 88 (1962) 2621.

3) G.D. Daves, Jr., Acc. Chem. Res. 12 (1979) 359.

4) M.L. Vestal, Mass Spectrom. Reviews 2 (1983) 447.

5) R.J. Beuhler, E.O. Flanigan, L.J.Greene and L.Friedman, Biochem. Biophys. Res. Commun. 46 (1972) 1082.

6) R.J. Beuhler, E.O. Flanigan, L.J. Greene and L. Friedman, J. Am. Chem. Soc., 96 (1974) 3990.

7) M. Ohashi and N. Nakayana, Org. Mass Spectrom. 13 (1978) 642.

8) H.D. Beckey, Int. J. Mass Spectrom. Ion Phys. 2 (1969) 500.

9) D.S. Simons, B.N. Colby, and C.A. Evans,Jr., Int. J. Mass Spectrom. Ion Phys. 15 (1974) 291.

10) R.D. Macfarlane and D.F. Torgerson, Science 191 (1976) 81.

11) R.D. Macfarlane and D.F. Torgerson, Int. J. Mass Spectrom. Ion Phys.,21 (1976) 81.

12) B. Sundqvist, A. Hedin, P. Håkansson, I. Kamensky, J. Kjellberg and M. Salephour, Int. J. Mass Spectrom. Ion Phys. 53 (1983) 167.

13) P. Dück, W. Treu, H. Fröhlich, W. Galster and H. Voit, Surf. Sci., 95 (980) 603. ;Nucl. Inst. and Meth. 168 (1980) 601.

14) P. Håkansson, I. Kamensky and B. Sundqvist, Surf. Sci. 16 (1982) 302.

15) R.D. Macfarlane, in A. Benninghoven (Ed.), Ion Formation From Organic Solids, Springer-Verlag, Heidelberg, 1983, pp.32-46.

16) A. Benninghoven and W. Sichtermann, Anal. Chem. 50 (1978) 1180.

17) M. Barber, R.S. Bordoli, R.D. Sedgwick and A.N. Tyler, J. Chem. Soc. Chem. Commun., (1981) 325.

18) A.M. Buko, L.R. Lawrence and B.A. Fraser, Biomed. Mass Spectrom. 10 (1983) 408.

19) C. Fenselau, J. Yergey and D. Heller, Int. J. Mass Spectrom. Ion Phys. 53 (1983) 5; J.A. Yergey, D. Heller, R.J.Catter and C. Fenselau, Proceedings of the 31st Annual Conference on Mass Spectrometry and Allied Topics, Boston, 1983, p. 353.

20) M.A. Posthumus, P.G. Kistemaker, H.L.C. Menzelaar and M.C. Ten Noever de Brauw, Anal. Chem. 50 (1978) 985.

21) B. Schueler, P. Feigl, F.R. Krueger and F. Hillenkamp, Org. Mass Spectrom., 16 (1981) 502.

22) B.T. Chait and K.G. Standing, Int. J. Mass Spectrom. Ion Phys. 40 (1981) 185.

23) B. Sundqvist, private communication to K.G. Standing.

24) B.T. Chait, private communication.

25) P. Steffens, E. Niehuis, T. Friese, and A. Benninghoven, in A. Benninghoven (Ed.), Ion Formation from Organic Solids, Springer-Verlag, Heidelberg, 1983, pp.113-117.

26) W. Ens, K.G. Standing, B.T. Chait and F.H. Field, Anal. Chem. 53 (1981) 1241.

27) J.B. Westmore, W. Ens and K.G. Standing, Biomed. Mass Spectrom. 9 (1982) 119.

28) R. Beavis, W. Ens, K.G. Standing and J.B. Westmore, Int. J. Mass Spectrom. Ion Phys. 46 (1983) 471.

29) W. Ens, K.G. Standing, J.B. Westmore, K.K. Ogilvie, and M.J. Nemer, Anal. Chem. 54 (1982) 960.

30) R. Beavis, W. Ens, M.J. Nemer, K.K. Ogilvie, K.G. Standing and J.B. Westmore, Int. J. Mass Spectrom. Ion Phys. 46 (1983) 475.

31) W.F. Hadden and F.W. McLafferty, Anal. Chem. 41 (1969) 31.

32) R.E. Ferguson, K.E. McCulloh and H.M. Rosenstock, J. Chem. Phys., 42 (1965) 100.

33) W.W. Hunt,Jr., R.E. Huffman and K.E. McGee, Rev. Sci. Instrum. 35 (1964) 82.

34) B.T. Chait and F.H. Field, Int J. Mass Spectrom. Ion Phys. 41 (1981) 17.

35) A. Benninghoven, Int. J. Mass Spectrom. Ion Phys. 53 (1983) 85.

36) C.J. McNeal, R.D. Macfarlane and E.L. Thurston, Anal. Chem. 5 (1979) 2036.

37) F.R. Krueger, Chromatographia 101 (1977) 151.

38) J. Zeleney, Phys. Rev. 10 (1917) 1.

39) W.C. Wiley and I.H. McClaren, Rev. Sci. Instrum. 26 (1955) 1150.

40) U. Boese, H.J. Neusser, R. Weinkopf and E.W. Schlag, J. Phys. Chem. 86 (1982) 4857.

41) W. Gohl, R. Kutscher, H.J. Laue and H. Wollnik, Int J. Mass Spectrom. Ion Phys. 48 (1983) 411.

42) J.P. Blewett and E.J. Jones, Phys. Rev. 50 (1936) 464.

43) S.K. Allison and M. Tamegai, Rev. Sci. Instrum. 32 (1961) 1090.

44) M.E. Haine and P.A. Einstein, Br. J. Appl. Phys. 3 (1952) 40.

45) M.E. Haine, P.A. Einstein and P.H. Borcherds, Br. J. Appl. Phys. 9 (1958) 482.

46) G. Liebmann, Proc. Phys. Soc. (London) B62 (1949) 213.

47) P.M.Y. Bernard, Le Journal de Physique et le Radium 14 (1953) 381

48) J.L. Verster, Philips Res. Repts. 18 (1963) 465

49) A. Recknagel, Z. Phys. 111 (1938) 61.

50) B. Leskovar, Phys. Today 42 Nov. 1977.

51) N. Fürstenau, W. Kippelberg, F.R. Krueger, G. Weiss and K. Wein, Z. Naturforsch. 32a (1977) 711.

52) R.J. Beuhler and L. Friedman, Nucl. Inst. and Meth. 170 (1980) 309.

53) J.E. Campana, T.M. Berlak, R.J. Cotton, J.J. DeCampo, J.R. Wyatt and B.I. Dunlap, Phys. Rev. Lett. 47 (1981) 1046.

54) B.T. Chait, F.H.Field and W.C. Agosta, 28th ASMS (1980) 657.

55) B.T. Chait, W.C. Agosta and F.H. Field, Int J. Mass Spectrom. Ion Phys. 39 (1981) 339.

56) B.T. Chait, Int J. Mass Spectrom. Ion Phys. 53 (1981) 227.

57) R.D. Macfarlane, Anal. Chem. 55 (1983) 1247A.

58) K.G. Standing, R. Beavis, W. Ens and B. Schueler, Int. J. Mass Spectrom. Ion Phys. 53 (1983) 125.

59) R.J. Day, S.E. Ungar and R.G. Cooks, Anal. Chem. 52 (1980) 557A; H. Grade and R.G. Cooks, J. Am. Chem. Soc. 100 (1978) 5615.

60) A. Eicke, W. Schichtermann and A. Benninghoven, Org. Mass Spectrom. 15 (1980) 289.

61) M. Barber, J.C. Vickerman and J. Wolstenholme, J. Chem. Soc., Faraday Trans. 1, 76 (1980) 549.

62) J.H. Bergman, Proc. R. Soc. Lond. A378 (1981) 1.

63) P.K. Haff, in D.A. Bromley (Ed.) Heavy Ion Science, Vol.III, Plenum, in press.

64) P. Håkansson, I. Kamensky and B. Sundqvist, Nucl. Inst. and Meth. 198 (1982) 43; Surface Science 116 (1982) 302.

65) P. Dück, H. Fröhlich, W. Treu and H. Voit, Nucl. Inst. and Meth. 191 (1981) 245.

66) R.D. Macfarlane and D.F. Torgenson, Int J. Mass Spectrom. Ion Phys. 21 (1976) 81.

67) R.F. Bonner, D.V. Bowen, B.T. Chait, A. Lipton, F.H. Field and W.F. Sippach, Anal. Chem. 52 (1980) 1923.

68) C.J. McNeal, K.K. Ogilvie, N.Y. Theriault and M.J. Nemer, J. Am. Chem. Soc. 104 (1982) 972-981.

69) C.J. McNeal, PhD Dissertation, Texas A & M University, 1980, University Microfilms, Ann Arbor, MI.

70) K.G. Standing, B.T. Chait, W. Ens, G. McIntosh and R. Beavis, Nucl. Inst. and Meth. 198 (1982) 33.

71) J. Lindhard, M. Scharff and H.E. Schiott, Mat. Fys. Medd., Dan Vid. Selsk. 33 (1963) no. 14.

72) W.D. Wilson, L.G. Haggmark and J.P. Biersack, Phys. Rev. B 15 (1977) 2458.

73) J. Lindhard and M.Scharff, Phys. Rev. 124 (1916) 128.

74) W.P. Wilson and C.L. Bisson, Phys. Rev. B3 (1971) 3984.

75) A. Albers, K. Wien, P. Dück, W. Treu and H. Voit, Nucl. Inst. and Meth. 198 (1982) 69.

76) See, for example, B. Schueler and F.R. Krueger, Org. Mass Spectrom. 14 (1979) 441; Org. Mass Spectrom. 15 (1980) 295.

77) P. Sigmund in N.H. Tolk et al (Ed.), Inelastic Ion-Surface Collisions, Academic, New York, 1977, p. 121.

78) I. Kamensky, P. Håkansson, B. Sundqvist, C.J. McNeal and R. Macfarlane, Nucl. Inst. and Meth. 198 (1982) 65.

79) B. Sundqvist, P. Håkansson, I. Kamensky and J. Kjellberg in A. Benninghoven (Ed.), Ion Formation from organic Solids, Springer-Verlag, Heidelberg, 1983, p. 52.

80) S. Della Negra, D. Jacquet, I. Lorthiois, Y. Le Beyec, O. Becker and K. Wien, Int. J. Mass Spectrom. Ion Phys. 53 (1983) 215; and private communication from Y. Le Beyec to K.G. Standing.

81) R. Beavis, W. Ens, D. Main, B. Schueler and K.G. Standing, to be presented at the proceedings of the 32nd Annual Conference on Mass Spectrometry and Allied Topics, San Antonio, 1984.

82) See, for example, M.R. Hoare, Adv. Phys. Chem. 40 (1979) 49

83) T.P. Martin, Physics Reports 95 (1983) 169.

84) J.E. Campana, T.M. Barlak, R.J. Colton, J.J. DeCorpo, J.R. Wyatt and B.I. Dunlap, Phys. Rev. Lett. 47 (1981) 1046.

85) T.M. Barlak, J.E. Campana, R.J. Colton, J.J. DeCorpo and J.R. Wyatt, J. Phys. Chem. 85 (1981) 3840

86) T.M. Barlak, J.R. Wyatt, R.J. Colton, J.J. DeCorpo and J.E. Campana, J. Am. Chem. Soc. 104 (1982) 1212.

87) B.I. Dunlap, Bull. Am. Phys. Soc. 27 (1982) 255.

88) W. Ens, R. Beavis and K.G. Standing, Phys. Rev. Lett. 50 (1983) 27.

89) K.G. Standing, W. Ens and R. Beavis, in A. Benninghoven (Ed.), Ion Formation from Organic Solids, Springer-Verlag, Heidelberg, 1983, p.107.

90) R.J. Colton, J.E. Campana, T.M. Barlak, J.M. DeCorpo and J.R. Wyatt, Rev. Sci. Instrum. 51 (1980) 1685.

91) W. Ens, R. Beavis, B. Schueler and K.G. Standing, Proc. 31st Annual Conference on Mass Spectrom. and Allied Topics, Boston, 1983, p.631.

92) M.A. Baldwin, C.J. Procter, I.J. Amster and F.W. McLafferty, Int. J. Mass Spectrom. Ion Proc. 54 (1983) 97.

93) F. Honda, G.M. Lancaster, Y. Fukuda and S.W. Rabalais, J. Chem. Phys. 69 (1978) 4931.

94) J.E. Campana, J.R. Wyatt, R.H. Bateman and B.N. Green, Proc. 31st Annual Conf. Mass Spectrom. and Allied Topics, Boston, 1983, p.132.

95) T.M. Barlak, J.E. Campana, J.R. Wyatt, B.I. Dunlap and R.J. Colton, Int. J. Mass Spectrom. Ion Phys. 46 (1983) 523.

96) See, for example, B. Jöst, B. Schueler and F. R. Krueger, Z. Naturforsch. **37a** (1982) 18.

97) G.M. Lancaster, F. Honda, Y. Fukuda and J.W. Rabalais, J. Am. Chem. Soc. 101 (1979) 1951.

98) P.R. Bevington, Data Reduction and Error Analysis for the Physical Sciences, McGraw-Hill Book Company, New York, 1969, p.134ff.